Search for New Physics Using Acoplanar Lepton Pair Events in e^+e^- Collisions at $\sqrt{s} =$ 183-208 GeV

Thomas E. Marchant

March 14, 2002

THE UNIVERSITY
of MANCHESTER

Particle Physics Group
Department of Physics and Astronomy

A thesis submitted to The University of Manchester for the degree of
Doctor of Philosophy in the Faculty of Science and Engineering

Contents

List of Figures

List of Tables

Abstract

A selection of events containing two charged leptons and significant missing transverse momentum has been carried out using a total data sample of 680.4 pb^{-1} collected at $\mathrm{e}^+\mathrm{e}^-$ centre of mass energies between 183 and 208 GeV. The observed numbers of events are consistent with the expectation from Standard Model processes, which come mostly from $\mathrm{W}^+\mathrm{W}^-$ production where both W particles decay leptonically. These events have been used to carry out a search for the pair production of sleptons, leptonically decaying charginos and charged Higgs particles. No evidence for new phenomena is apparent and model independent production cross section limits for the new particles are presented. For a 100% branching ratio for the decay $\tilde{\ell}^{\pm}_R \to \ell^{\pm}\tilde{\chi}^0_1$, where $\tilde{\chi}^0_1$ is the lightest neutralino, the following are excluded at 95% CL: right handed smuons with masses below 94.0 GeV for $m_{\tilde{\mu}} - m_{\tilde{\chi}^0_1} > 4$ GeV and right handed staus with masses below 89.5 GeV for $m_{\tilde{\tau}} - m_{\tilde{\chi}^0_1} > 8$ GeV. Right-handed selectrons are excluded at 95% CL for masses below 97.5 GeV for $m_{\tilde{e}} - m_{\tilde{\chi}^0_1} > 10$ GeV, within the framework of the Minimal Supersymmetric Standard Model for $\mu < -100$ GeV and $\tan\beta = 1.5$.

Further comparisons between the data and Standard Model are presented, inspired by new physics scenarios which may lead to final states containing two charged leptons plus missing transverse momentum plus isolated photons, and also events containing two charged leptons with unequal momentum distributions plus missing transverse momentum. The data is found to be in agreement with the Standard Model expectation for both cases.

Declaration

No portion of the work referred to in this thesis has been submitted in support of an application for another degree or qualification of this or any other university or other institute of learning.

The ownership of any intellectual property rights which may be described in this thesis is vested in the University of Manchester, subject to any prior agreement to the contrary, and may not be made available for use by third parties without the written permission of the University, which will prescribe the terms and conditions of any such agreement.

Further information on the conditions under which disclosures and exploitation may take place is available from the Head of the Department of Physics and Astronomy.

The Author

The author was educated at Judd School, Tonbridge, Kent before joining the Department of Physics and Astronomy at the University of Manchester as an undergraduate in September 1994. The work presented here was undertaken at Manchester and CERN, Geneva.

Acknowledgements

I would like to thank my supervisor Terry Wyatt for his excellent supervision, and also Graham Wilson for help and advice while at CERN. Thanks to PPARC who provided me with financial support while undertaking this research. Thanks to all of the friends who helped to make the last three years so enjoyable, and to my parents for supporting me through my many years of study. Also, a special thankyou to Ib for putting up with me disappearing off to Geneva for a year.

Chapter 1

Introduction

The LEP e^+e^- collider at CERN has been instrumental in testing the Standard Model of particle physics. So far, all measurements taken by LEP have been in good agreement with the Standard Model predictions. However, as the energy of the e^+e^- collisions has been successively increased over recent years, into energy regions which have not been tested before, searches for new phenomena also form an important part of LEP physics.

This thesis reports on a search for supersymmetric particles carried out using the LEP e^+e^- collider. Anomalous production of events containing two charged leptons and significant missing transverse momentum, known as *acoplanar lepton pairs*, is looked for. The kinematic properties of the events are used to separate potential signal from Standard Model sources of these events.

Results are presented which combine four years of data taken using the OPAL detector at LEP.

1.1 Thesis outline

This document is organised as follows. In chapter 2 a brief overview of the Standard Model of particle physics is presented, along with some of the unanswered problems that it presents. Supersymmetry may be able to solve some of these problems, and it is introduced in order to motivate the search for supersymmetric particles.

Chapter 3 describes the experimental equipment used in this analysis – the LEP accelerator and the OPAL detector. Particular attention is given to those aspects which limit the sensitivity of the search.

Chapter 4 discusses the acoplanar lepton topology in more detail. The event selections used in this analysis are described and Standard Model processes which form a background to the search are introduced.

The techniques used to separate signal from background events are described in chapter 5. Also mentioned here are the techniques which allow the search to be extended to a wide range of signals and centre of mass energies.

The search results are presented in chapter 6. Chapter 7 contains some additional comparisons between the data and the Standard Model expectation, motivated by signal scenarios where a full search analysis would be too complicated.

1.2 Summary of changes to analysis

Now follows a summary of changes which have been made with respect to the previous published version of the search for new physics using acoplanar lepton pair events. These are the areas where significant new work has been done by the author, which is described in this thesis.

- Extension of analysis to many $\sqrt{s}$ values and calculation of results with about

3 times more integrated luminosity than before (see results section 6).

- Introduction of technique for interpolation of reference histograms in $\sqrt{s}$ (sections 5.5.4 and 5.9.2).
- Introduction into the likelihood of a two dimensional acolinearity versus momentum asymmetry histogram, including methods for smoothing and interpolating 2D histograms (sections 5.2.3, 5.4.2 and 5.5.2).
- Integration of lepton identification using the OPAL Tau Platform, including ambiguous lepton categories (section 5.2.2).
- Integration of additional constraints on leptons entering selectron and smuon search (section 5.2.2).
- Improved interpolation technique for 1D histograms (section 5.5.1).
- Use of signal events from 4 nearest grid points in setting limits at intermediate m and Δm values, instead of one (section 5.6).
- Investigation of signal Monte Carlo statistics systematic error (section 5.9.1).
- Investigation of $\sqrt{s}$ interpolation systematic error (section 5.9.2).

These improvements have resulted in an increase in the sensitivity of the analysis of between 5-20% at intermediate to high Δm (sensitivity at low Δm has been slightly reduced due to changes in the general selection which make the analysis more robust against sources of low p_t^{miss} background where there is significant statistical uncertainty in the Monte Carlo). The improvements in sensitivity come mostly from the changes to the lepton ID and the 2D acolinearity variable.

The additional data / Standard Model comparisons described in chapter 7 are also new work carried out by the author.

Chapter 2

The Standard Model and Beyond

The Standard Model is a theoretical framework which describes all of the fundamental particles which have so far been discovered (see table 2.1), and allows their interactions to be calculated to a high degree of accuracy. In this respect the Standard Model is very successful; this chapter will describe those aspects of it which are most relevant to the present analysis. There are, however, good reasons to think that there may be new physics beyond the Standard Model. The new particle searches described in this thesis are motivated by possible extensions to the Standard Model, which are introduced in section 2.5.

2.1 The Standard Model

In the Standard Model the fundamental particles are represented as three different types of field – the fermion matter fields, the gauge fields and the Higgs scalar fields. The interactions between these fields are described by two gauge theories [1], the Glashow-Salam-Weinberg model of electroweak interactions and quantum chromodynamics (QCD).

		Q	Y
Leptons	$\begin{pmatrix}\nu_{\mathrm{e}}\\ \mathrm{e}\end{pmatrix}_L$ $\begin{pmatrix}\nu_\mu\\ \mu\end{pmatrix}_L$ $\begin{pmatrix}\nu_\tau\\ \tau\end{pmatrix}_L$	0 -1	-1
	e_R μ_R τ_R	-1	-2
Quarks	$\begin{pmatrix}\mathrm{u}\\ \mathrm{d}\end{pmatrix}_L$ $\begin{pmatrix}\mathrm{c}\\ \mathrm{s}\end{pmatrix}_L$ $\begin{pmatrix}\mathrm{t}\\ \mathrm{b}\end{pmatrix}_L$	$+2/3$ $-1/3$	$1/3$
	$\begin{pmatrix}\mathrm{u}\\ \mathrm{d}\end{pmatrix}_R$ $\begin{pmatrix}\mathrm{c}\\ \mathrm{s}\end{pmatrix}_R$ $\begin{pmatrix}\mathrm{t}\\ \mathrm{b}\end{pmatrix}_R$	$+2/3$ $-1/3$	$4/3$ $-2/3$
gauge bosons	γ $\mathrm{W}^{\pm}$,Z^0 $\mathrm{g}_i(i = 1, 8)$	0 $\pm 1, 0$ 0	

Table 2.1: Fundamental particles of the Standard Model.

2.2 The Electroweak Interaction

The electroweak interaction unifies quantum electrodynamics (QED) and the weak interaction as two aspects of the same force. QED is the quantum field theory which describes the forces between electrically charged particles. In QED a vector field is introduced which preserves the invariance of the Lagrangian under local gauge transformations. This vector field is recognized as the photon field. The masslessness of the photon can be understood in terms of the requirement that the Lagrangian remain gauge invariant. The addition of a mass term for the photon would destroy the gauge invariance.

It is observed that the weak interaction is parity violating, in that the weak charged current couples only to left(right) handed particles(anti-particles). This parity violation is built into the electroweak theory by grouping the left handed fermions into an $SU(2)$ isospin doublet, while the right handed fermions form isospin singlets.

The electric charge, Q, of the fermion fields is related to their hypercharge, Y, and their third component of isospin, I_3, by the relation

$$Q = I_3 + \frac{Y}{2}. \tag{2.1}$$

The electroweak interaction combines the electromagnetic and weak interactions into an $SU(2)_L \otimes U(1)$ symmetry group, which has a vector triplet gauge field, $W^i(i = 1, 2, 3)$, and a singlet gauge field B^0. The vector triplet corresponds to the weak isospin current and the singlet field to the weak hypercharge current. This is seen from the covariant derivative which can be written

$$D^\mu = \partial^\mu + igT_iW_i^\mu + \frac{ig'}{2}YB^\mu, \tag{2.2}$$

where g and g' are the weak charges of the $SU(2)_L$ and the $U(1)$ parts of the gauge group respectively.

The physical gauge fields of the W$^\pm$, Z^0 and γ are obtained from linear combinations of the W^i and B^0:

$$W_\mu^\pm = \frac{1}{\sqrt{2}}(W_\mu^1 \mp iW_\mu^2), \tag{2.3}$$

$$A_\mu = B_\mu \cos\theta_W + W_\mu^3 \sin\theta_W, \tag{2.4}$$

$$Z_\mu = -B_\mu \sin\theta_W + W_\mu^3 \cos\theta_W, \tag{2.5}$$

where A_μ is the photon field, Z_μ is the Z^0 field, and θ_W is the weak mixing angle.

2.2.1 Production and decay of W bosons at LEP

W bosons are produced at LEP in pairs via the processes shown in figure 2.1. Each of the W particles may then decay leptonically or hadronically (see figure 2.2). The expected branching ratio for each of these decays are shown in table 2.2, along with the W$^+$W$^-$ branching ratios.

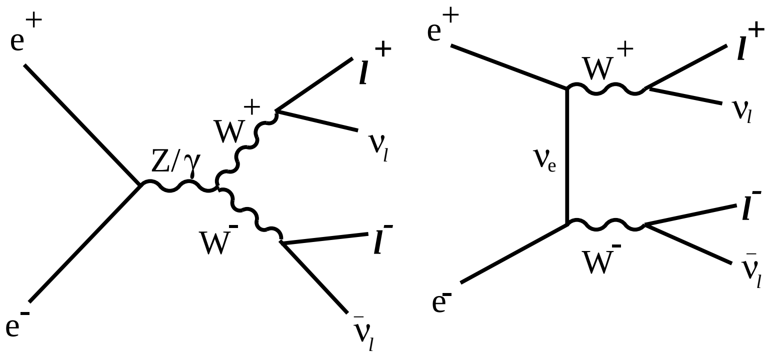

Figure 2.1: W^+W^- production processes.

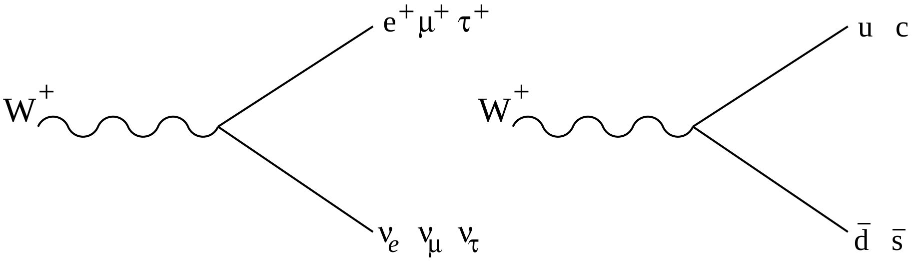

Figure 2.2: Decay modes of the W boson.

BR(W→ qq)	67.5 %
BR(W→ eν_e)	10.8 %
BR(W→ $\mu\nu_\mu$)	10.8 %
BR(W→ $\tau\nu_\tau$)	10.8 %
BR(W^+W^-→ eν_eeν_e)	1.2 %
BR(W^+W^-→ e$\nu_e\mu\nu_\mu$)	2.3 %
BR(W^+W^-→ e$\nu_e\tau\nu_\tau$)	2.3 %
BR(W^+W^-→ $\mu\nu_\mu\mu\nu_\mu$)	1.2 %
BR(W^+W^-→ $\mu\nu_\mu\tau\nu_\tau$)	2.3 %
BR(W^+W^-→ $\tau\nu_\tau\tau\nu_\tau$)	1.2 %
BR(W^+W^-→ $\ell^+\nu\,\ell^-\overline{\nu}$)(ℓ = e,μ, or τ)	10.5%

Table 2.2: Expected W and W^+W^- decay branching ratios (adapted from [2])

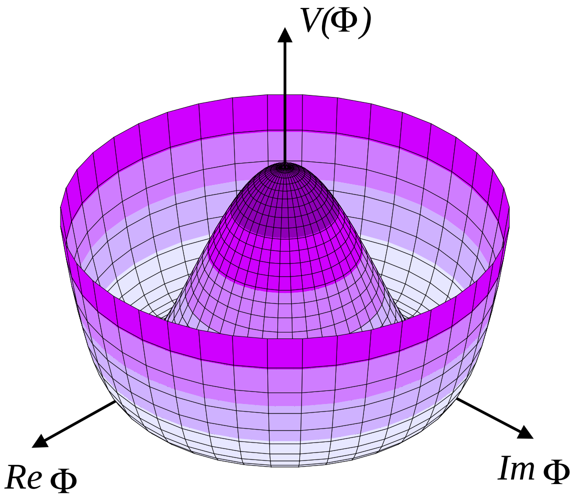

Figure 2.3: The Higgs Potential.

2.3 Spontaneous Symmetry Breaking

It is observed that, in contrast to the photon, the gauge bosons of the weak force are not massless. Indeed measuring the masses of the $W^{\pm}$ and Z^0 has been one of the major activities at LEP. We have seen that introducing a mass term for the photon field would destroy the gauge symmetry of the theory, and the same problem occurs with generating masses for the $W^{\pm}$ and Z^0. The solution to this problem is called spontaneous symmetry breaking, where the symmetry is violated in a more elegant way which preserves invariance under local gauge transformations.

This principle is demonstrated by considering a complex scalar field theory with a mass term and a quartic self-interaction. The Lagrangian for this theory is

$$\mathcal{L} = \partial_\mu \Phi^* \partial^\mu \Phi - V(\Phi), \tag{2.6}$$

where the potential $V(\Phi)$ is given by

$$V(\Phi) = \mu^2 \Phi^* \Phi + \lambda |\Phi^* \Phi|^2. \tag{2.7}$$

If we suppose that the sign of μ^2 is negative then the potential has the form shown in figure 2.3, with a maximum at $\Phi = 0$ and minimum occuring at $\Phi = e^{i\theta}\sqrt{-\mu^2/2\lambda}$, where $0 \leq \theta < 2\pi$. This corresponds to an infinite number of ground states, each with the same lowest energy. Each state is related to another by a $U(1)$ gauge transformation. One of these states is chosen to be the "true" vacuum, thereby spontaneously breaking the $U(1)$ invariance.

If Φ is expanded around its vacuum expectation value as

$$\Phi = \frac{1}{\sqrt{2}}(\frac{\mu}{\sqrt{\lambda}} + H + i\phi), \tag{2.8}$$

and inserted into the potential (equation 2.7), one generates a mass term $\mu^2 H^2$ for the field H. The field ϕ corresponds to a massless Goldstone boson.

This principle of spontaneous symmetry breaking can be applied to the electroweak sector of the Standard Model by choosing Φ to be an $SU(2)_L$ doublet of complex scalar fields. This results in 3 massless Goldstone bosons which are absorbed by the $\mathrm{W}^{\pm}$ and Z^0 as extra degrees of freedom, causing them to become massive. Also a massive scalar field, H, is generated as above – the Higgs boson. The Higgs boson has yet to be observed directly.

2.4 Problems with the Standard Model

While the Standard Model has proved a very successful theory, there are a number of reasons why theoretical physicists believe it is not a fundamental theory, and that there should be more general principles which underwrite it.

The Standard Model contains 3 different gauge groups, $U(1), SU(2)$, and $SU(3)$, each with its own gauge coupling. It is an appealing idea that these are three subgroups of a single large group which generates all the interactions in nature. Such theories, called "Grand Unified Theories" (or GUT's), postulate that the three couplings are only different at the energy scales currently accessible, and that there

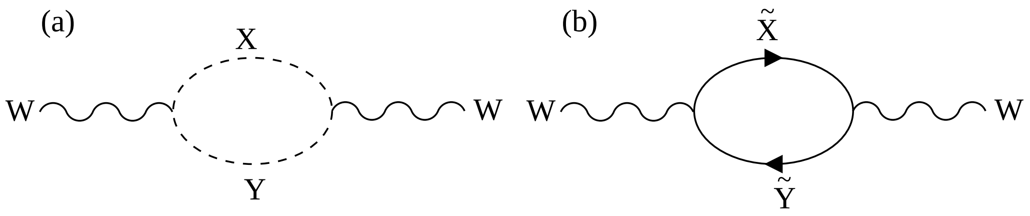

Figure 2.4: Corrections to M_W arising from loops of very massive (a) X and Y bosons, (b) fermionic superpartners of the X and Y bosons.

exists some energy scale, M_{GUT}, where the couplings coincide. Current experimental limits require $M_{GUT} > 5 \times 10^{15}$ GeV (from measurements of the proton lifetime). This would lead to new particles with masses of this order. However, when the Standard Model couplings are extrapolated to large energies of order M_{GUT}, they are found not to coincide. Grand Unified Theories also provide a framework for incorporating gravity, which is missing from the Standard Model.

One question associated with Grand Unification, called the "hierarchy problem", is why is there such a large gap between the scale of weak symmetry breaking ($\sim M_W$) and the GUT scale?

There is also a technical problem caused by higher order corrections to the lighter masses from loops containing much heavier particles. Consider the corrections to the W-mass arising from a loop of X and Y bosons having mass $\sim M_{GUT}$ (see figure 2.4a).

This diagram gives a contribution to M_W of order $\delta M_W^2 \sim \alpha M_{GUT}^2$, which is 10^{12} times larger than M_W itself, despite the factor of α (coupling constant $\sim 10^{-2}$) outside. Corrections this large would require the "bare" W mass, M_W^0 to be tuned to an incredible accuracy, for the W to end up with its observed mass of around 10^2 GeV. Requiring the gauge boson masses to have this degree of fine tuning seems unnatural, hence this problem is called the "naturalness problem".

Assuming no new physics between the electroweak scale and the GUT scale offers no answer to the hierarchy or naturalness problems.

Another unappealing feature of the Standard Model is its incompleteness. It contains at least 19 free parameters, and many unanswered questions such as why the left handed fermions come in $SU(2)$ doublets while the right handed fermions are singlets, and why there are only three generations of fermions. The Standard Model also fails to address some questions of cosmological importance. Astronomers report that the majority of mass in the universe is made up of non-baryonic "dark matter", thought to consist of stable weakly interacting massive particles (WIMPS) with masses of order 50 to 500 GeV [3]. There are no candidates for such a particle in the Standard Model. The observed baryon asymmetry in the universe is not explicable within the Standard Model [4] and, most tellingly of all, the Standard Model does not include gravity. This means that new physics is required at the Planck scale, where gravitational effects become important ($M_{Planck} = \sqrt{\hbar c^5/G} = 1.22 \times 10^{19}$ GeV).

2.5 Supersymmetry

Supersymmetry (SUSY) [4] is a symmetry which links bosons and fermions. It is thought to be the last possible symmetry of the particle scattering matrix [5], and this alone is enough to argue that it must be important in physics.

In supersymmetry all bosons have a fermionic partner and all fermions have a bosonic partner. Supersymmetry transformations cause transitions between the boson and fermion states (and vice versa). The first consequence of supersymmetry must be the postulation of new particles – the superpartners of the Standard Model particles [1].

The names of the superpartners to the fermions are constructed by prefixing the

---

[1] It is not possible to construct a supersymmetric model with Standard Model particles alone, because the known bosons and fermions have different conserved quantum numbers.

Particle	Spin	Spartner	Spin
quark: q	$\frac{1}{2}$	squark: $\tilde{q}$	0
lepton: ℓ	$\frac{1}{2}$	slepton: $\tilde{\ell}$	0
photon: γ	1	photino: $\tilde{\gamma}$	$\frac{1}{2}$
W	1	wino: $\tilde{W}$	$\frac{1}{2}$
Z	1	zino: $\tilde{Z}$	$\frac{1}{2}$
Higgs	0	higgsino:$\tilde{H}$	$\frac{1}{2}$

Table 2.3: Standard Model particles and their supersymmetric partners.

fermion name with an “s”. The name of the superpartner to a boson is found by appending the boson name with “-ino”. Standard Model particles and their supersymmetric partners are shown in table 2.3.

Supersymmetry is a popular theory because it provides answers to some of the problems with the Standard Model discussed in section 2.4.

Supersymmetry provides a way out of the naturalness problem because higher order corrections due to loops of ordinary particles are cancelled out by corrections due to loops of the superpartner particles (see fig 2.4b). Supersymmetry also provides a natural candidate for the WIMP’s – the neutralino (see section 2.5.3). Further motivation in favour of supersymmetry comes from the running of the standard model coupling constants to M_{GUT}. When supersymmetric corrections are included, the coupling constants coincide, as required by Grand Unification. Also Grand Unified Theories can predict the value of $\sin\theta_W$. However the prediction is in much better agreement with the experimentally observed value if supersymmetry is assumed [4].

2.5.1 Supersymmetry breaking

If supersymmetry were an exact symmetry then the supersymmetric particles would have the same mass as their partners. This is observed not to be the case since no supersymmetric particles have so far been observed. Hence supersymmetry must be a broken symmetry, thus causing a splitting between the masses of the Standard Model particles and their supersymmetric counterparts.

One of the strongest arguments in favour of supersymmetry is its solution to the naturalness problem. The cancellation of higher order corrections between particles and their superpartners is only exact if both particles have the same mass, however the resultant corrections remain small provided the masses are not too different. This leads us to the conclusion that the scale of supersymmetry breaking must be low. Indeed, if we require that higher order corrections to the "bare" W-mass remain of the order of the observed M_W (thus avoiding the need for fine-tuning the bare mass), then the scale of supersymmetry breaking must be around 1 TeV or less. Supersymmetric particles should be discovered with mass $\sim$ 1 TeV or less for the naturalness argument in favour of supersymmetry to remain valid.

It is typically assumed that the supersymmetry breaking occurs in some "hidden" sector of new particles (which have no interactions with the Standard Model particles), and is transferred (or mediated) to the "visible" sector of Standard Model and SUSY particles by one of the known interactions. The two most popular scenarios are gravity mediation and gauge mediation.

2.5.2 Structure of the MSSM

The minimal supersymmetric extension of the Standard Model (MSSM) consists of taking the Standard Model and adding the corresponding superpartners. The MSSM also contains two Higgs doublets instead of one, which is the minimum required to generate mass for both "up" and "down" type quarks in a supersymmetric theory. All renormalisable supersymmetric interactions consistent with global $B - L$ conservation (B and L are baryon and lepton number respectively) are included, as are the most general soft supersymmetry breaking terms [6].

Because $B - L$ invariance is required, the MSSM is R-parity conserving, where $R = (-1)^{3(B-L)+2S}$ for a particle with spin S. According to this definition, Standard Model particles have even R-parity while supersymmetric particles have odd R-parity. This has important consequences for the phenomenology of supersymmetric processes, as explained in section 2.5.3.

MSSM Higgs sector

The MSSM higgs sector contains 2 higgs doublets, leading to 8 real degrees of freedom. Three of these are taken up by the $\mathrm{W}^{\pm}$ and Z as in the Standard Model, which leaves 5 physical Higgs bosons: a pair of charged higgs ($\mathrm{H}^{\pm}$), two CP-even neutral higgs (h^0 and H^0), and one CP-odd neutral higgs (A^0). Two important MSSM parameters relate to the higgs sector. μ is the supersymmetric higgs mass parameter, and $\tan\beta = v_1/v_2$ is the ratio of the vacuum expectation values for the two higgs doublets. Note that their sum, $v_1^2 + v_2^2 = 246\ \mathrm{GeV}^2$ is fixed by M_W, but their ratio is a free parameter.

Sleptons

Superpartners to the charged leptons are the sleptons ($\tilde{\mathrm{e}}^{\pm}, \tilde{\mu}^{\pm}, \tilde{\tau}^{\pm}$). The left and right handed leptons each have an associated slepton, $\tilde{\ell}_L$ and $\tilde{\ell}_R$. Here the subscripts L and R denote which lepton state the particle partners (and therefore its electroweak couplings), not the handedness of the slepton (the slepton is a scalar particle, remember). The $\tilde{\ell}_L$ and $\tilde{\ell}_R$ do not in general have the same mass, and can mix because they have the same quantum numbers. This mixing turns out to be unimportant for $\tilde{e}$ and $\tilde{\mu}$, but may be important for $\tilde{\tau}$ if $\tan\beta \gg 1$.

Charginos and Neutralinos

The superpartners to the electroweak gauge ($W^{\pm}$, Z^0, γ) and higgs ($H^{\pm}$, h^0, H^0, A^0) bosons (the *gauginos* and *higgsinos*) can mix. The physical mass eigenstates are model-dependent linear combinations of these states – 4 neutral particles called neutralinos ($\tilde{\chi}^0_i, i = 1, 4$) and 2 charged particles called charginos ($\tilde{\chi}^{\pm}_{1,2}$).

2.5.3 SUSY phenomenology

This section will discuss possible signatures of supersymmetric particle production at LEP.

R-parity conservation (introduced in section 2.5.2) has three very important consequences:

- supersymmetric particles are always produced in pairs.
- supersymmetric particles must decay to other, lighter supersymmetric particles.
- the lightest supersymmetric particle (LSP) must be stable (because it cannot decay without violating R-parity conservation).

This last point allows us to infer that the LSP must be electrically neutral and weakly interacting. Otherwise it would have been detected by now. The identity of the LSP depends on the type of SUSY model. In models with gravity mediated supersymmetry breaking the gravitino mass is of the order of the electroweak symmetry breaking scale, while its couplings are gravitational in strength. This gravitino plays no part in SUSY phenomenology, and the favoured candidate for

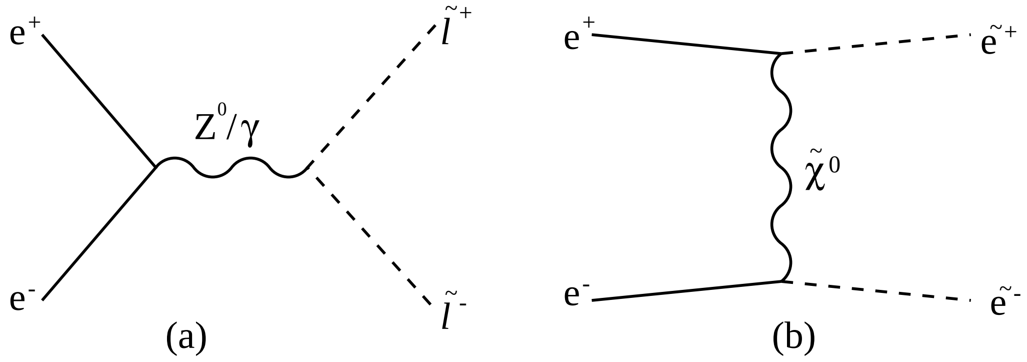

Figure 2.5: Production of slepton pairs at LEP (a) s-channel, (b) t-channel neutralino exchange (selectrons only).

the LSP is the lightest neutralino. This is the scenario which is assumed for the majority of this thesis. The situation is different for gauge mediated supersymmetry breaking models, and these are discussed in sections 2.5.4 and appendix C.

Since all supersymmetric particles will decay to the stable LSP, any process involving supersymmetric particles will have LSP's in the final state. Since the LSP is only weakly interacting, it will not interact in conventional particle detectors. This leads to a missing energy signature of supersymmetry.

Sleptons

Sleptons can be produced in pairs at LEP by the process shown in figure 2.5a. The cross-section for this process, $\sigma(\mathrm{e}^+\mathrm{e}^- \to \tilde{\ell}^+\tilde{\ell}^-)$ is proportional to β^3/s, where s is the centre of mass energy squared and β is the slepton velocity [7]. This means that the cross section is suppressed close to the kinematic limit where the slepton velocity is small.

Selectrons can also be produced by t-channel neutralino exchange (see figure 2.5b). This enhances the selectron production cross section, and also modifies the angular distribution. The significance of this effect is sensitive to the nature of the neutralino, but generally the angular distribution is enhanced in the forward direction ($-q\cos\theta = +1$, where q is the charge of the selectron).

For the case of a neutralino LSP and slepton NLSP (next to lightest supersymmetric particle), the slepton will decay via the process $\tilde{\ell} \rightarrow \ell\tilde{\chi}^0_1$. This creates a signature of 2 leptons plus missing energy.

Charginos

Charginos ($\tilde{\chi}^{\pm}$) can be pair produced in e^+e^- collisions by either s-channel γ^* or Z^{0*} exchange, or via t-channel $\tilde{\nu}$ exchange. The t-channel process causes an enhancement of the cross-section in the forward direction, and its significance varies depending on the composition of the chargino.

The cross-section is proportional to β/s, hence the suppression close the kinematic limit is less significant than with sleptons.

Two different decay schemes for the chargino are searched for in this analysis. If the $\tilde{\nu}_\ell$ is lighter than the chargino then the "two-body" decay $\tilde{\chi}^{\pm} \rightarrow \tilde{\nu}_\ell \ell^{\pm}$ will dominate. The $\tilde{\nu}_\ell$ decays invisibly to $\tilde{\chi}^0\nu_\ell$. The kinematics of this decay are analogous to the 2-body slepton decay to $\ell\tilde{\chi}^0$.

Alternatively, if the $\tilde{\nu}_\ell$ is heavier than the chargino, then the chargino may decay by the "three-body" process $\tilde{\chi}^{\pm} \rightarrow \tilde{\chi}^0\ell^{\pm}\nu_\ell$. Both of these decays are shown in figure 2.6. The observed leptons from the three-body decays tend to have lower energy due to the extra neutrino in the decay chain.

Charged Higgs

The charged Higgs is produced in e^+e^- collisions by s-channel γ^* or Z^{0*} exchange. The production cross-section varies proportional to β^3/s. The Higgs field couples most strongly to particles with high mass, hence the charged Higgs decays dom-

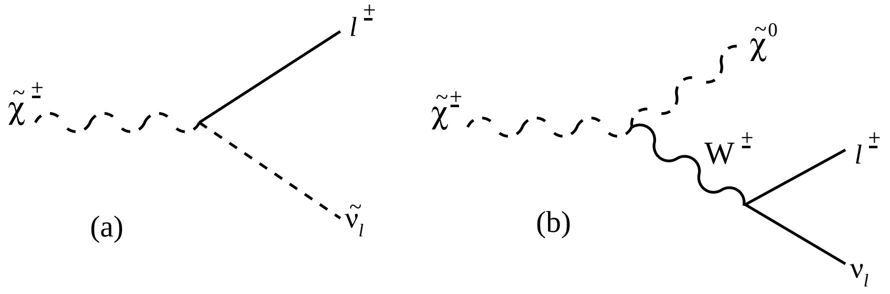

Figure 2.6: Possible decay modes of the chargino (a) two-body (b) three-body.

inantly to c$\bar{\text{s}}$ or $\tau^{\pm}\nu_{\tau}$ (the decay to c$\bar{\text{b}}$ is strongly suppressed by the small CKM matrix element V_{cb} [8]).

2.5.4 Gauge mediated SUSY models

In models with gauge mediated supersymmetry breaking (GMSB) the gravitino is effectively massless, making it the LSP. If the slepton is the NLSP then it can decay via the process $\tilde{\ell} \rightarrow \ell\tilde{\text{G}}$. This decay creates a signature identical to that with a neutralino LSP of zero mass, which the analysis described in this thesis is sensitive to.

The coupling of the slepton to the gravitino may be rather smaller than its coupling to the neutralino, hence the slepton lifetime can be significant. It may be possible to measure the flight and decay points of the actual slepton, instead of just its decay products. In order to carry out a complete search one should be sensitive to all values of the slepton lifetime, and the analysis described in this thesis (which is sensitive to sleptons with zero or very short lifetime) should be combined with searches for long-lived sleptons. This has been done and results are shown in appendix C.

Another possibility is for the slepton to decay to lepton plus neutralino, followed by the neutralino decay $\tilde{\chi}^0_1 \rightarrow \tilde{\text{G}}\gamma$, which would produce two leptons and missing energy plus isolated photons in the final state. This topology is considered in section 7.2.

Chapter 3

LEP and the OPAL Detector

3.1 The LEP Accelerator

The LEP machine [9] at CERN is the largest particle accelerator ever built. It is 27 km in circumference, buried about 100 m underground, near to Geneva in Switzerland. Bunches of electrons and positrons circulate in opposite directions as they are accelerated to almost the speed of light.

The acceleration of the particles takes place in several stages. Electrons are first accelerated by a linear accelerator to 500 MeV. Positrons are obtained from bremsstrahlung photons produced when an electron beam is collided with a heavy metal target. Both types of particle are then stored and further accelerated to 3.5 GeV in the PS accelerator. The electrons and positrons are then passed into the 7 km circumference SPS accelerator which is used as the injector for LEP. Here the particle beams are accelerated further to 22 GeV.

Finally the beams are injected into the LEP (Large Electron Positron) machine, where they undergo final acceleration to the desired physics energy. Once this has been reached, the beams are brought into collision at four interaction points around

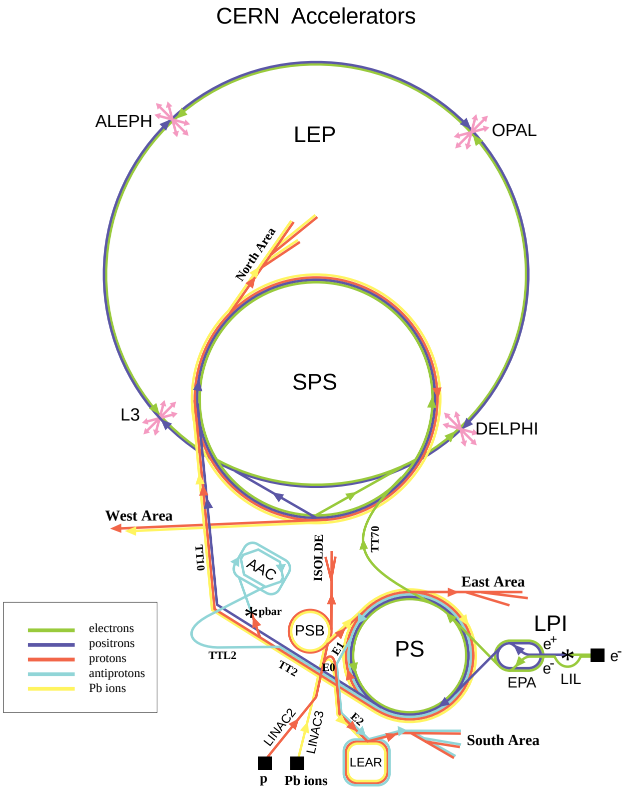

LEP: Large Electron Positron collider
SPS: Super Proton Synchrotron
AAC: Antiproton Accumulator Complex
ISOLDE: Isotope Separator OnLine DEvice
PSB: Proton Synchrotron Booster
PS: Proton Synchrotron
LPI: Lep Pre-Injector
EPA: Electron Positron Accumulator
LIL: Lep Injector Linac
LINAC: LINear ACcelerator
LEAR: Low Energy Antiproton Ring

Rudolf LEY, PS Division, CERN, 02.09.96

Figure 3.1: The CERN accelerator complex.

the ring, inside the particle detectors of the four experiments ALEPH, DELPHI, L3 and OPAL (see figure 3.1).

The LEP accelerator has been used primarily in two modes. In LEP1 (from 1989-1995) the beam energy was tuned to the Z^0 resonance at $\sqrt{s} = 91$ GeV to make detailed studies of the Z^0 boson. In LEP2 (1996-2000) the beam energy has been increased year by year above the threshold for W^+W^- production (at $\sqrt{s} = 160$ GeV) and up to a maximum of around $\sqrt{s} = 200$ GeV. This has been a new energy range for e^+e^- colliders, so searches for new phenomena such as the Higgs Boson and

Supersymmetric particles have been very important.

The dataset analysed here was taken between 1997 and 2000 at beam energies ranging from 81.5 GeV to 105 GeV (resulting in a centre of mass energy range of $183 \leq \sqrt{s} \leq 210$ GeV).

The year 2000 was the final year of running for LEP, and the accelerator was run at the limits of its capability to produce the maximum possible beam energy. To achieve this a new strategy called a "miniramp" was used, where the energy of the beams is further increased after they have been brought into collision. This results in small amounts of data being acquired over a range of different energies, rather than all of the data being accumulated at one well-defined energy. This has some implications for the analysis of the data, as explained in chapter 5.

3.2 The OPAL Detector

The OPAL (Omni Purpose Apparatus at LEP) detector is designed to detect all types of event which can result from e^+e^- interactions at LEP. This requires identification and measurement of as many as possible of the particles from those interactions. The detector is hermetic in all ϕ [1] and extends to very small values of θ to minimise the loss of particles close the the beam. It has a layered structure which aims to efficiently identify particles and to accurately measure their position and energy. The OPAL detector is illustrated in Figure 3.2. A description of the various components in OPAL follows, beginning with those located closest to the beam-pipe and working its way outwards. A (much) more detailed description of OPAL can be found in references [10–13].

---

[1] A right-handed coordinate system is adopted, in which the x-axis points to the centre of the LEP ring, and positive z is along the electron beam direction. The angles θ and ϕ are the polar and azimuthal angles respectively.

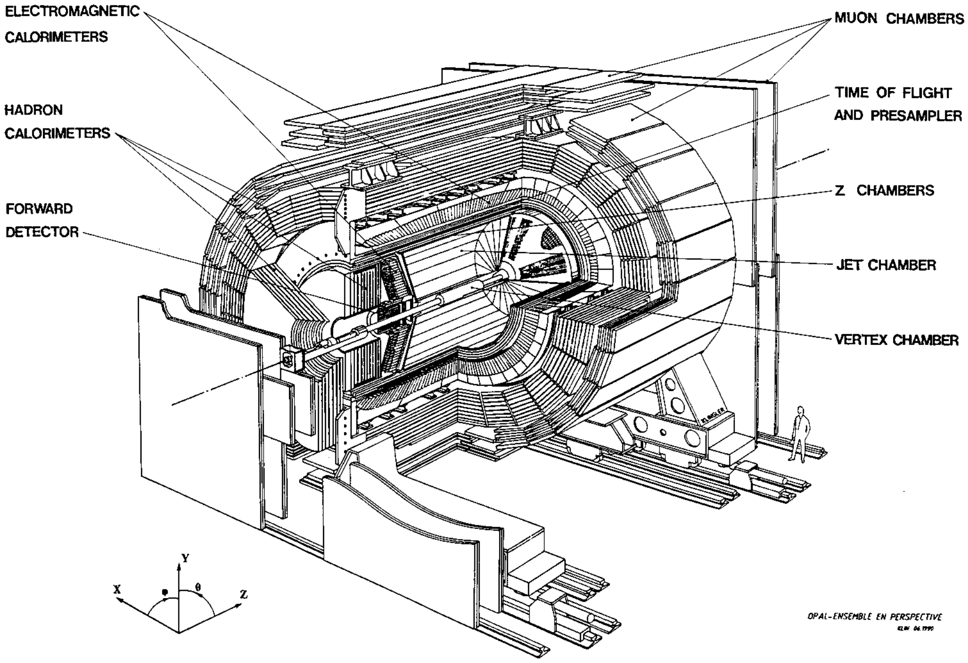

Figure 3.2: The OPAL detector.

3.2.1 Vertex and Tracking Detectors

Vertex and Tracking detectors are used to measure the position of a particle at numerous positions along its path, allowing the trajectory to be calculated.

The vertex detectors in OPAL are designed measure the position of particles as close to the interaction point as possible. This allows one to pinpoint the decay vertices of short-lived particles such as b-quarks, which travel only a few millimetres from the interaction point before decaying. Vertex tagging has become particularly important at LEP2 where Higgs searches are a priority, since the Standard Model Higgs Boson decays preferentially to b-quarks.

The tracking detectors operate in the presence of a 0.435 T axial magnetic field. In addition to measuring particle locations, tracking detectors can provide a momentum measurement, calculated from the the curvature of particle trajectories in the magnetic field.

Silicon Microvertex Detector

The silicon microvertex detector consists of 2 concentric cylindrical layers of silicon wafer strips at radii from the beam of 60.5 mm and 73.8 mm (this is as close to the beampipe as possible) [11]. Using this detector, the impact parameters of particle tracks (ie. how close to the interaction point they pass) can be measured with accuracy $\sigma(d_0) = 15$ μm (in the plane perpendicular to the beam) and $\sigma(z_0) =$ 20-50 μm (parallel to the beam). The ϕ acceptances are 97.8 % and 99.6 % for the inner and outer layers respectively. Polar angle coverage extends to $|cos\theta|$=0.93 for the inner layer and $|cos\theta|$=0.89 for the outer.

Central Vertex Chamber

This is a cylindrical drift chamber 1 m long and 47 cm in diameter. It has two layers both segmented into 36 cells. The cells of the outer layer have a stereo angle of 4° with respect to the inner layer, which has axial wires.

The r/ϕ coordinates of a track are precisely measured with a resolution of 50 μm, and a coarse z measurement is obtained from the time delay between the signals at each end of the wire. Because the outer layer wires are at an angle to the inner layer, the r/ϕ measurements from the two layers can be used to produce a more accurate measurement in z ($\sigma_z \approx 700$ μm).

Jet Chamber

The Jet Chamber is a 4 m long cylinder which surrounds the beampipe and vertex detectors. It has an inner radius of 25 cm and an outer radius of 1.85 m. Radial cathode wire planes divide the chamber into 24 sectors, each containing 159 sense wires. All of the wires are parallel to the beam. The maximum drift distance varies from 3 cm at the inner edge of the chamber to 25 cm at the outside. 159 points are measured along each track in the range $43° < \theta < 137°$, and at least 8 points are measured over a solid angle of 98% of 4π.

The wire position and drift time are used to measure coordinates in r/ϕ with resolution between 120 μm and 240 μm depending on the drift distance. The z coordinate is obtained with relatively low precision ($\sigma_z \approx 6$ cm) from the division of charge between the two ends of the wire.

The momentum of the particle is deduced from the curvature of its track caused by the magnetic field. The transverse momentum, p_T (in GeV), is related to the radius of curvature, R (in m), by $p_T = 0.3\ z\ B\ R$, where z is the charge of the particle in units of the electron charge, and B is the magnitude of the magnetic field in Tesla. The main contribution to the resolution of this momentum measurement comes from the accuracy with which the curvature is measured. This depends on $|cos\theta|$ because tracks in the forward region have fewer points and are therefore less well measured, and also on the p_T of the particle. In the barrel region ($|\cos\theta| < 0.73$) the momentum resolution is described by $\sigma_{pT}/p_T = \sqrt{0.02^2 + (0.0015\ p_T)^2}$ where p_T is in GeV. Good p_T resolution is very important to this analysis as it allows one to accurately measure the net p_T in an event — and hence select events with genuine missing p_T.

The energy loss ($\mathrm{d}E/\mathrm{d}x$) of a particle as it passes through the chamber is also measured by summing the charge deposited at both ends of the wire. This provides a method of particle identification when combined with the momentum of the track.

Z-Chambers

The Jet Chamber provides only a relatively coarse measurement of the z-coordinate, so the Z-chambers are used to provide a precise z measurement as the track leaves the jet chamber. The Z-chambers are 24 drift chambers which form a barrel shaped layer around the Jet Chamber covering the angular region $44^\circ < \theta < 136^\circ$. Each chamber is 4 m long, 50 cm wide and 59 mm thick. They are divided into 8 cells 50 cm long, giving a maximum drift distance of 25 cm in the z direction. The resolution of the z measurement is in the range 100-350 μm depending on the polar angle and the drift distance.

3.2.2 Time-of-Flight System (TOF)

The time-of-flight system forms a barrel outside the magnet coil at a radius of 2.36 m from the beam. It is made of 160 scintillation counters, which provide signals to measure the time-of-flight from the interaction point. The time resolution of this measurement is typically around 0.3 ns (compare to the time for a particle travelling with speed c to reach this radius = 8 ns). This aids the rejection of cosmic rays, and the identification of charged particles in the range 0.6-2.5 GeV.

3.2.3 Calorimeter Detectors

Calorimeter detectors contain a large amount of dense material, which absorbs the energy from most types of particle. They provide position and energy measurements.

When a high energy electron or photon interacts with matter it gives rise to an "electromagnetic shower" of electrons and photons due to the processes of brehmsstrahlung and pair-production. The energy deposited by the shower is measured to give the energy of the incident particle.

Presampler Detectors

The calorimeter detectors aim to absorb and measure all of the energy of a particle. However, there is about 2 radiation lengths of material in front of the calorimeters, and the particle may lose some energy before it reaches them. This material is mostly due to the magnet coil and the jet chamber pressure vessel.

The Presampler detectors are designed to measure the extent to which an electromagnetic shower has developed before it reaches the calorimeter, and thus improve the resolution of the energy measurement.

Electromagnetic Calorimeter

The electromagnetic calorimeter (ECAL) in OPAL detects and measures the energy of electrons, positrons and photons. It is made of lead-glass blocks and is divided into two sections, the barrel and the endcap, which together cover about 98% of the solid angle. As charged particles pass through the lead-glass they radiate Čerenkov light which is detected to give the energy measurement.

The Barrel (EB) is a cylindrical array of 9440 lead-glass blocks arranged so that each block points towards the interaction point. This maximises the probability of a particle only traversing one block. However this pointing geometry is offset slightly to prevent particles from escaping along the gaps between blocks. The Čerenkov light from each block is read out by a phototube. The barrel section is at a radius of 2.45 m and covers the angular range of $|cos\theta| < 0.82$.

The two Endcap (EE) sections contain 1132 lead-glass blocks each. In contrast to the barrel section, these blocks are mounted with their axes parallel with the beam. The endcap must operate in a much larger magnetic field than the barrel, so phototubes are not suitable for readout. Instead single stage multipliers called vacuum phototriodes are used. The endcaps cover the polar angle region $0.81 < |cos\theta| < 0.98$.

Any particle travelling from the interaction point with $|cos\theta| < 0.98$ will encounter at least 20.5 radiation lengths of material in the electromagnetic calorimeter. Electromagnetic showers can be measured with a spatial resolution of about 5 mm, and typical energy resolution of $\sigma_E/E \simeq 5\%/\sqrt{E}$ for the barrel and $\sigma_E/E \simeq 6.3\%/\sqrt{E}$ in the endcaps, where E is the energy in GeV.

Hadron Calorimeter

The Hadron Calorimeter measures particles which penetrate through the electromagnetic calorimeter, which are mainly hadrons and muons. It is a sampling calorimeter made up from iron layers of the magnet return yoke, interspersed with planes of limited streamer tube detectors. The streamer tubes are divided into cells roughly 10 mm square. There are 8 iron layers, each 100 mm thick, in the barrel section and 7 in the endcap. This gives at least 4 interaction lengths of material over 97% of the solid angle.

For energy measurements, the detector cells in different layers are grouped together into towers which divide the solid angle into 976 segments radiating from the interaction region. The signals from all of the layers in each tower are summed to provide an estimate of the hadronic shower energy. Since hadronic showers are likely to initiate before reaching the hadron calorimeter, it is necessary to combine this with measurements from the electromagnetic calorimeter. The hadron calorimeter energy measurements have a relatively poor resolution of $\sigma_E/E \simeq 120\%/\sqrt{E}$.

The hadron calorimeter makes a more important contribution to the lepton ID, because it can be used to identify muon tracks. Spatial resolution is important for this purpose, and is limited by the cell size of about 10 mm.

3.2.4 Muon Detectors

Located outside the hadron calorimeter, the muon detectors detect any charged particles which penetrate this far. The vast majority of these particles are muons. The probability for a pion not to undergo a strong interaction in the material in front of the muon detectors is less than 0.001 (although secondary particles from hadronic interactions can produce muon chamber hits).

Muons are identified by matching tracks in the central tracking system to hits in the muon detectors.

The barrel section of muon detector (MB) has 110 drift chambers arranged in 4 cylindrical layers of 5 m radius and 10 m long. The endcap (ME) has 4 layers of limited streamer tubes with 10 mm square cells, similar to those of the hadron calorimeter.

Both sections of the detector achieve spatial resolution of 1-3 mm, and together they cover 93% of the solid angle with at least 1 layer of detector. The angular coverage is limited by gaps left for the support structures for the rest of the detector, and for cabling and the beampipe.

3.2.5 Forward Detectors

There are several additional detectors which plug the gaps in the other detectors close to the beam. These are particularly important for identifying events with missing transverse momentum, because high energy particles travelling close to the beam can carry significant amounts of missing momentum.

Silicon Tungsten Detector, Forward Detector and Gamma Catcher

This group of calorimeter detectors is located close to the beam pipe between 2-3 m on either side of the interaction region. They detect and measure electrons and photons at small angles and are principally designed for monitoring luminosity by counting small angle Bhabha scattering events.

Closest to the beam is the Silicon Tungsten detector (SW). It has 19 layers of silicon detectors sandwiched with tungsten plates [12]. It is located around the beampipe at about 2.4 m on either side of the interaction region, and covers the angular region 25 mrad $< \theta <$ 60 mrad. Each layer of silicon consists of 16 wedge shaped detectors each with 64 readout pads. The energy resolution of this detector is $\sigma_E/E \sim 25\%/\sqrt{E}$.

The main component of the forward detector (FD) is the forward calorimeter, which covers the angular region 47 mrad $< \theta <$ 120 mrad.[2] This consists of 35 layers of lead scintillator sandwich, divided into 4 interaction lengths of presampler and 20 interaction lengths of the main calorimeter. There are 16 azimuthal segments, and the azimuthal angular resolution is 1.5°, from the ratio of the signals in adjacent segments. The energy resolution is $\sigma_E/E \sim 17\%/\sqrt{E}$.

The Gamma Catcher (GC) is a ring of lead-scintillator sandwiches which plugs the gap between the forward calorimeter and the endcap electromagnetic calorimeter in the angular region 140 mrad $< \theta <$ 200 mrad.

MIP Plug

The forward calorimeters can detect small angle electrons and photons down to about 25 mrad, but are not sensitive to non-showering particles such as muons. The MIP plug was installed in 1997 to cure this problem [13]. It consists of 2 layers of

---

[2] Hence overlapping with the Silicon Tungsten detector to increase hermeticity.

scintillating tiles covering the angular range 43 mrad $< \theta <$ 200 mrad. The tiles are segmented into either 4 or 8 ϕ sectors. About 97% efficiency for identifying muons is achieved by requiring coincident hits in at least 2 tile layers in the same or adjacent ϕ sectors. This is very important for identifying $\mathrm{e}^+\mathrm{e}^-\mu^+\mu^-$ events which can fake a missing p_T signature.

3.3 Trigger System

Bunch crossings in LEP occur every 22 μs, most of which produce no $\mathrm{e}^+\mathrm{e}^-$ interaction. It is not sensible to try to record the data from every one of these. The job of the trigger system [14] is to make fast decisions to select those crossings where interesting interactions have occurred and to reject background events such as cosmic rays or beam-gas interactions. This reduces the event rate to around 5-15 Hz which can be managed by the data acquisition system. The read out dead-time is about 10 ms, so it is important to keep the background trigger rate as low as possible.

The trigger makes decisions on the basis of coarse signals from the subdetectors, which are divided into two types. "Stand alone" signals such as energy sums or multiplicity counts have relatively high thresholds and can be enough to cause a trigger by themselves. Signals from each subdetector are also coarsely divided into overlapping bins in θ/ϕ. There are 24 bins in ϕ and 6 in θ. The "*theta*/ϕ" signals have lower thresholds but 2 or more signals are usually required with some angular correlation to trigger on the event.

Trigger decisions are made according to a flexible (programmable) combination of stand-alone and θ/ϕ signals.

3.4 Data Acquisition and Event Reconstruction

A positive decision from the trigger causes each subdetector to read out its raw data. The Event Builder collects and assembles the data from each subdetector and passes it to the Filter. The Filter checks the events and performs a simple classification, before they are compressed and written onto optical disks. About 15-35% of triggers are rejected by the filter as background. The compressed size of a multihadron event is typically about 100 Kb at this stage.

Event reconstruction is carried out offline by ROPE (Reconstruction of OPAL Physics Events), after calibration constants for each detector are calculated[3]. The various tracks and clusters which make up each event are reconstructed, and information about them (eg. energy, position) is written in the form of Data Summary Tables (DSTs). Most physics analyses are carried out on the DST level data.

3.5 Event Simulation

Monte Carlo simulations of physics processes are a vital tool in understanding the data from large particle physics experiments such as OPAL. A Monte Carlo event generator typically produces a list of particles present in the final state of an interaction along with their four-vectors (see section 4.3 for details of Monte Carlo processes and generators used in this analysis). The GOPAL program [15] takes the four-vector information on the event and simulates the response of the OPAL detector. GOPAL is based on the GEANT3 simulation package and uses precise geometrical details of the OPAL detector to simulate the interactions of different types of particle as they pass though. The detector responses simulated by GOPAL are output in the same format as the real detector. This allows them to be reconstructed by ROPE and subsequently analysed in the same way as real data.

---

[3] This is done automatically shortly after the data has been collected.

Name	Integrated Luminosity (pb^{-1})	Mean $\sqrt{s}$
183	56.43	182.70
189	183.54	188.63
192	29.33	191.59
196	76.41	195.53
200	76.57	199.52
202	45.54	201.95
205	79.00	205.09
207	124.57	206.48
208	9.03	207.94
All	680.43	–

Table 3.1: The integrated luminosity and mean centre-of-mass energy for each energy bin of the dataset.

3.6 The Dataset

The data analysed in this document was taken between 1997 and 2000. The total integrated luminosity is 680.4 pb^{-1} at centre-of-mass energies between 183 and 208 GeV. The data is split up by centre-of-mass energy into 9 energy bins, details of which are shown in table 3.1 and figure 3.3.

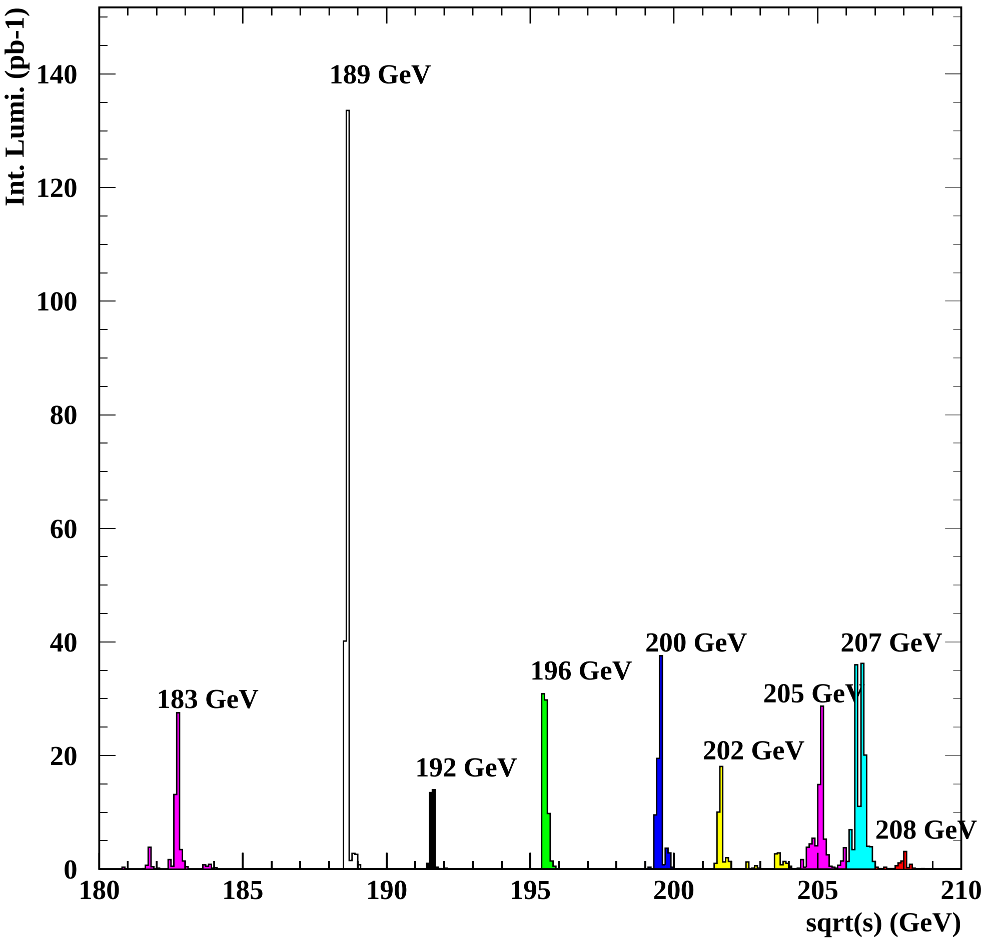

Figure 3.3: Integrated luminosity in each energy bin.

Chapter 4

Acoplanar Lepton Pairs

The dominant Standard Model process leading to lepton pairs with missing transverse momentum is W pair production where the W's decay leptonically ($W^+W^- \to \ell^+\nu\,\ell^-\overline{\nu}$, see figure 2.1). The neutrinos are not observed in the detector and thus lead to missing transverse momentum. Missing *transverse* momentum is required because longitudinal momentum can escape undetected due to particles travelling close to the beam. The missing transverse momentum causes the charged leptons (which are detected) to be acoplanar with the beam direction. When this type of event is viewed in the plane transverse to the beam, the charged leptons are seen to be not "back to back", see figure 4.1. This topology can be used to measure the production of W pair events [16]. However it is also an experimental signature for the pair production of new particles which then decay to a charged lepton and one or more invisible particles. An example of this could be the pair production of charged scalar leptons (sleptons) which then decay to a lepton and a neutralino: $\tilde{\ell}^\pm \to \ell^\pm\tilde{\chi}^0_1$.

This chapter will summarise the event selection which is designed to select all acoplanar lepton events, whatever their source. This is known as the *general selection*, and for its purposes the term "signal" refers to any event which consists of 2 leptons and

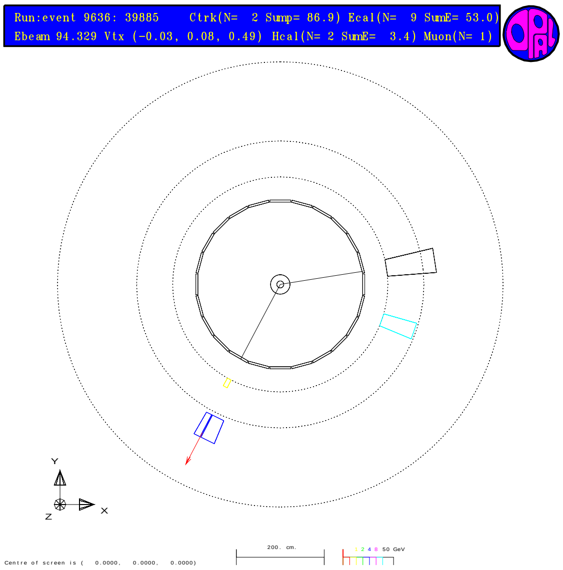

Figure 4.1: An acoplanar lepton pair event containing an electron, a muon, and a photon, as seen in the OPAL detector. The event is viewed in the plane transverse to the beam.

genuine missing transverse momentum, and "background" refers to other standard model processes which may fake this signature.

The event selections described here were developed by Wyatt and Wilson , and are described in [17–19]. The selections are sumarised here because of their importance to the search analysis.

4.1 Event Selection

The general selection is formed by requiring that an event is selected by either or both of two independent event selections, referred to here as selection A and selection B. Selection A is designed to retain efficiency for events with low visible energy.

This is characteristic of slepton or chargino events with small Δm[1]. Selection B is optimised to maximise the efficiency for $\mathrm{W^+W^-} \rightarrow \ell^+\nu\,\ell^-\overline{\nu}$ events, while keeping Standard Model background events to a minimum.

Both selections require evidence for 2 charged leptons and an invisible system carrying significant missing transverse momentum (p_t^{miss}). The maximum p_t^{miss} which can be carried away by undetected particles travelling close the the beam is set by the maximum angle to the beam at which such a particle will not be detected. This is 25 mrad – the angle to which the Silicon Tungsten detector extends. A particle travelling with E_{beam} may thus carry away $p_t^{\mathrm{miss}} = 0.025E_{beam}$ without being detected.

Some background processes containing secondary neutrinos (particularly from tau-decay) may have large values of p_t^{miss} with the direction of the missing momentum vector pointing away from the beam axis. Such events tend to be fairly coplanar, and the component of p_t^{miss} which is perpendicular to the event thrust axis in the transverse plane (called a_t^{miss}) is much less sensitive than p_t^{miss} to the presence of neutrinos from tau-decays or to poorly measured particles. This can be seen by considering electrons produced in tau-decay. Low momentum electrons produced from this source can have a large angle relative to the original tau direction, but their momentum transverse to the original direction (and hence their contribution to a_t^{miss}) is small.

4.1.1 Selection A

Selection A is designed to retain efficiency for events with very low visible energy, but nevertheless significant p_t^{miss}. This is typical of new physics signal events with small Δm. The selection requires evidence that a pair of leptons has been produced

---

[1] Δm is the mass difference between the pair produced supersymmetric particle and its invisible daughter particle.

and of significant missing momentum. Subsequent cuts reduce the probability that the signature of missing momentum is faked by events with secondary neutrinos from tau-decay or poorly measured particles.

At least one lepton in the event is required to be well identified and to satisfy requirements on isolation and transverse momentum. Much looser requirements are made on the possible presence of a second lepton in the event.

Lepton Candidates

The first stage is to look for lepton candidates in the event. A track is identified as a lepton candidate if it has $p > 1.5$ GeV and it is identified as an electron, muon or hadronic tau decay[2]. The electron ID is based on the ratio of ECAL energy to track momentum (E/p), and dE/dx information. Muons are identified using muon chamber or HCAL hits which match to a track in the central detector, or from a high momentum track which matches to a low energy ECAL cluster. To be identified as a hadronic tau the following criteria are applied:

1. Within a cone of half-opening angle 35° there are no more than three tracks.
2. The invariant mass of all tracks and clusters within the cone is less than the tau mass (assuming the pion mass for each track).

The lepton candidates are also required to be isolated. There must be no more than 2 tracks or 2 clusters in an isolation cone defined around the lepton candidate (half opening angle 20° for electrons and muons, half opening angle 60° for hadronic taus), and the energy sum of the tracks or of the clusters must be less than 2 GeV.

---

[2] The lepton ID made at the event selection stage is used for the purpose of the selection only. A separate lepton ID is applied to selected events and used by the search analysis (see section 5.2.2).

Event selection cuts

Firstly evidence for a pair of leptons is required:

- There must be at least one and no more than two isolated lepton candidates with $p_t > 1.5$ GeV.
- If the event contains a second isolated lepton candidate then all charged tracks in the event must be associated with at least one of the lepton candidates.
- If there is only one isolated lepton candidate then the other tracks and clusters in the event are considered as a possible second lepton candidate provided the following:
    (a) There must be between 1 and 3 additional tracks, at least one of which must have $p_t > 0.3$ GeV.
    (b) The invariant mass of the additional tracks must be less than 3 GeV and the invariant mass of the additional tracks plus clusters must be less than 8 GeV.
    (c) $\gamma\beta$, the net momentum of the additional tracks and clusters divided by their invariant mass, is required to be greater than 2.0.

Next, significant missing energy and momentum is required. At large acoplanarity[3] ($\phi_{acop} < \pi/2$ rad) the following cut is applied [4]:

- $x_t > 0.045$ (where $x_t = p_t^{\mathrm{miss}}/E_{beam}$)

---

[3] the acoplanarity angle, ϕ_{acop}, is defined as 180° minus the angle between the two leptons in the transverse plane.

[4] The effect of measurement errors is taken into account in selection A by taking each lepton in turn and fluctuating its momentum up and down by one standard deviation of its estimated measurement error. At each stage the values of p_t^{miss} and a_t^{miss} are recalculated and the minimum of all the values obtained is the one used for comparison to the cut values.

At small acoplanarity ($\phi_{acop} < \pi/2$ rad):

- $x_t > 0.035$
- At small acoplanarity cuts on a_t and θ_a^{miss} (where $\theta_a^{miss} = \tan^{-1}(a_t^{miss}/p_z^{miss})$, and p_z^{miss} is the total momentum of the observed particles in the z direction) are used to reduce background from processes such as $\tau^+\tau^-$ and $\mathrm{e^+e^-}\tau^+\tau^-$. Events are divided into subsets depending on how likely they are to originate from $\tau^+\tau^-$ or $\mathrm{e^+e^-}\tau^+\tau^-$. The cut values vary according to the subset.
    (a) most likely to be $\tau^+\tau^-$ or $\mathrm{e^+e^-}\tau^+\tau^-$: $a_t^{miss}/E_{beam} > 0.025$ and $\theta_a^{miss} > 0.1$
    (b) least likely to be $\tau^+\tau^-$ or $\mathrm{e^+e^-}\tau^+\tau^-$: $a_t^{miss}/E_{beam} > 0.011$ and $\theta_a^{miss} > 0.025$
- $x_t + a_t^{miss}/E_{beam} > 0.070$.

Further cuts are applied to reduce the effect of processes which may fake the signature of missing transverse momentum. These are mostly vetoes against energy in the forward region (GC, FD, SW, or MIP). However care is taken that the activity in the forward region could possibly explain the missing momentum observed. Also different requirements are made depending on the amount of missing transverse momentum observed.

Single lepton selection

Selection A also includes a selection for events with only 1 lepton visible in the central detector, and the other lepton travelling sufficiently close to the beam axis that no track is produced in the central tracking chambers.

The single lepton selection requires:

- The event must contain one and only one identified, isolated lepton candidate, and no other tracks.

- $x_t > 0.16$
- If the lepton is identified as a hadronic tau decay and $\phi_{acop} < \pi/2$ then a_t^{miss} must satisfy $a_t^{miss}/E_{beam} > 0.015$.

In order to veto events which may fake the missing transverse momentum signature, events are rejected if they contain activity in ECAL,GC,FD,SW,ME, or MIP plug which is back-to-back with the observed lepton.

4.1.2 Selection B

Selection B is optimised to select high visible energy events typical of the process $\mathrm{W}^+\mathrm{W}^- \rightarrow \ell^+\nu\,\ell^-\overline{\nu}$. A low multiplicity preselection is applied such that the events contain at least one charged track but no more than 8. Also the sum of the number of charged tracks plus the number of ECAL clusters is required to be less than 16.

A cone-based jet finding algorithm is applied requiring a minimum jet energy of 2.5 GeV and a cone half angle of 20°. Events are required to contain 1,2 or 3 jets, and a separate selection is used for each value of n_{jet}, the number of jets. The majority (about 90%) of $\mathrm{W}^+\mathrm{W}^- \rightarrow \ell^+\nu\,\ell^-\overline{\nu}$ events have $n_{jet} = 2$. One-jet events are usually those where the decay products from one of the W's are poorly reconstructed (for example if the lepton is travelling close to the beam pipe). Three-jet events can occur if there is a high energy photon in the event.

Electron and muon identification, similar to that in selection A, is applied to the most energetic track in each jet. Jets not identified as electrons or muons are classified as hadronic tau decays.

The most important cuts for each n_{jet} class are summarised below.

2-jet selection

1. $\theta_{acol} > 5°$, where θ_{acol} is the acollineartiy angle between the two jets defined in figure 5.6.

2. $x_t > 0.05$. It is further required that the significance by which x_t exceeds 0.05 is greater than 1 standard deviation.

3. For events with acoplanarity angle, ϕ_{acop}, greater than 90° it is required that the direction of the missing momentum satisfies $|\cos\theta_p^{miss}| < 0.95$. For events with $\phi_{acop} < 90°$ it is required that $a_t/E_{beam} > 0.022$ and that $\sin\theta_a^{miss} > 0.06$.

Further cuts are made on the quality of each jet, and for background rejection (mainly for events at low x_t).

- Events are rejected if there are any tracks which are not associated with either jet.

- Events with low x_t ($x_t < 0.15$) are rejected if there is evidence of activity in the MIP plug at the same end and with azimuthal angle within 60° of the missing transverse momentum direction.

3-jet selection

For events classified as tri-jet, significant missing momentum is required:

- The sum of the opening angles among the three 2-jet pairings should be less than 359°.

- x_t of the 3-jet system should exceed 0.05 with a significance exceeding 1 standard deviation.

The most important additional requirements are:

- For $\Delta\phi^{max} > 185°$, the number of jets with associated charged tracks should be 2, where $\Delta\phi^{max}$ is the maximum opening angle between any two jets in the transverse plane.
- For $\Delta\phi^{max} < 180°$, an axis in the transverse plane is defined using the highest p_T charged jet. The event is rejected if the transverse momentum of the neutral jet with respect to this axis exceeds 80% of the transverse momentum of the lowest p_T charged jet. This cut is effective against $\tau\tau\gamma$ events.
- Events are rejected if there is evidence for a particle passing through the MIP plug (similar to di-jet MIP veto but without the directional requirement).

1-jet selection

The single-jet selection applies to events where one high transverse momentum lepton is observed at wide angle with evidence for a partially reconstructed lepton at small polar angle, or events where the two leptons fall within the same cone. In contrast to the single lepton category of selection A, it is required here that there is some activity in the forward region (EE,GC,FD,SW,ME,MIP plug).

Backgrounds from cosmic rays are reduced by requiring in-time TOF hits for tracks in the barrel region, and that the most energetic track in the jet is associated with hits in the silicon micro-vertex detector.

In addition it is required that:

- $x_t > 0.25$.
- There should be evidence of activity in the forward region ($|\cos\theta| > 0.95$).

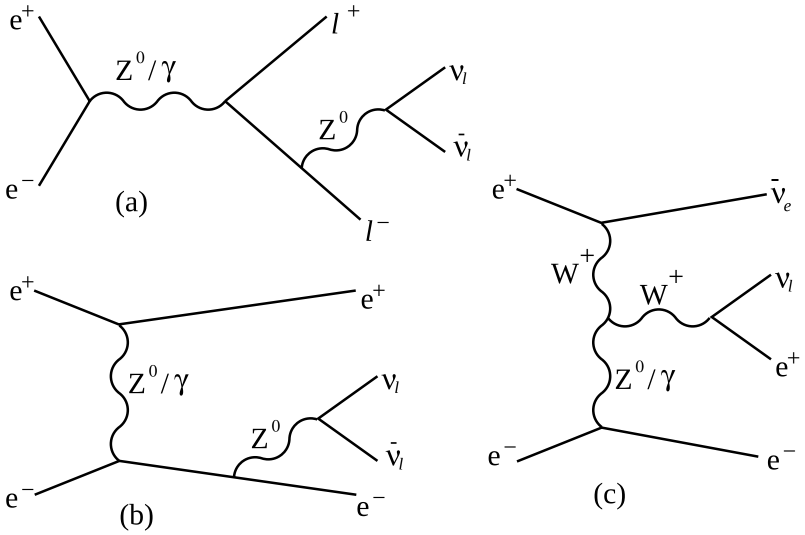

Figure 4.2: 4-fermion processes other than W^+W^- production leading to two charged leptons plus missing transverse momentum. (a) and (b) s and t-channel diagrams (c) Single W or Weν process.

4.2 Selected Processes

Standard Model processes other than W^+W^- production which lead to the $\ell^+\nu\,\ell^-\overline{\nu}$ final state are shown in figure 4.2.

Other Standard Model processes which may fake the signature of 2 leptons plus missing energy are lepton pair production, and two-photon processes. Lepton pairs are produced by the process shown in figure 4.3a, where ℓ can be e,μ,τ, or ν_ℓ (events containing neutrino pairs are only detected if additional photons are radiated from the incoming electrons). Electron pairs can also be produced by the t-channel process shown in figure 4.3b, known as bhabha scattering. The Feynman diagram for two-photon processes is shown in figure 4.4.

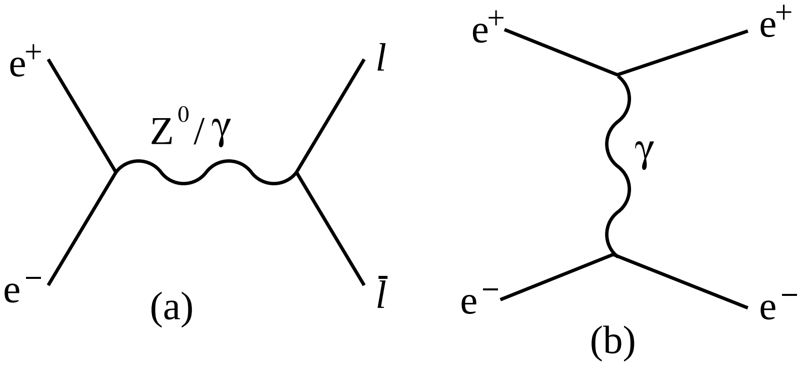

Figure 4.3: Lepton pair production processes.

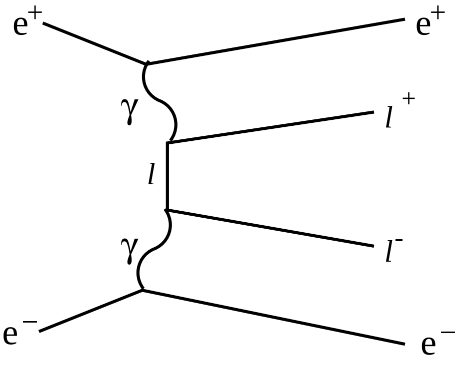

Figure 4.4: Two-photon Feynman diagram.

4.3 Monte Carlo Generators

The following Standard Model Processes are simulated at $\sqrt{s}$ = 189, 192, 196, 200, 202, 206, and 208 GeV. Processes leading to four leptons in the final state (except $e^+e^-\ell^+\ell^-$ states) are simulated together as one sample, known as $\ell\ell\ell\ell$. This study uses $\ell\ell\ell\ell$ samples generated using KORALW [20]. Although these samples include final states with four charged leptons ($\ell^+\ell^-\ell^+\ell^-$), only those with neutrinos ($\ell^+\nu\,\ell^-\overline{\nu}$) are accepted by the acoplanar lepton pair selection cuts. These 4-lepton processes account for 97% of the events selected into the acoplanar lepton pair sample. The predicted W^+W^- cross section from the KORALW Monte Carlo samples has been scaled down by 2.5% in agreement with recent calculations usin the RACOONWW and YFSWW programs [21]. This difference is principally due to their inclusion of non-leading $\mathcal{O}(\alpha)$ initial state radiation corrections.

Processes leading to $e^+e^-\ell^+\ell^-$ final states are simulated as follows. Two-photon processes are generated using the programs of Vermaseren[5] [22] and BDK [23]. Other processes leading to $e^+e^-\ell^+\ell^-$ final states are generated using grc4f [24], as are $e^+e^-q\overline{q}$ final states. Because of the large total cross-section for $e^+e^-e^+e^-$, $e^+e^-\mu^+\mu^-$ and $e^+e^-q\overline{q}$, soft cuts are applied at the generator level to preselect events that might possibly lead to background in the selection of $\ell^+\nu\,\ell^-\overline{\nu}$ final states. No generator level cuts are applied to the $e^+e^-\tau^+\tau^-$ generation.

The production of lepton pairs is generated using BHWIDE [25] and TEEGG [26] for $e^+e^-(\gamma)$, KK2F [27] and KORALZ [28] for $\mu^+\mu^-(\gamma)$, $\tau^+\tau^-(\gamma)$, NUNUGPV [29] and KORALZ for $\nu\nu\gamma(\gamma)$. The production of photon pairs is generated with RADCOR [30].

Slepton pair production and chargino pair production with 2-body decays are generated using SUSYGEN [31]. Chargino pair production with 3-body decays are generated by DFGT [32]. Charged Higgs pair production is generated by HZHA [33]. Signal events are only generated for particular combinations of m and Δm. These

---

[5] The Vermaseren Monte Carlo generator does not simulate radiation of additional photons.

	$\sqrt{s}$ (GeV)						
Process	183	189	196	200	202	204	208
$\tilde{\mathrm{e}}^+\tilde{\mathrm{e}}^-$	1000	1000	-	1000	-	1000	1000
$\tilde{\mu}^+\tilde{\mu}^-$	2000	1000	1000	1000	-	1000	1000
$\tilde{\tau}^+\tilde{\tau}^-$	4000	5000	-	5000	-	5000	5000
$\tilde{\chi}_1^+\tilde{\chi}_1^-$ (2 body)	4000	4000	-	-	4000	-	-
$\tilde{\chi}_1^+\tilde{\chi}_1^-$ (3 body)	4000	4000	-	4000	-	-	4000

Table 4.1: Number of events generated at each mass value for the various signal processes and centre-of-mass energies.

combinations are shown for sleptons in figure 5.10. Table 4.1 summarises the number of events produced at each m, Δm value for the various $\sqrt{s}$ values and search channels.

4.4 Random Occupancy Corrections

An inefficiency in the selection arises from sources such as off-momentum beam electrons or cosmic rays. This "random occupancy" inefficiency is not simulated by the Monte Carlo generators, and its effect is estimated using randomly triggered beam crossings.

The effect is mainly due to activity in the detectors close to the beam (Silicon Tungsten, Forward Detector, and MIP plug). Activity here can cause the event to be vetoed, particularly for events with low missing transverse momentum.

Tracks and clusters from the randomly triggered beam crossings are superimposed onto the Monte Carlo events before the event selection is applied. The effect on the efficiency to select Standard Model $\ell^+\nu\,\ell^-\overline{\nu}$ events is shown in table 4.2 for three

	$p_t^{\rm miss}/E_{beam} < 0.1$	$0.1 < p_t^{\rm miss}/E_{beam} < 0.25$	$0.25 < p_t^{\rm miss}/E_{beam}$
no correction	65.9±1.8 fb	441.8±4.7 fb	1383±8.3 fb
corrected	63.8±1.8 fb	436.3±4.7 fb	1381±8.3 fb
change	3.1±0.5%	1.2±0.1%	0.14±0.02%

Table 4.2: The effect of random detector occupancy on the accepted cross-section for Standard Model $\ell^+\nu\,\ell^-\overline{\nu}$ events at 189 GeV for three separate ranges of missing transverse momentum.

separate ranges of missing transverse momentum.

The random event mixing is applied to all Monte Carlo events for Standard Model and new physics processes.

4.5 Performance of selection

The numbers of events passing the general selection at each centre-of-mass energy in the data are compared to the Standard Model Monte Carlo predictions in table 4.3. The total number of events predicted by the Standard Model is given, together with a breakdown into the contributions from individual processes. The number of events in the data is consistent with the Standard Model expectation, which is dominated by the $\ell^+\nu\,\ell^-\overline{\nu}$ final state arising mostly from W^+W^- production.

Event variables which are used to discriminate between Standard Model and new physics sources of acoplanar lepton events are lepton energy, acolinearity, lepton identification, and $-q\cos\theta$ where q and θ are the lepton charge and polar angle respectively (see section 5.2 for full definitions of these variables). Figure 4.5 compares these variables for the observed data events to the Standard Model expectation. This figure does not include the data collected at 183 GeV. This data was taken in 1997 before the MIP plug was fully functional. Since the MIP plug is very important to the event selection described in this chapter, it was decided not to re-analyse the 183 GeV data. The event selection and the analysis applied to this data is therefore identical to that described in [18] and [19].

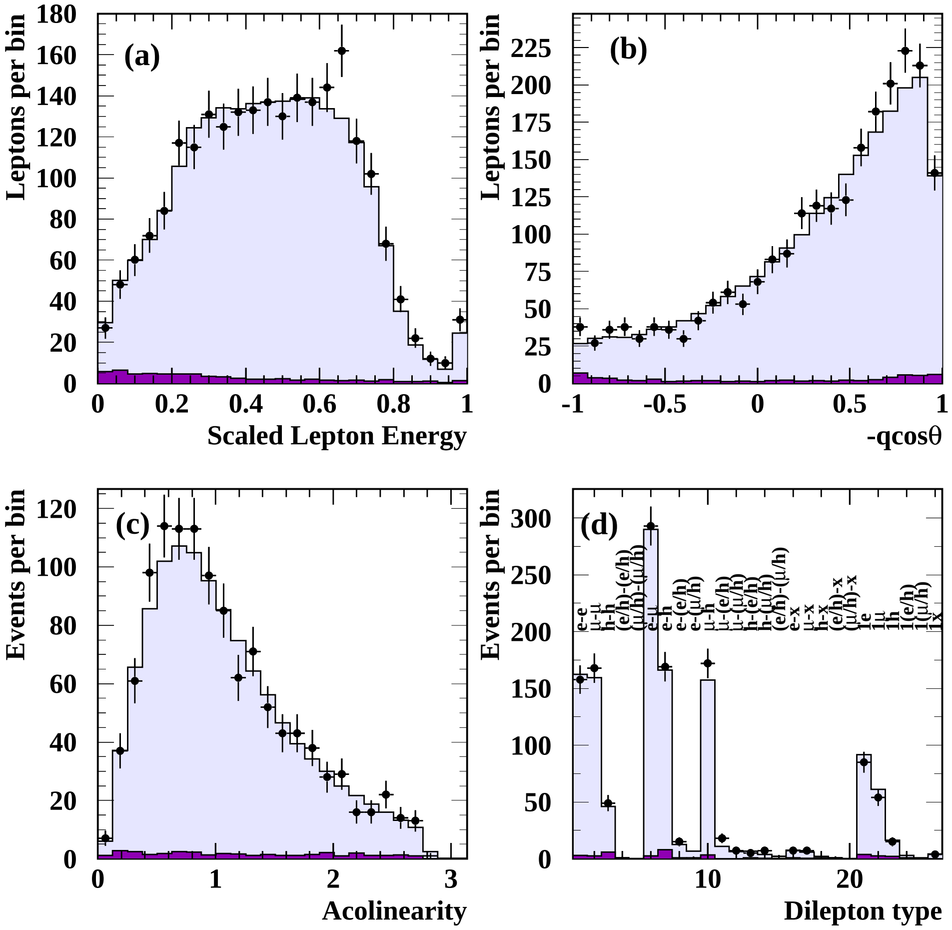

Figure 4.5: Distributions of (a) scaled energy of each lepton (leptons with measured energy larger than E_{beam} are put into the last bin of this histogram). (b) $-q\cos\theta$ of each lepton (c) acolinearity of each event, and (d) dilepton type of each event, for events passing the general selection. The points with error bars show OPAL data collected between 189 GeV and 208 GeV, the light shaded histogram shows the total Standard Model expectation, and the dark shaded histogram shows the expectation from Standard Model sources containing no genuine missing transverse momentum (this shading convention is used throughout this document). See section 5.2 for full definitions of these variables.

$\sqrt{s}$(GeV)	data	SM	$\ell^+\nu\,\ell^-\overline{\nu}$	$\ell^+\ell^-\mathrm{q\overline{q}}$	$\mathrm{e^+e^-}\ell^+\ell^-$	$\ell\ell(\gamma)$	$\nu\overline{\nu}\gamma(\gamma)$
183	78	81.4±0.8	77.5±0.7	0.07±0.03	3.4±0.5	0.31±0.04	0.06±0.03
189	332	348.2±1.9	337.2±1.7	1.6±0.1	3.6±0.7	4.6±0.3	1.1±0.2
192	60	56.1±0.6	54.2±0.6	0.24±0.04	0.64±0.10	0.91±0.18	0.10±0.04
196	166	150.5±1.2	144.7±1.0	0.55±0.06	2.7±0.4	2.1±0.4	0.42±0.05
200	155	153.5±0.9	148.7±0.7	0.72±0.06	1.8±0.3	1.8±0.2	0.45±0.05
202	110	90.6±0.7	87.6±0.6	0.40±0.04	1.4±0.2	0.96±0.14	0.19±0.04
205	154	155.6±1.2	150.8±1.1	0.64±0.07	1.8±0.3	2.0±0.3	0.38±0.07
207	243	249.5±1.4	241.4±1.2	1.1±0.1	3.9±0.6	2.3±0.3	0.64±0.08
208	19	18.2±0.2	17.7±0.2	0.08±0.01	0.17±0.04	0.18±0.03	0.06±0.01
total	1317	1303.6±3.3	1259.8±2.9	5.4±0.2	19.6±1.2	15.2±0.7	3.4±0.2

Table 4.3: Numbers of events passing the general selection in the data, and the expected numbers from each Standard Model Monte Carlo process.

Chapter 5

Search for New Physics

The general selection of events described in chapter 4.1 is designed to select any events which contain a lepton pair and genuine missing transverse momentum. No attempt has been made to distinguish between the potential sources of these events. This chapter will describe the methods used to analyse the generally selected events in order to search for the range of different new physics processes described in section 2.5. From this chapter onwards the term “background” refers to any Standard Model process and “signal” refers to any new physics process.

5.1 Likelihood Method

Several event variables are chosen which contain the information used to separate signal from background. Histograms of these variables are made separately for background processes and each signal process to be considered. These reference histograms are then normalised so that they can be used as probability distributions for an event to have a certain value of each variable.

A signal and background likelihood is constructed for each event by multiplying together the probabilities for each variable. Hence the background likelihood is

$$L_B = \prod_i P_B(x_i), \tag{5.1}$$

and the signal likelihood is

$$L_S = \prod_i P_S(x_i), \tag{5.2}$$

where x_i are the values of the likelihood variables, $P_B(x_i)$ are the background probabilities for each of these values, and $P_S(x_i)$ are the corresponding signal probabilities.

The signal and background likelihoods are then combined into one discriminating variable called the likelihood ratio, L_R, defined as

$$L_R = \frac{L_S}{L_S + L_B}. \tag{5.3}$$

L_R varies between zero and one. It is calculated for each event and the distribution is plotted for signal and background Monte Carlo events and the OPAL data (see example in figure 5.1). The background distribution tends to be peaked towards zero, while the signal distribution is peaked towards one. These L_R distributions form the basis for testing compatibility between data and Monte Carlo and also for setting limits on signal cross sections (see section 5.8).

This method does not take into account correlations between the likelihood variables, so it is less sensitive than using an n-dimensional reference histogram (where n is the number of likelihood variables). To do this would be impractical because a very large amount of Monte Carlo would be necessary to populate such a histogram. However, some attempt is made to retain information about the correlations between likelihood variables — this is explained in sections 5.2.1 and 5.2.3.

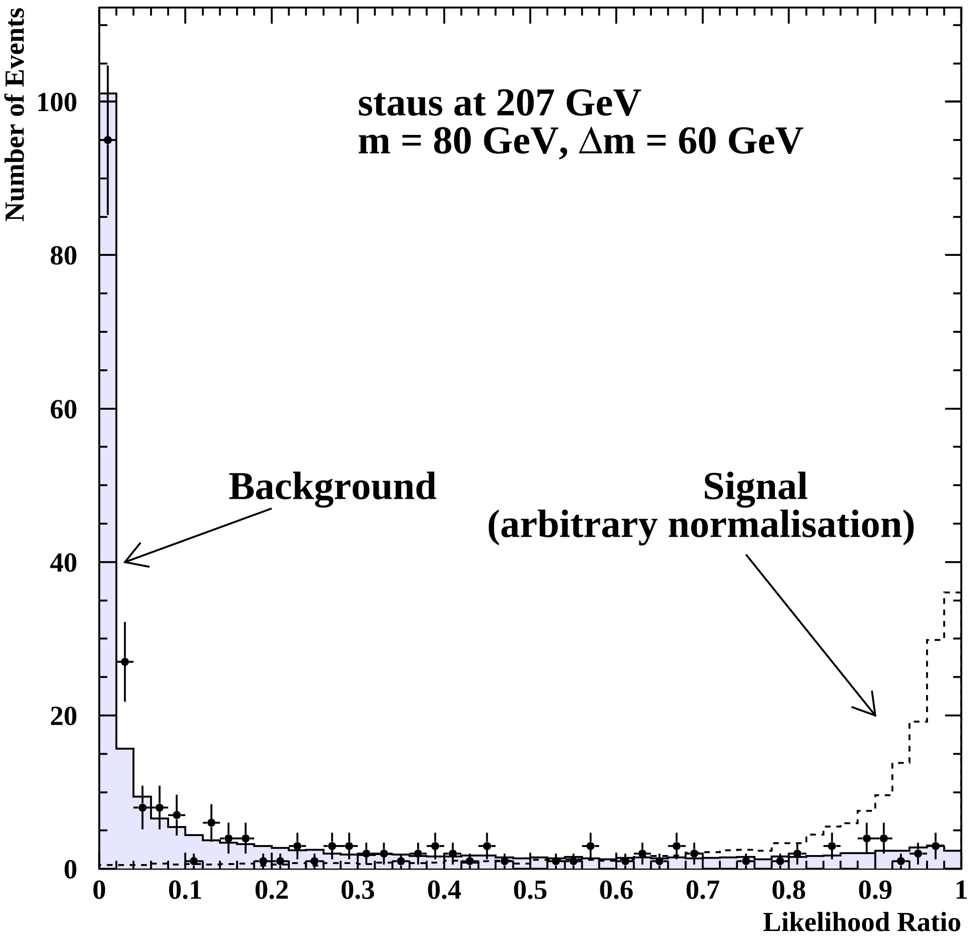

Figure 5.1: Example likelihood ratio distributions for staus at $\sqrt{s}$=207 GeV with m = 80 GeV and Δm = 60 GeV, for data, background and signal.

5.2 Likelihood Variables

5.2.1 Scaled Lepton Momentum

The momentum of the leptons in the event is perhaps the most important variable used to isolate potential signal events. This is because the signal momentum distributions vary widely depending on the mass of the pair produced particle (slepton, chargino or charged higgs) and the mass difference, Δm, between it and its daughter (neutralino, sneutrino or neutrino). The scaled lepton momentum, x, is defined as

$$x_{lepton} = \frac{P_{lepton}}{E_{beam}}. \tag{5.4}$$

The scaled lepton momentum is used here in order to reduce sensitivity to small differences in the beam energy.

Variation with Δm

When Δm is small most of the energy of the pair-produced particle is taken by the mass of the invisible daughter, leaving only a small amount of energy for the observed lepton. This results in a very narrow momentum distribution at low values. As Δm increases the energy available to the observed lepton increases, so the momentum distribution moves to higher values.

Variation with m

The effect of $m_{slepton}$ on the momentum distribution has to do with the Lorentz boost given to the lepton in the slepton decay. The sleptons are produced back-to-back in the lab frame, with their momentum determined by the difference between the centre-of-mass energy and the energy required to produce the slepton pair (ie., $2m_{slepton}$).

Each slepton then decays to a lepton and neutralino. In the rest frame of the slepton this decay is back-to-back and mono-energetic. Hence in the case of high mass sleptons, which are produced almost at rest, the lepton energy spectrum is a narrow peak at a value determined by the kinematics of the decay.

At lower slepton mass the slepton rest frame has a considerable boost compared to the laboratory frame. This causes the lepton energy to be smeared into a broader distribution. Figure 5.2 shows the momentum distributions for data, Standard Model background and signal with various combinations of m and Δm. Leptons with measured energy larger than E_{beam} are put into the last bin of the lepton energy histogram.

Subdivision of Momentum Histograms

The momentum reference histograms are subdivided into several different classes. This retains sensitivity to features of the momentum distribution which are specific to certain types of events. Each lepton is classified according to its ID, the acolinearity of the event[1], and whether it is the higher or lower momentum lepton in the event. Then it is compared to the appropriate reference histograms.

In the stau, chargino and charged higgs searches, the leptons are divided into those identified as e or μ and those identified as hadronically decaying taus. In the selectron and smuon searches this distinction is not made because only leptons identified as electrons or muons are considered (see section 5.2.2). Leptons are also divided depending on whether they are the higher or lower momentum lepton in the event.

Events are also divided into three ranges of acolinearity. This is because of the strong correlation between the lepton momentum distributions and the acolinearity of the event. This can be understood in terms of the Lorentz boost given to the

---

[1] Defined in section 5.2.3.

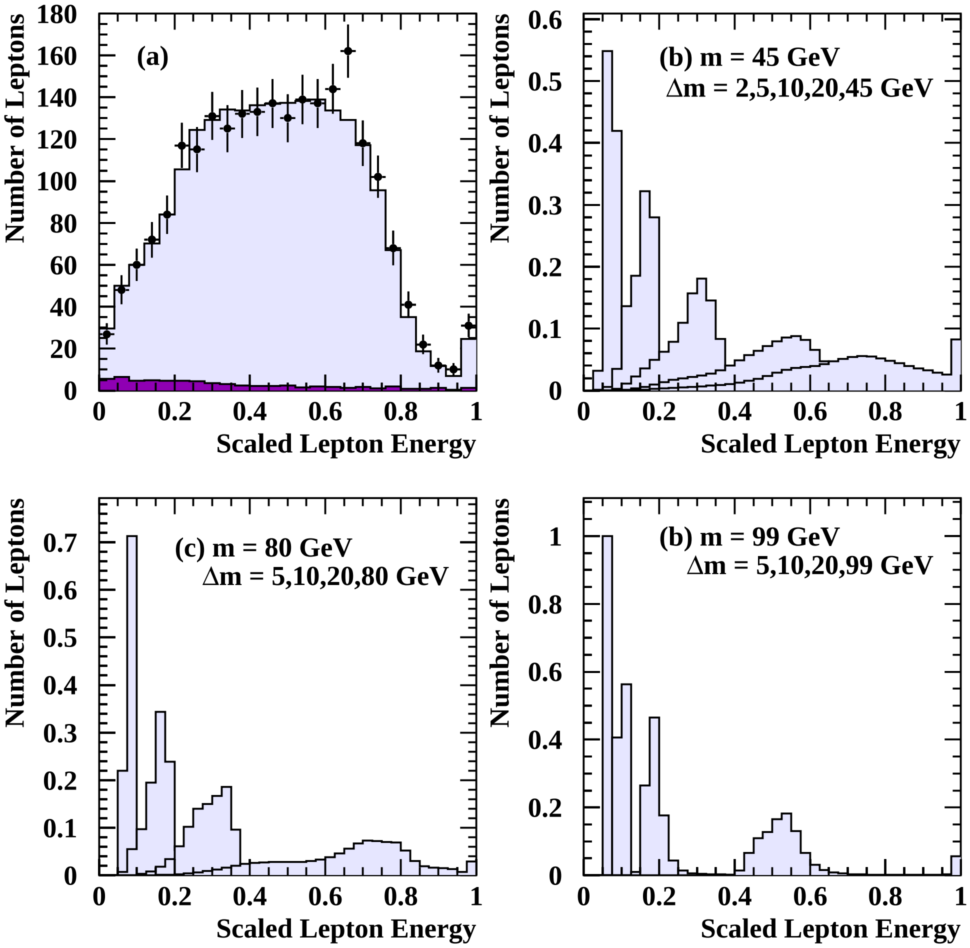

Figure 5.2: Momentum distributions for (a) data at $\sqrt{s} = 189 - 208$ GeV (points with error bars) and Standard Model background (the light shaded histogram represents the total standard model background, the dark shaded histogram shows the contribution from Standard Model sources containing no genuine missing transverse momentum) (b) smuon signal at $\sqrt{s}$=200 GeV with m = 45 GeV (c) smuon signal m = 80 GeV (d) smuon signal m = 99 GeV

leptons by their parent particles. The maximum boost is given to the daughter lepton when the decay angle between parent and daughter is small. Hence events with low acolinearity, where both leptons are travelling close to the direction of their parent particle, tend to have higher momentum leptons.

Conversely, events with high acolinearity are likely to have at least one lepton with a large decay angle relative to its parent. This results in the lepton's momentum being reduced in the lab frame.

The three acolinearity ranges used are (in radians) $0 < \theta_{acol} \leq 0.8$, $0.8 < \theta_{acol} \leq 1.6$, and $1.6 < \theta_{acol} \leq 3.15$. The differences between momentum distributions in these ranges are illustrated in figure 5.3.

5.2.2 Lepton ID

The type of leptons observed in each event provides a very powerful way of reducing background. For example, in the SUSY model being considered, selectrons always decay to an electron and a neutralino. Since the selectrons are produced in pairs this means that selectron events always contain two electrons plus missing energy.

If we were able to identify the leptons perfectly then we could only accept events with two electrons, and reject all other events as background. This cut would reject about 90 % of the $\mathrm{W}^+\mathrm{W}^- \rightarrow \ell^+\nu\,\ell^-\overline{\nu}$ background (see table 2.2 in section 2.2.1). A similar cut could be made in the smuon channel — where two muons would be required.

In the stau, chargino and charged Higgs searches the final state leptons can be of any type, so it is not sensible to simply reject any events based on their lepton ID. However the lepton ID is still a powerful tool for separating signal from background. For example, stau pair events always contain two tau-leptons which may each decay to an electron, a muon or hadrons. Taking into account the branching ratio for each

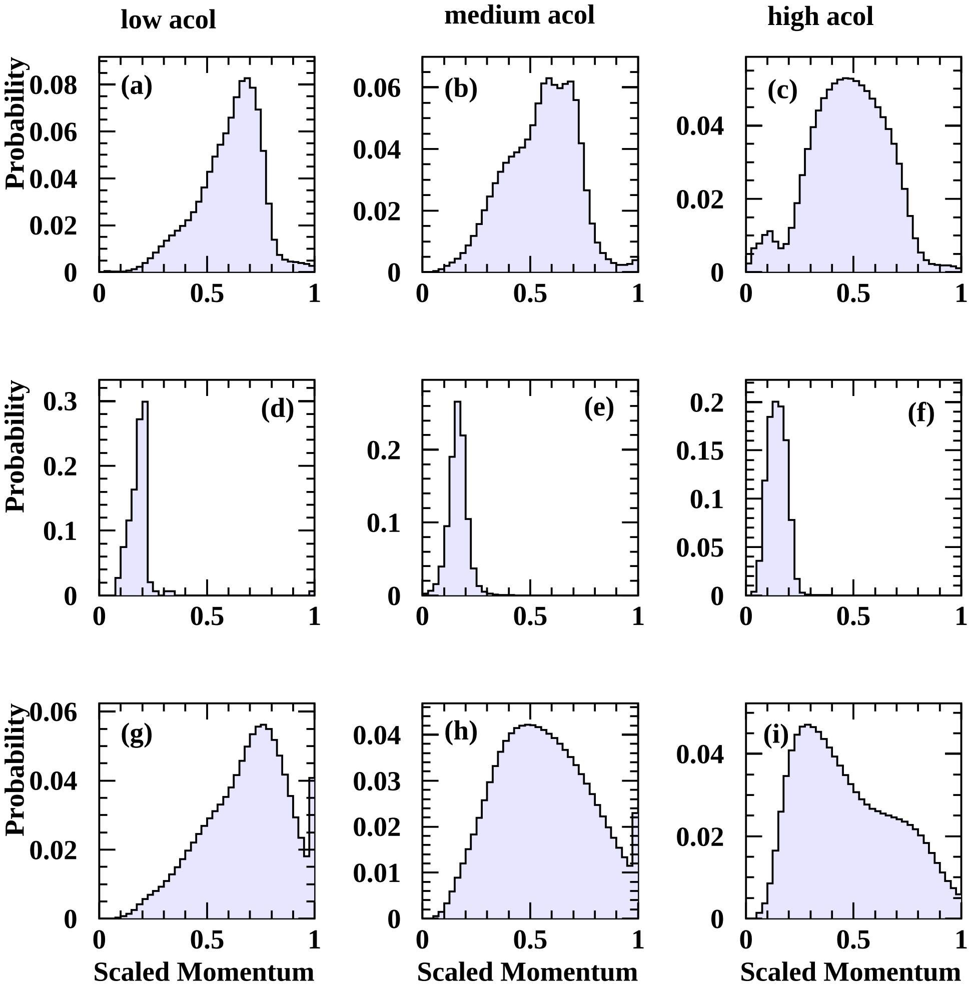

Figure 5.3: Momentum distributions from the selectron search at 189 GeV, for three different acolinearity ranges for (a-c) Standard Model background (d-f) selectron signal with m = 70 GeV and Δm = 10 GeV (g-i) selectron signal with m = 45 GeV and Δm = 45 GeV.

of these decays [6], one finds that in 40 % of the stau events both taus will decay to hadrons. Compare this to $W^+W^- \rightarrow \ell^+\nu\,\ell^-\overline{\nu}$ events where only 4.5 % of events contain two taus which decay to hadrons. Clearly an event with this final state can be weighted as highly signal-like.

Of course perfect lepton identification cannot be achieved in the real world, but many of the benefits described above can still be realised.

Tau Platform Lepton ID

This analysis employs the lepton ID provided by the OPAL Tau Platform (TP). This is a standard piece of OPAL software which was developed to identify the various tau decay modes at LEP1, and has recently been adapted to also identify isolated leptons at LEP2. The TP lepton ID works in several stages:

1. Lepton cones are identified and a high efficiency preselection is applied using polar angle, momentum, and track multiplicity to reduce obvious background (ie. cones which are not leptons).
2. Cones are classified according to general appearance using number of tracks, number of photons, HCAL activity, and muon chamber hits.
3. Class dependent cuts are applied. For some classes this completes the lepton identification. Variables used are E/p, dE/dx, and HCAL activity.
4. For some classes a likelihood is used with variables dE/dx, presampler and ECAL energies, invariant mass, and HCAL activity.

For each cone a lepton ID is assigned which will be either e, μ, or $\tau \rightarrow$ nh (where n $\geq$ 1). No attempt is made to separate prompt electrons or muons from $\tau \rightarrow$ e or $\tau \rightarrow \mu$ decays.

It is possible for a cone to satisfy the requirements for more than one lepton ID or none at all. If such a cone is of a class where a likelihood is used (which is likely for cones where the decision is not clearcut) then the likelihood can be used to decide the lepton ID. In cases where a decision still cannot be made cones are assigned an ambiguous lepton ID, either electron-hadron ambiguous or muon-hadron ambiguous (referred to as (e/h) and (μ/h) from now on). Lepton cones which are electron-muon ambiguous are very rare, so a separate category for these is not required.

Using the TP lepton ID is a new addition to this analysis since the previous published version [19]. The TP software runs independently of the event selection used in this analysis (see section 4.1), and the cones identified by it are then matched to the leptons identified by the event selection. If no matching TP cone is found then the simpler lepton ID provided by the event selection is used. Using the TP lepton ID is found to bring significant gains in efficiency and purity (compare tables 5.1 and 5.2). The lepton ID category "x" in tables 5.1 and 5.2 refers to "rest of event" leptons selected by selection A, which do not match to any TP cone. These tables quote the efficiency for Monte Carlo leptons with $\cos\theta < 0.95$ and $P > 0.02E_{beam}$. About 10% of Monte Carlo leptons fail these criteria and are not used to calculate the performance of the lepton ID.

Selectrons and Smuons

As noted previously, for the selectron search channel one wants to consider only events with two electrons in the final state. To achieve this events are used only if at least one lepton is identified as an electron and no leptons in the event are compatible with being muons (ie. the other lepton is not identified as a muon or as (μ/h) ambiguous). This is because the probability for an electron to be identified as a muon is very small, so rejecting these events results in a negligible loss of efficiency. Events selected by the single lepton selection where the lepton is identified as an electron are also accepted. This selects 99% of the genuine di-electron events.

Lepton ID	True Identity of Lepton			purity
	e or $\tau \to$ e	μ or $\tau \to$ μ	$\tau \to$ h	
	(a)KoralW $\ell\ell\ell\ell$ all leptons			
e	96.3 %	0.1 %	4.8 %	97.7 %
μ	0.1 %	98.2 %	3.6 %	98.2 %
h	1.2 %	0.8 %	86.9 %	95.3 %
(e/h)	2.2 %	0.1 %	2.9 %	–
(μ/h)	0.2 %	0.8 %	1.9 %	–
x	0.0 %	0.0 %	0.4 %	–
	(b) Lepton Energy $>$ 10 GeV			
e	96.4 %	0.0 %	3.2 %	–
μ	0.1 %	99.0 %	3.0 %	–
h	1.2 %	0.3 %	89.1 %	–
(e/h)	2.1 %	0.0 %	2.7 %	–
(μ/h)	0.2 %	0.7 %	1.9 %	–
x	0.0 %	0.0 %	0.2 %	–
	(c) Lepton Energy $<$ 10 GeV			
e	96.0 %	0.0 %	3.4 %	–
μ	0.2 %	96.9 %	3.3 %	–
h	1.0 %	2.3 %	80.9 %	–
(e/h)	2.3 %	0.0 %	3.7 %	–
(μ/h)	0.1 %	0.6 %	7.2 %	–
x	0.3 %	0.1 %	1.6 %	–

Table 5.1: Lepton ID performance using TP lepton ID, calculated using (a) KoralW $\ell\ell\ell\ell$ Monte Carlo at $\sqrt{s}$ =189-206 GeV (b) Leptons with energy greater than 10 GeV (from a mixture of signal and background sources) (c) Leptons with energy less than 10 GeV (from a mixture of signal and background sources).

Lepton ID	True Identity of Lepton			purity
	e or $\tau \to$ e	μ or $\tau \to \mu$	$\tau \to$ h	
e	92.4 %	0.0 %	12.2 %	94.2 %
μ	0.3 %	97.8 %	6.2 %	96.6 %
h	6.5 %	1.4 %	79.5 %	82.5 %
x	0.9 %	0.7 %	2.0 %	–

Table 5.2: Lepton ID performance without using TP lepton ID, calculated using KoralW $\ell\ell\ell\ell$ Monte Carlo at $\sqrt{s}$ =189-206 GeV.

The smuon search channel is treated similarly to selectrons, with only events containing one muon and no leptons identified as e or (e/h) being considered. Figure 5.4 shows the distribution of di-lepton ID for data, background and selectron and smuon signal events. Note that only channels 1,7,8,16 and 21 are considered as selectron candidates, and only channels 2,10,12,17 and 22 are considered as smuon candidates.

Additional constraints on lepton type for selectron and smuon searches

Some additional constraints are applied to the second lepton candidate in the selectron and smuon searches if it is identified as a tau or if it is a "rest of event" candidate from selection A. These extra cuts are designed to reject the event from the selectron (smuon) search if the second lepton candidate is incompatible with being an electron (muon). This should reject obvious background events with a negligible loss in signal efficiency.

Events containing tau candidates are rejected from the selectron search if the tau candidate has a high charged track multiplicity or one of its tracks satisfies a tight muon identification.

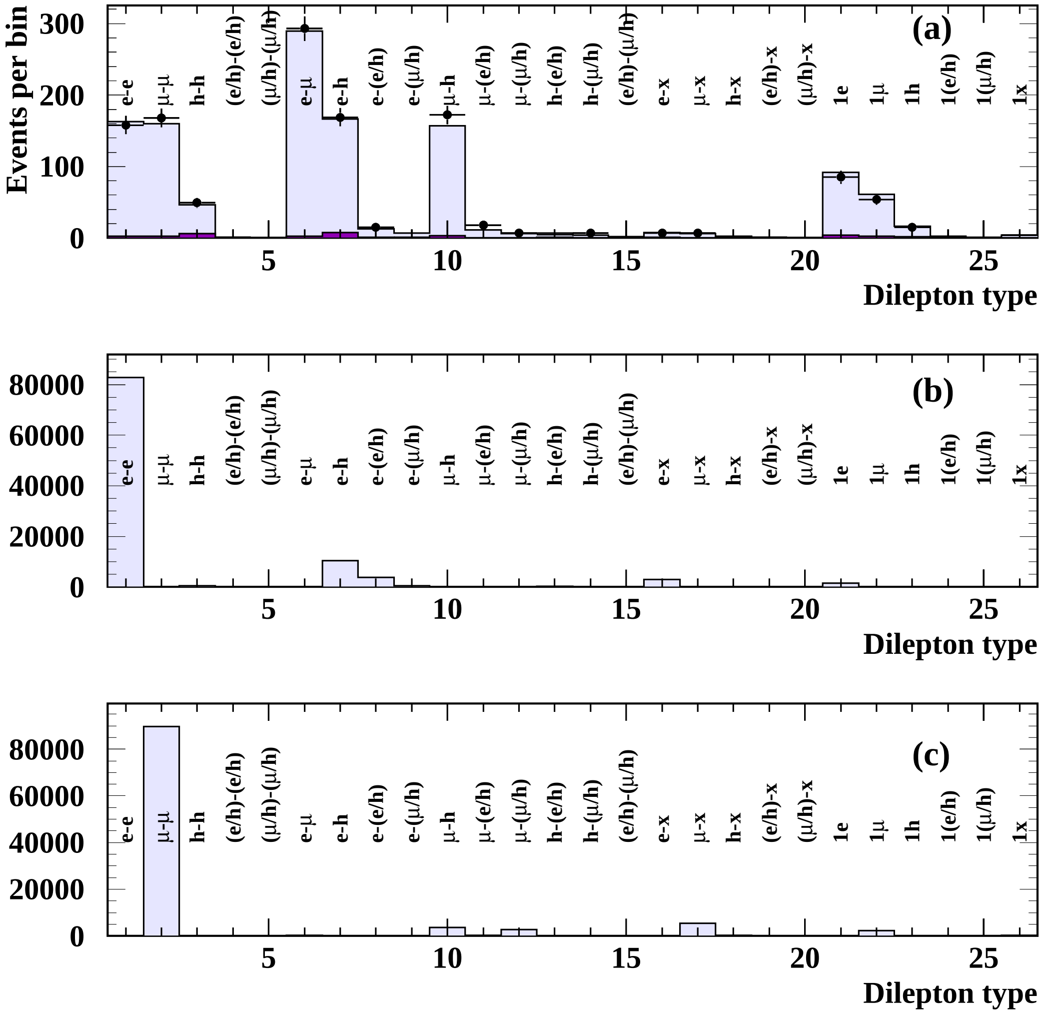

Figure 5.4: Di-lepton ID for (a) data at $\sqrt{s} = 189 - 208$ GeV and Standard Model background (b) selectrons (c) smuons.

Events containing "rest of event" lepton candidates are rejected from the selectron search if they have high invariant mass, many charged tracks, or E/p of the highest momentum track not compatible with being an electron.

Events containing tau or "rest of event" lepton candidates are rejected from the smuon search if the second lepton has high invariant mass which is not compatible with being a muon.

These additional requirements reject 21.1% of the background from the selectron search, with only 2.1% reduction in signal efficiency. The background for the smuon search is reduced by 14.1%, with only 0.8% reduction in signal efficiency.

Staus, Charginos and Charged Higgs

All events from the general selection are considered in the remaining search channels (stau, chargino and charged higgs). However, as can be seen from figure 5.4, this leads to a large number of different dilepton ID categories. Spreading the limited number of signal Monte Carlo events over such a large number of bins can lead to large statistical fluctuations which will degrade the sensitivity of the likelihood - particularly where the signal efficiency is low. For likelihood variables which have a continuous distribution, such as momentum or acolinearity, this problem is reduced by the use of histogram smoothing (see section 5.4). In the case of the lepton ID variable the distribution is not continuous between bins — so smoothing is not appropriate.

Instead the number of lepton ID categories is reduced by removing the distinction between electrons and muons - and merging them into 1 category referred to as ℓ . This is acceptable because the ability to discriminate between an electron or a muon and a hadronically decaying tau is much more important than the discrimination between electrons and muons, when searching for staus or charged Higgs. Chargino events have a lepton ID distribution which is similar to that of W^+W^- events so

	Average L_R		
Lepton ID used	Background	Signal	Difference
1. From Selection	0.3681	0.6319	0.2638
2. Full TP	0.3415	0.6585	0.3170
3. TP with e/$\mu = \ell$	0.3420	0.6580	0.3160

Table 5.3: Results of testing sensitivity of three different lepton ID schemes, for separating stau signal from Standard Model background.

here the lepton ID variable is less important in any case.

Removing the distinction between electrons and muons reduces the 25 dilepton ID categories shown in figure 5.4 to just 13. The distribution of events between these categories is shown in figure 5.5 for data, background and stau events.

In order to show that no significant loss of sensitivity is incurred by reducing the number of dilepton ID categories, a simplified version of the likelihood ratio was formed using only the lepton ID variable. The average separation between stau signal and background was tested for 3 different lepton ID schemes:

1. The lepton ID taken from the event selection (this is the lepton ID which was used in the previous published version of this analysis).
2. The TP lepton ID, using the full 26 dilepton categories.
3. The TP lepton ID, with no distinction between e and μ .

The results of this test are shown in table 5.3. A significant increase in the separation of signal and background is achieved by using the TP lepton ID, and 98 % of this gain is kept after removing distinction between e and μ .

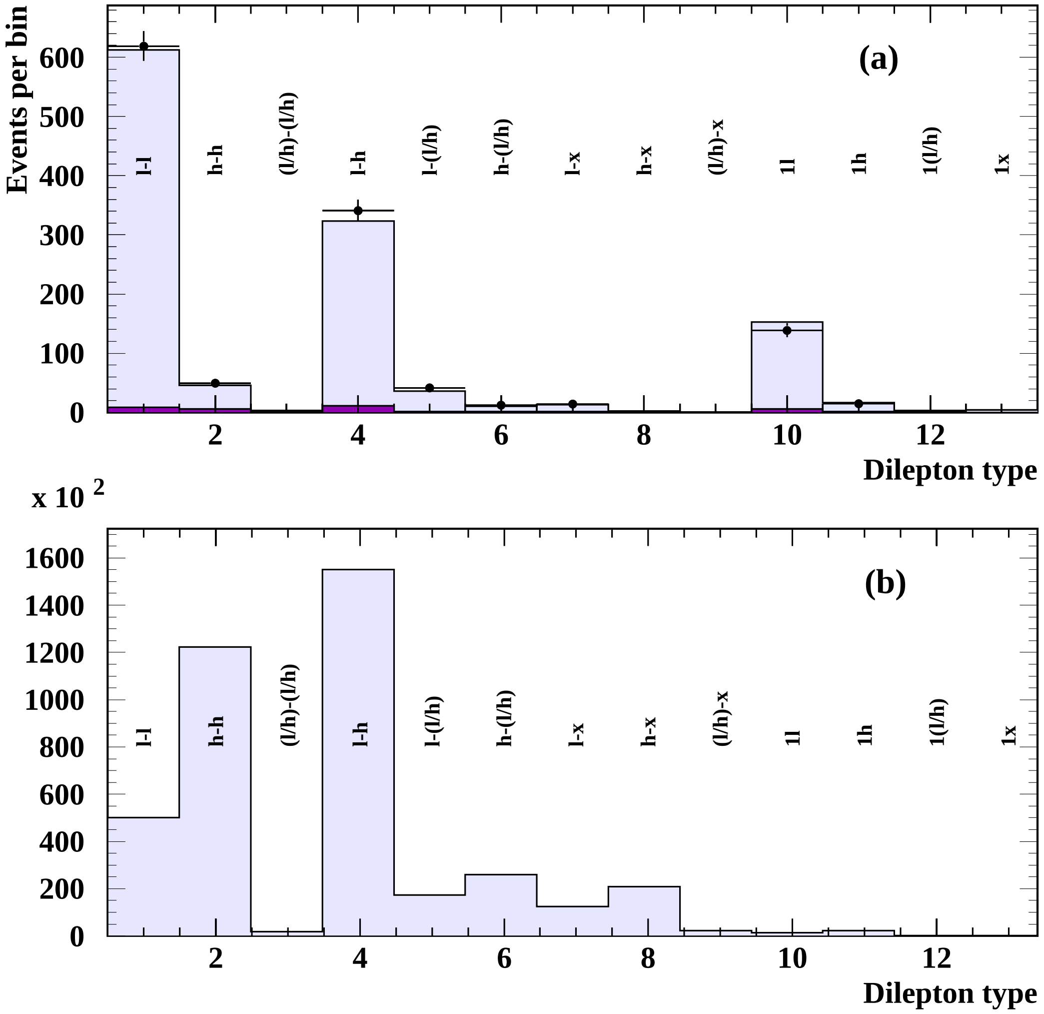

Figure 5.5: Di-lepton ID with e/μ = ℓ for (a) data at $\sqrt{s} = 189 - 208$ GeV and background (b) stau signal.

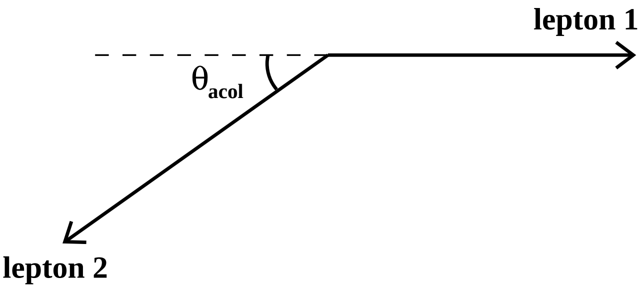

Figure 5.6: Definition of acolinearity as $180° - \theta$, where θ is the angle between the two leptons. The figure shows the plane containing the two leptons.

5.2.3 Acolinearity and Momentum Asymmetry

These two variables are considered together because of their strong correlation.

Acolinearity

The acolinearity of an event is defined as the complement of the angle between the two leptons (see figure 5.6). Thus events with low acolinearity are almost back-to-back, and those with high acolinearity have only a small angle between the two leptons.

The background acolinearity distribution is peaked towards low values. This is because the lepton decay angle is forward peaked in the W rest frame due to the spin structure of W decay (see figure 5.7 a).

The signal acolinearity distributions vary with m and Δm. At low parent particle mass, a large boost is given to the decay particles along the direction of the parent. This results in smaller values of acolinearity. At higher values of m, where the parents are produced almost at rest, the daughter lepton can decay in any direction. This results in a peak at $\pi/2$. When Δm is low the visible energy in the event is also low. This leads to low efficiency to select events because they do not pass the

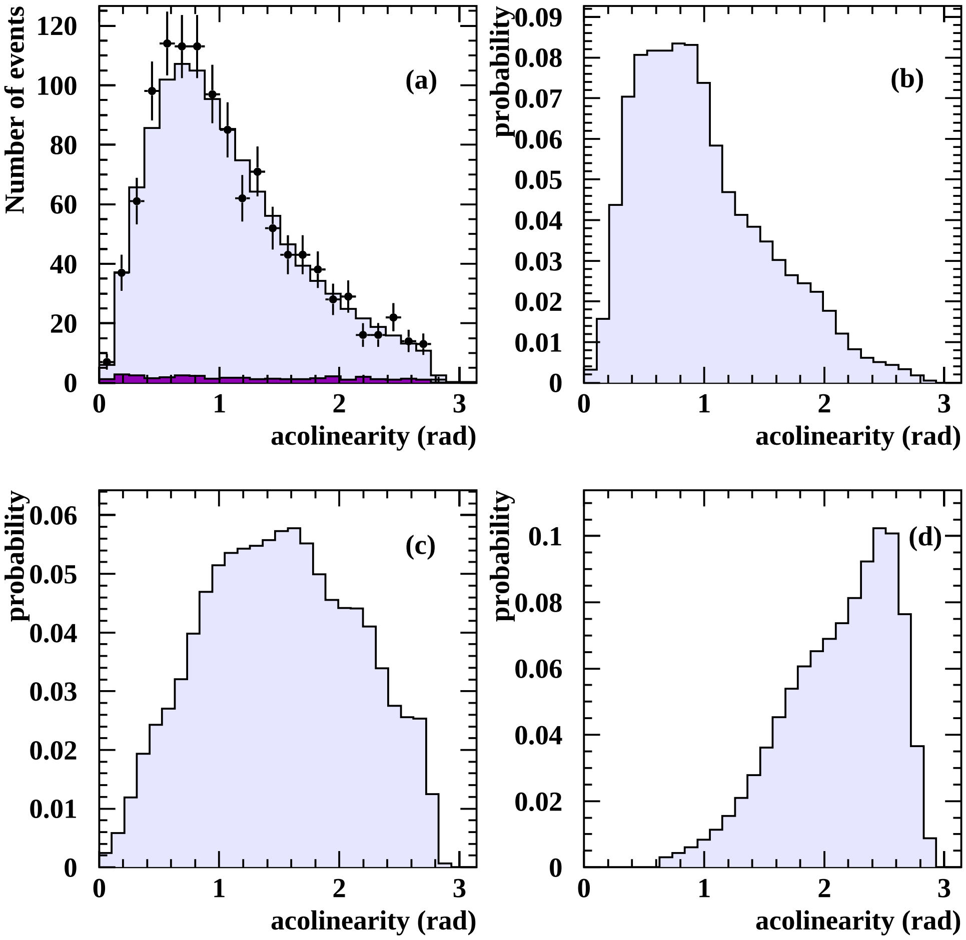

Figure 5.7: Acolinearity distributions for (a) data at $\sqrt{s} = 189 - 208$ GeV and background (b) selectrons at $\sqrt{s} = 200$ GeV with m = 45 GeV and $\Delta m = 45$ GeV (c) selectrons at $\sqrt{s} = 200$ GeV with m = 99 GeV and $\Delta m = 99$ GeV (d) selectrons at $\sqrt{s} = 200$ GeV with m = 99 GeV and $\Delta m = 2.5$ GeV.

missing transverse energy cut. High acolinearity maximises the amount of missing transverse energy in an event, making the event more likely to be selected. This results in a bias towards high acolinearity at low Δm. Various signal acolinearity distributions are shown in figure 5.7 b-d.

Events selected with the single-lepton topology (see section 4.1.1) present a problem in defining an acolinearity. These events contain only one lepton candidate and no other charged tracks. They may however contain other activity, such as ECAL or forward detector clusters. If these are present then they are assumed to be evidence for the second lepton, and are considered as such for the purpose of calculating the acolinearity. If there are no other clusters in the event then an acolinearity cannot be defined and the event is not considered as a candidate. This requirement is also useful because it reduces the number of events from background processes, such as $\mathrm{e^+e^-} \rightarrow \mathrm{We}\nu$ (see figure 4.2c), which tend to produce only one observed lepton, with only a small loss in efficiency for signal-like processes with two charged leptons. The total Standard Model background is reduced by 6.5%, while the number of signal events selected is reduced by only 0.3%.

Momentum Asymmetry

A variable called the momentum asymmetry, which describes the correlation between the two lepton momenta, is defined as follows:

$$A_x = \frac{x_{max} - x_{min}}{x_{max} + x_{min}}, \tag{5.5}$$

where x_{max} is the scaled momentum of the more energetic lepton in the event, and x_{min} is the scaled momentum of the less energetic lepton. The momentum asymmetry variable is complementary to the two momentum variables because it describes the correlation between them, but not their absolute values. This is particularly useful at low signal mass values where the momentum distributions are broad. It adds less information at high signal mass values where the momentum distributions are narrow, leading to low values of A_x.

This variable is correlated with the acolinearity of the event. The information contained in this correlation would be lost by using one-dimensional (1D) histograms, so a 2D histogram of A_x against acolinearity is used. Examples of this 2D distribution are shown in figure 5.8 for various signals and background.

Using a 2D distribution increases the problems of limited Monte Carlo statistics. Histogram smoothing becomes very important. The technique used for smoothing 2D histograms causes a smearing of the distribution, and this means that sensitivity to sharp features is compromised. It is necessary to establish that the gain in sensitivity from using the extra kinematic correlations is not cancelled out by this loss due to smoothing.

This was investigated by comparing the expected sensitivity (see section 5.8.1 for details of how this is evaluated) using the 2D histogram and using a simple 1D acolinearity histogram[2].

It was found that the use of a 2D histogram is only advantageous in the selectron and smuon search channels. The other channels (stau, chargino, charged Higgs) all involve additional neutrinos from tau decays in the final state. These dilute the quality of kinematic information gained by using the 2D histogram. When combined with the smearing caused by the histogram smoothing process, there was no net gain in sensitivity for these channels.

For search channels other than selectron and smuon a simple 1D acolinearity histogram is used.

---

[2] This was the case in the previous version of the analysis.

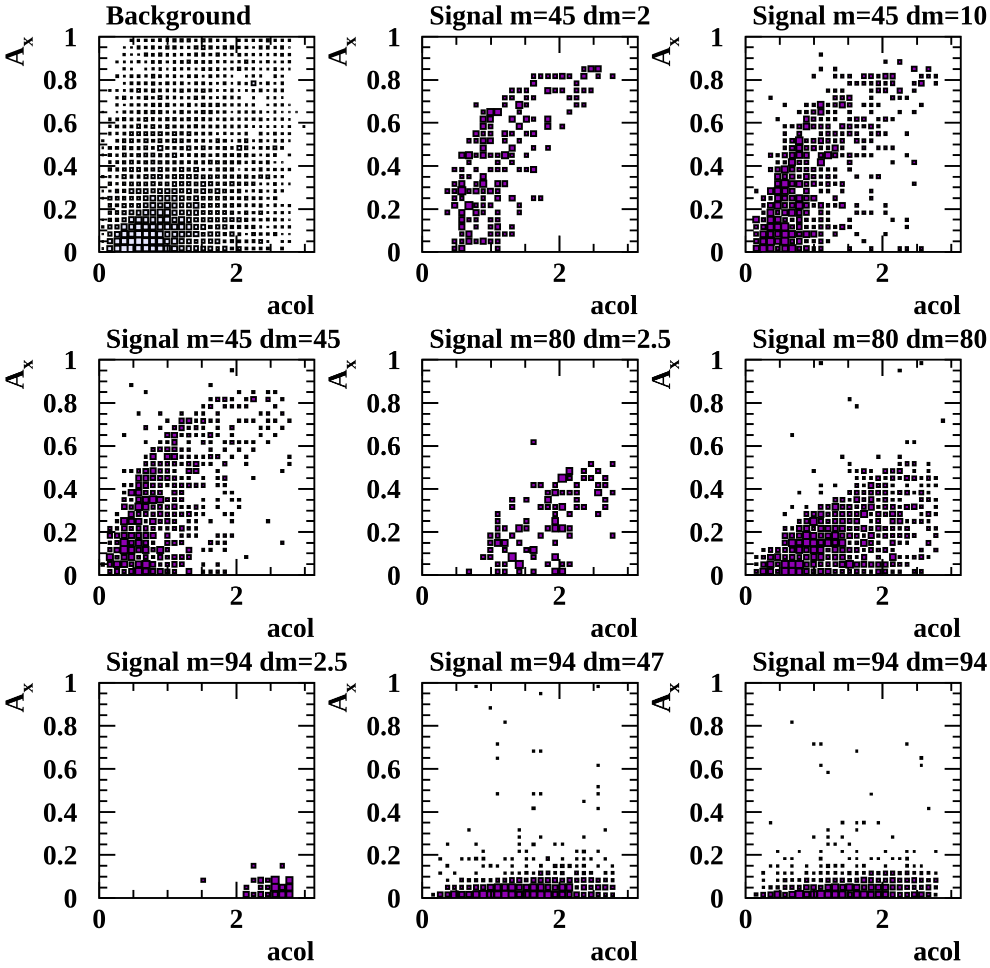

Figure 5.8: Two dimensional distributions of momentum asymmetry against acolinearity for Standard Model background (with lepton ID cuts for selectron search applied) and various signals in the selectron search at 189 GeV.

5.2.4 Charge-signed Polar Angle

The charge-signed cosine of the polar angle is defined for each lepton as $-q\ \cos\theta$, where q is the charge of the lepton (1 or -1) and θ is its polar angle.

This variable is strongly forward peaked in the background (ie. negative leptons tend to travel close to the the electron beam direction and positive leptons tend to travel close to the positron beam direction). This is caused by a combination of the dominance of the t-channel neutrino exchange mechanism for W^+W^- production which produces the W particles preferentially in the forward direction, and the forward peaking of the lepton decay angle described in section 5.2.3.

For the smuon, stau and charged higgs channels the distribution of $-q\cos\theta$ is not forward peaked. This is because these particles are produced in the s-channel with no preferred direction, and the lepton decay is not forward peaked in the slepton (or higgs) rest frame. This results in a fairly flat distribution which is symmetric about $\cos\theta = 0$. Example distributions of $-q\cos\theta$ for background and signal are shown in figure 5.9. The signal distributions show only a slight variation with m and Δm.

This variable is not used in the selectron and chargino search channels because these particles can also be produced via t-channel neutralino or sneutrino exchange respectively. The relative importance of the s- and t-channel production mechanisms depends on the SUSY parameters, resulting in a $-q\cos\theta$ distribution which is model dependent.

5.3 Note on Signals Considered

It should be noted that an essentially independent analysis is carried out for each value of m and Δm considered. This means that signal reference histograms for each variable, and L_R distributions for signal and background are created for every

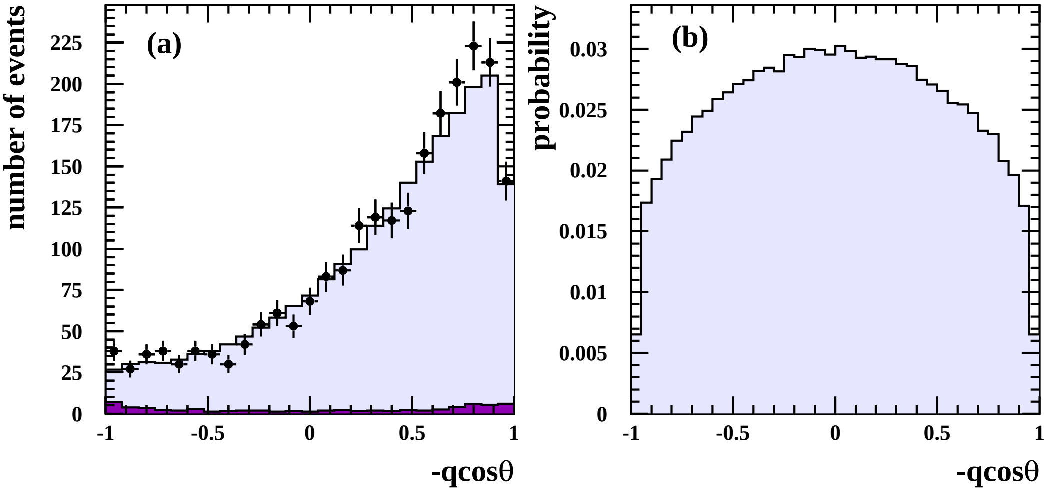

Figure 5.9: Distributions of $-q\cos\theta$ for (a) data at $\sqrt{s} = 189 - 208$ GeV and Standard Model background and (b) stau signal at $\sqrt{s} = 200$ GeV.

m and Δm value.

Since the search is carried out on a 1 GeV by 1 GeV grid in m and Δm it would be impractical to produce signal Monte Carlo for every one of these fine grid points. Instead a coarse grid (see figure 5.10) is used for the production of signal Monte Carlo, and interpolation techniques have been developed to reconstruct the histograms at intermediate grid points.

Even using a coarse grid for signal Monte Carlo production results in around 100 different combinations of m and Δm for each search channel and for each $\sqrt{s}$ value considered. This places a logistical restriction on the number of events which can be generated at each point. As a result statistical fluctuations are still a significant problem. Histogram smoothing is used to reduce this effect. The histogram smoothing and interpolation techniques used are discussed in the following sections (5.4 to 5.6).

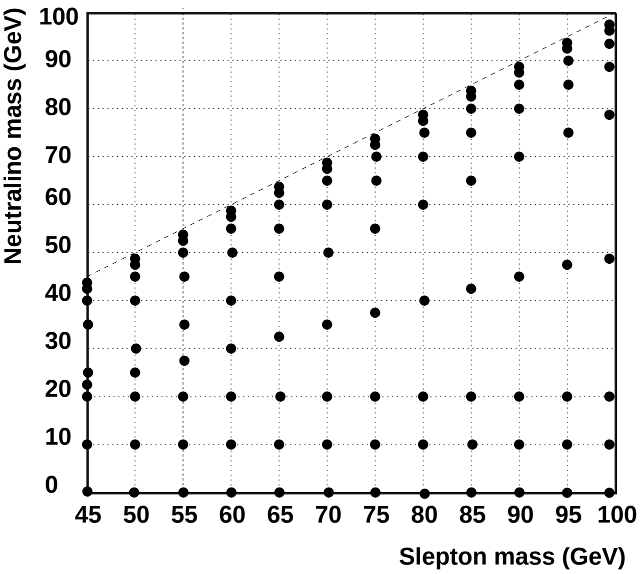

Figure 5.10: Grid of m and Δm values where signal Monte Carlo is produced.

5.4 Smoothing of Reference Histograms

Reference histograms are smoothed to reduce the effect of statistical fluctuations. In order for the smoothing techniques to work, the size of any genuine features of the distribution (eg. peaks, endpoints) must be larger than the statistical fluctuations. This requires that the reference histograms and binning used are carefully chosen so as not to stretch the available Monte Carlo statistics too far.

5.4.1 One Dimensional Histograms

A smoothing algorithm [34] is applied to the 1D reference histograms for scaled momentum, $-q\cos\theta$ (and acolinearity for the search channels where 2D histograms are not used). The sensitivity of the smoothing to statistical fluctuations can be adjusted. For signal histograms, this parameter is chosen to be the maximum value for which there is only one peak in the smoothed histogram. For background histograms two peaks are allowed.

The most severe problems with low statistics occur at low Δm where the signal selection efficiency can be very low. It is fortunate that this is the kinematic region where the momentum distributions are narrowest, so the events are only spread over a small number of bins. Figure 5.11 shows some examples of the effect of 1D smoothing. Leptons which are measured to have momentum greater than the beam energy are not entered into the momentum reference histogram before smoothing. They are added to the last bin of the histogram after smoothing. This can be seen in figure 5.11(e,f).

5.4.2 Two Dimensional Histograms

Smoothing of 2D momentum asymmetry versus acolinearity histograms is carried out by a process of averaging entries over several bins. The procedure is described in the steps below:

1. Define region around a certain bin (initial size 3×3 bins), and find sum of all bin contents within the region.
2. If the sum is greater than a certain number (n_{min}) then replace the original bin entry, n_{orig}, with a new value n_{smooth}, where $n_{smooth} = n_{orig}/2 + n_{av}/2$, and n_{av} is the average content of the bins within the surrounding region [3]. n_{min} is initially set to 9 times the current bin value (but is reduced if there are not enough entries in the histogram to satisfy this requirement).
3. If the sum is less than n_{min} then increase the size of the region and find the sum again.

---

[3] This formula for n_{smooth} was chosen in preference to $n_{smooth} = n_{av}$ to reduce the amount by which bin contents are changed by the smoothing. This was found to be useful in areas where the original histogram has a large gradient.

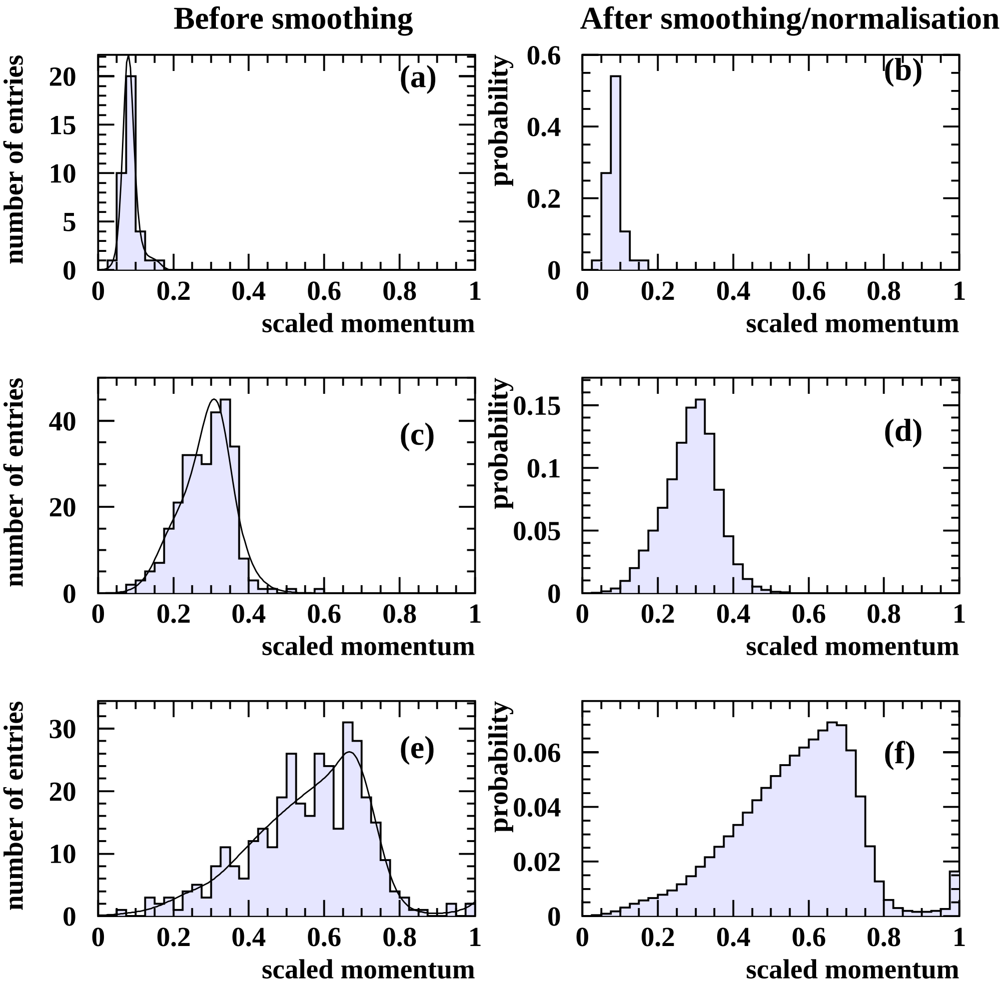

Figure 5.11: Examples of effect of 1D smoothing. The first column shows the unsmoothed histogram with the function produced by the smoothing algorithm superimposed. The second column shows the resulting smoothed and normalised histograms. These are all scaled momentum histograms for selectrons with m = 45 GeV and (a,b) Δm =2.5 GeV, (c,d) Δm = 10 GeV, (e,f) Δm = 25 GeV.

4. Repeat this process for all bins in the histogram.
5. Find the number of peaks in the histogram (a peak is defined as a bin whose contents are larger than all 8 neighbouring bins). If this is greater than 3 then smooth the histogram again.

This method of smoothing potentially suffers from smearing of sharp features in the histogram to a greater degree than the 1D method, which tries to fit a curve to the data. Knowledge of what the distribution is expected to look like can be used to identify sharp edges in the histogram. These are then preserved by splitting the histogram into two regions on either side of the edge, and not allowing events to be smeared from one region to another.

Figure 5.8 shows some of the 2D histograms before smoothing. A clear curved edge can be seen in the momentum asymmetry versus acolinearity plane. A curve defined by $F(x) = V\sqrt{\sin((x-s)/2)}$ is used to locate the edge. The parameters V and s are varied to maximize the difference between the contents of bins adjacent to this curve on either side of it. The position of the edge is seen to depend most strongly on m, so all of the histograms with the same value of m are added together for the purpose of locating the edge. Figure 5.12 shows some examples of 2D histograms before and after smoothing.

5.5 Interpolation of Reference Histograms

5.5.1 One Dimensional Histograms

The method used to interpolate 1D reference histograms is based on that developed by David Futyan and described in his thesis [35], and below.

To construct histogram H at mass m by interpolating between two histograms H_1

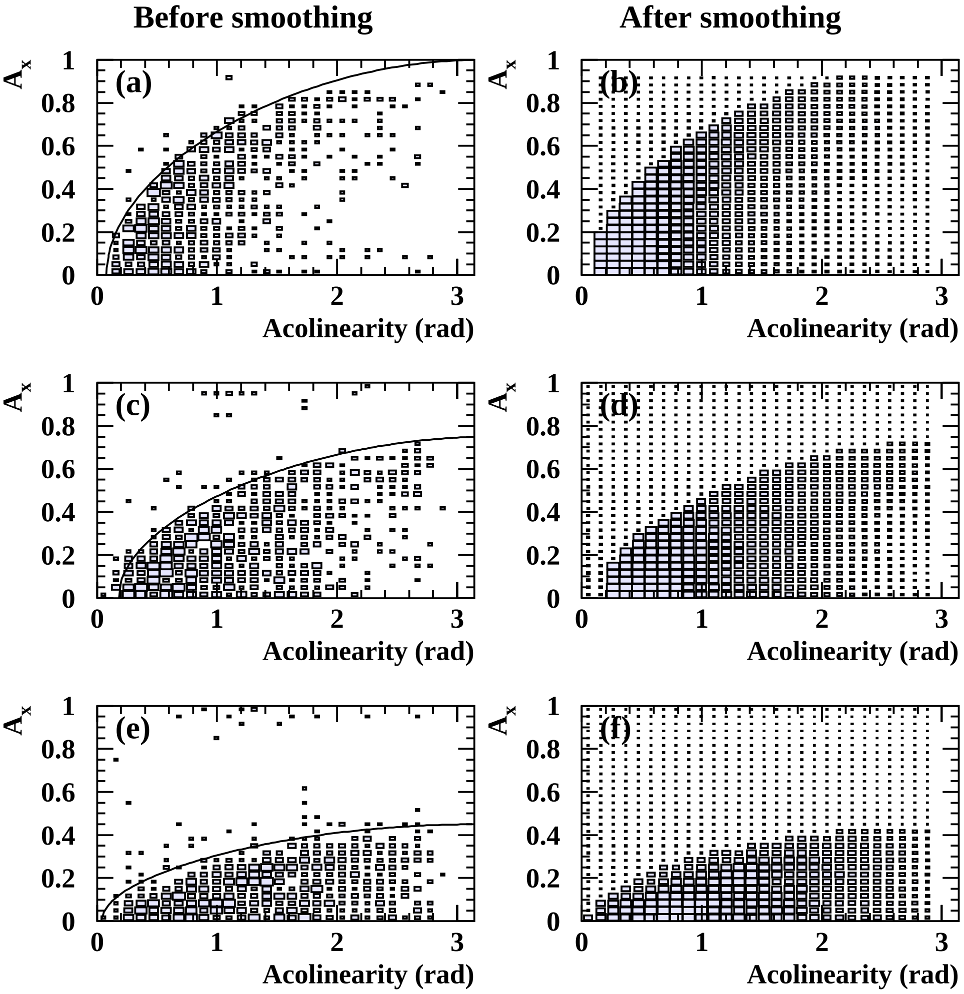

Figure 5.12: Examples of effect of 2D smoothing. The first column shows the unsmoothed histogram, along with the line which divides the histogram into two regions. The second column shows the resulting smoothed histograms. These examples are for smuon signal at $\sqrt{s} = 200$ GeV with (a,b) $m = 45$ GeV and $\Delta m = 10$ GeV, (c,d) $m = 70$ GeV and $\Delta m = 35$ GeV, (e,f) $m = 90$ GeV and $\Delta m = 90$ GeV.

and H_2 at masses m_1 and m_2 the following steps are performed.

1. Calculate
$$q = q_1 + (q_2 - q_1)\frac{m}{m_2 - m_1}, \tag{5.6}$$
where q_1 and q_2 are the contents of the first non-zero bin of histograms H_1 and H_2 respectively.

2. Subtract q from both H_1 and H_2, from the left, as represented by the shaded areas in figure 5.13.

3. Calculate
$$x = x_1 + (x_2 - x_1)\frac{m}{m_2 - m_1}, \tag{5.7}$$
where x_1 and x_2 are the mean positions of the events removed in step 2 from H_1 and H_2 respectively.

4. Calculate
$$n_1 = \sum_{k=k_1}^{k_2} \frac{H_1(k)}{H_1(k_{max})}, \tag{5.8}$$
where k_1 and k_2 are the first and last bins respectively of histogram H_1 which are subtracted from in step 2, k_{max} is the bin of histogram H_1 from which the maximum amount is subtracted, and $H_1(k)$ is the value of bin k in histogram H_1. Also calculate a similar quantity n_2 for histogram H_2. These are measures of the spread in bins from which the amount q is subtracted from each histogram. The value is weighted by the amount subtracted from each bin. For example, if the whole amount q is subtracted from one bin then the spread in bins is $n_1 = 1$. If q is subtracted from two bins, with the same amount being taken from each bin then the spread in bins is $n_1 = 2$. If q is subtracted from two bins with twice as much taken from one bin as the other, then the spread in bins is $n_1 = 1.5$.

5. Now calculate
$$n = n_1 + (n_2 - n_1)\frac{m}{m_2 - m_1}. \tag{5.9}$$

This is the interpolated spread in bins, and is used to determine how many bins the amount q should contribute to in the interpolated histogram.

6. Add amount q to histogram H with width n bins and centred around position x.

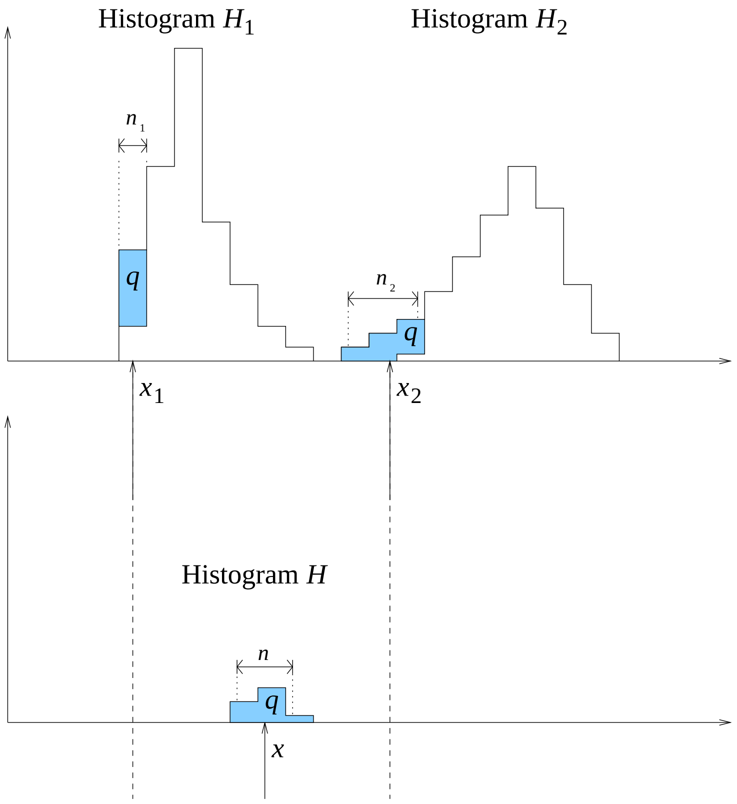

Figure 5.13: Interpolation of 1D histograms (adapted from [35]).

Steps 1 to 6 are repeated until histograms H_1 and H_2 are empty.

The difference between this method and that used in [35] is in steps 4 and 5. Previously the width from which the amount q was subtracted from each histogram was not considered, and it was always added to the interpolated histogram with a width of 1 bin (although this was not necessarily centered on one bin in the new histogram, so usually contributed over two bins). The effect of this modification is typically small, but can be significant in situations where the shape of the histogram is changing rapidly. If H_1 is much more sharply peaked than H_2 then spikes can occur in the interpolated histogram if the additional spreading is not used. Figure 5.14 shows an example of this.

5.5.2 Two Dimensional Histograms

Interpolation of 2D histograms is achieved by splitting the 2D histogram into a number of 1D histograms (one from each column and one from each row of the original). These are then interpolated using the 1D interpolation method described in 5.5.1. These are then recombined into two 2D interpolated histograms - one from interpolating the rows, and one from interpolating the columns. The final interpolated 2D histogram is formed by averaging these two.

5.5.3 Interpolation in m and Δm

To create the reference histogram for an arbitrary point in the m—Δm plane, one needs to interpolate in two directions. This is achieved by using the reference histograms from the 4 nearest Monte Carlo grid points and a combination of 3 interpolations (two in m and one in Δm — see figure 5.15).

5.5.4 Interpolation in E_{CM}

Signal Monte Carlo events are only generated at $\sqrt{s} = 183{,}189$, 200,204 and 208 GeV for sleptons (see table 4.1 for details). Signal reference histograms must also be created at the other centre-of-mass energies.

To construct a reference histogram at centre-of-mass energy E_{CM} for the point (m,Δm):

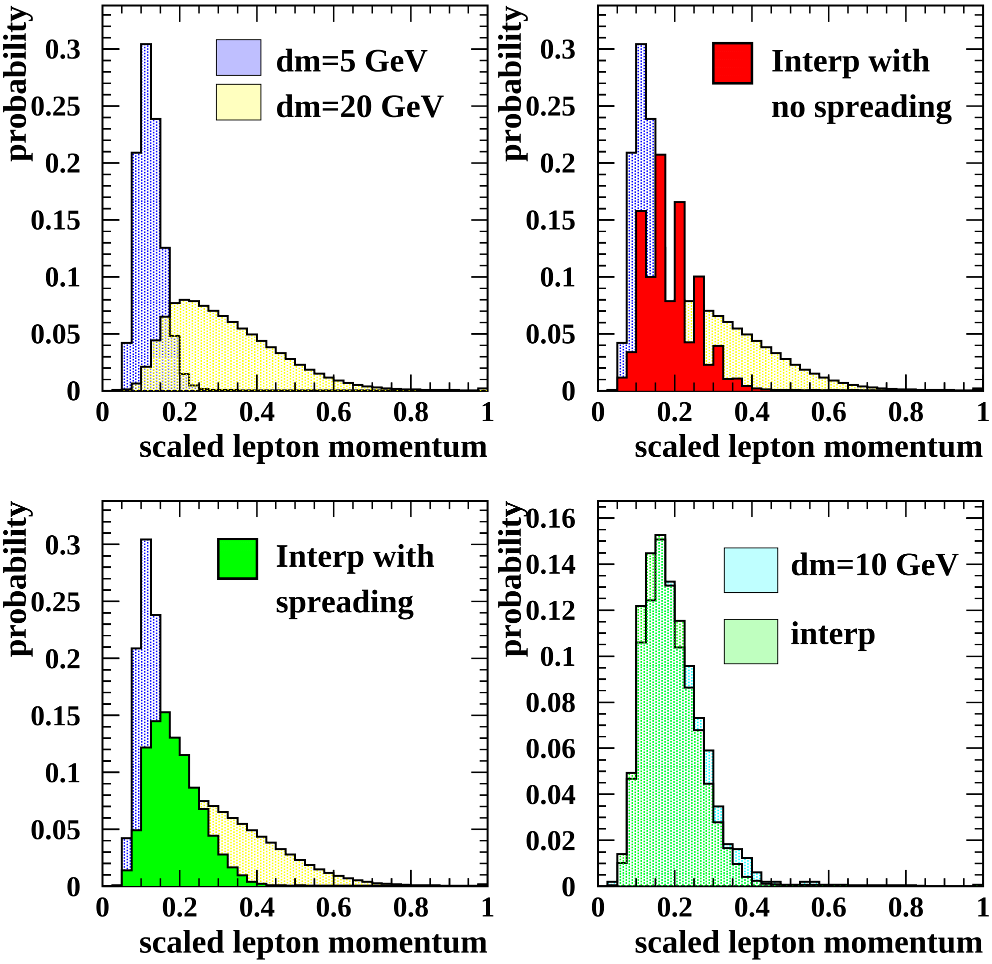

Figure 5.14: Effect of additional spreading in 1D histogram interpolation. Example histograms from stau search at 189 GeV, with $m = 45$ GeV. The bottom right plot compares the interpolated $\Delta m = 10$ GeV histogram with the “true” histogram made using signal Monte Carlo with $\Delta m = 10$ GeV.

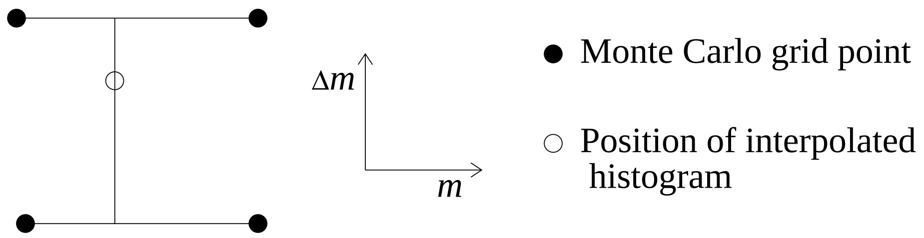

Figure 5.15: Interpolation to an arbitrary point in m and Δm (from [35]).

1. Redefine $(m,\Delta m)$ to a new point $(m',\Delta m')$ at energy E'_{CM}, where

   $$m' = m\,\frac{E'_{CM}}{E_{CM}} \tag{5.10}$$

   $$\Delta m' = \Delta m\,\frac{m'}{m}, \tag{5.11}$$

   and E'_{CM} is the nearest energy below E_{CM} where signal Monte Carlo is available. The aim of this redefinition is that the kinematic distributions for the point $(m', \Delta m')$ at E'_{CM} should be the same as those expected for $(m,\Delta m)$ at E_{CM}.

2. Construct the reference histogram for point $(m', \Delta m')$ using signal Monte Carlo generated at E'_{CM}.

3. Repeat steps 1 and 2 using the nearest energy above E_{CM} where signal Monte Carlo is available.

4. Interpolate between the two reference histograms created in the previous steps to get the final histogram.

This reconstruction process is illustrated in figure 5.16. The process is tested by generating a full set of smuon signal Monte Carlo at $\sqrt{s} = 196$ GeV. Reference histograms for 196 GeV created by interpolating between 189 and 200 GeV are compared to the same histograms made using 196 GeV Monte Carlo (see examples in figure 5.17).

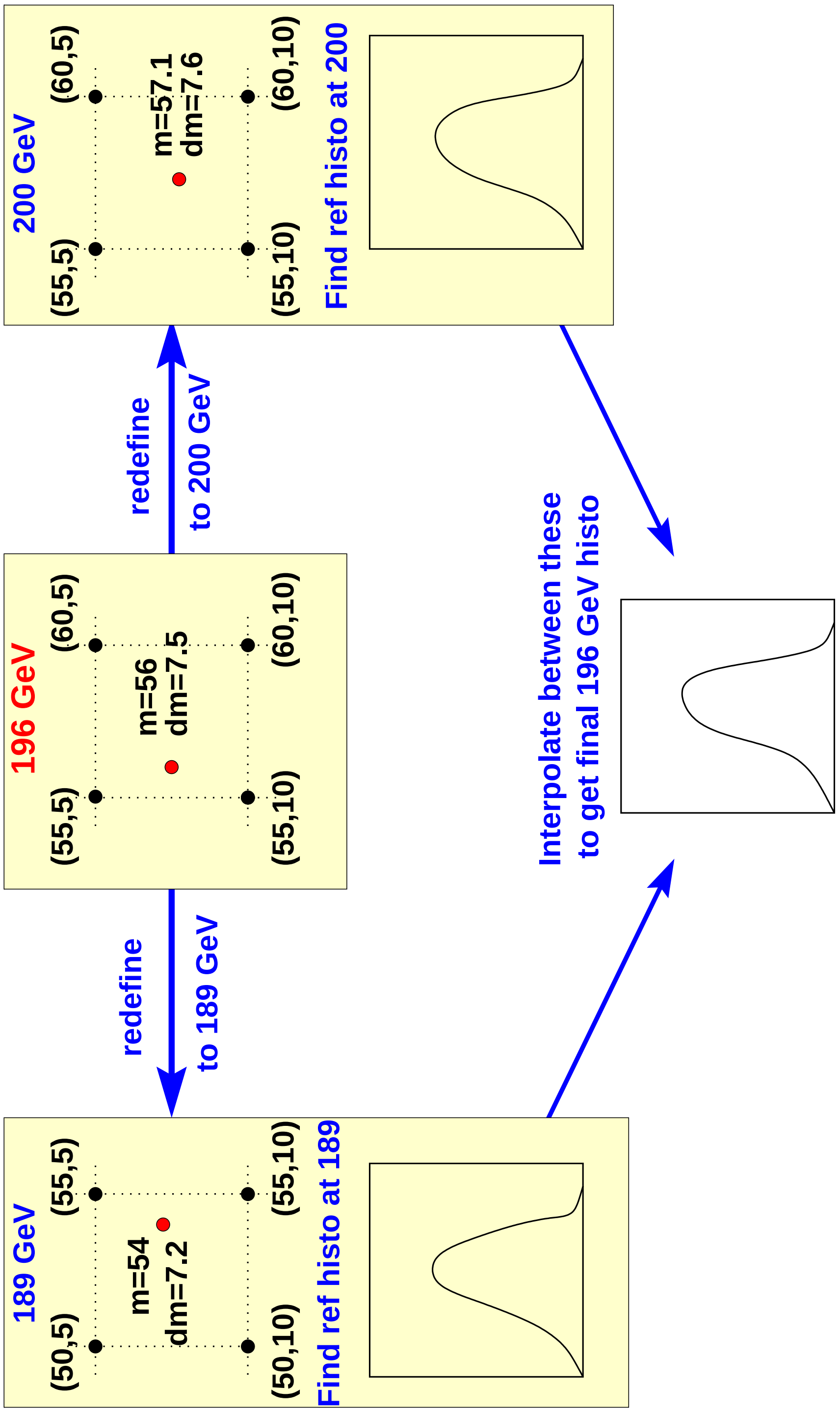

Figure 5.16: Schematic view of process by which reference histograms are interpolated between E_{CM}'s.

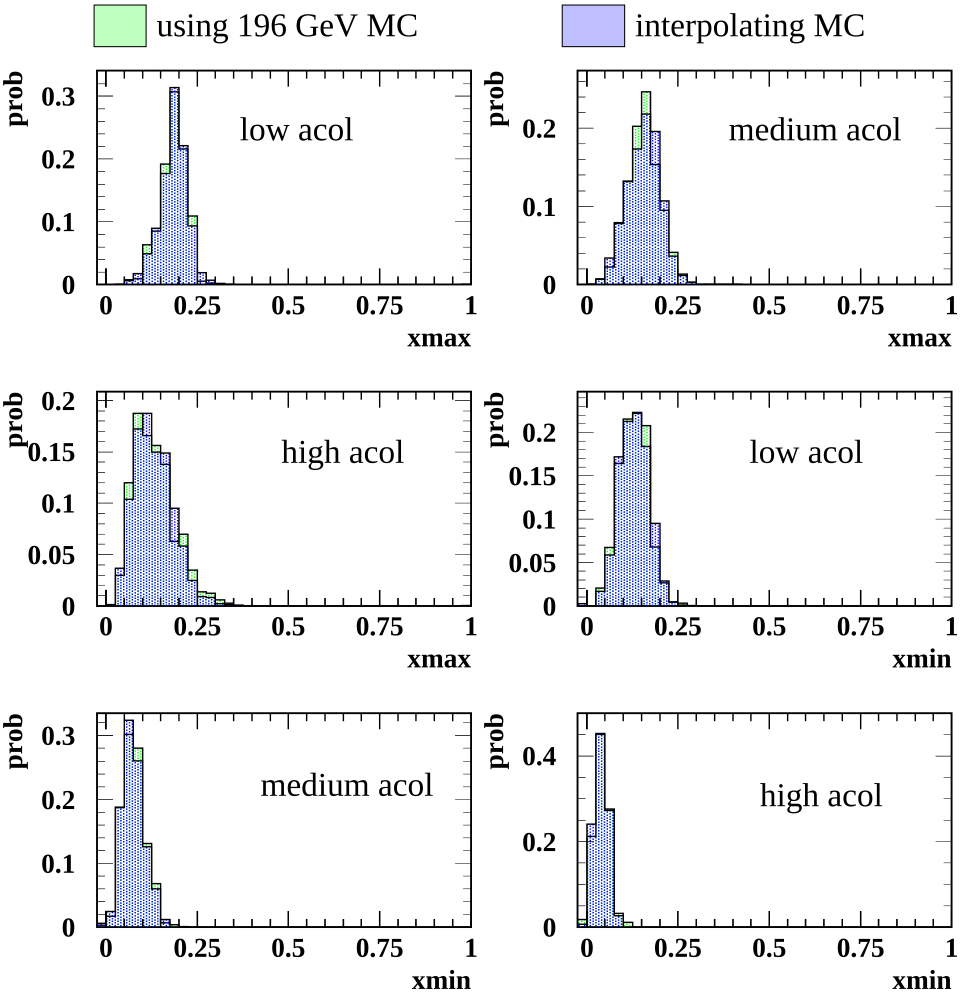

Figure 5.17: Examples of interpolation of signal reference histograms between E_{CM}'s: Momentum reference histograms for the three acolinearity ranges for s-muons at $\sqrt{s} = 196$ GeV with $m = 57$ GeV and $\Delta m = 7.5$ GeV, constructed using signal Monte Carlo generated at $\sqrt{s} = 196$ GeV (light histogram) and interpolating between signal Monte Carlo generated at 189 and 200 GeV (dark histogram).

Note that interpolation of reference histograms between centre-of-mass energies is only necessary for signal. Background histograms are constructed using Monte Carlo generated at the appropriate beam energy for all E_{CM}'s.

5.6 Interpolation of Signal MC

Signal L_R distributions at each Monte Carlo grid point are produced by plotting the L_R value for each signal Monte Carlo event. For intermediate points in m,Δm and $\sqrt{s}$ the L_R distribution is made using signal events from the four nearest grid points (8 at intermediate $\sqrt{s}$), with weights inversely proportional to their distance from the intermediate grid point.

The L_R distribution of signal Monte Carlo at the intermediate point (m,Δm) is simulated using signal Monte Carlo events from the grid point (m_1,Δm_1) as follows. For each signal Monte Carlo event at (m_1,Δm_1), the fraction, F_i, of each likelihood variable reference histogram at (m_1,Δm_1) which lies below the value of the variable, x_i, is found (see figure 5.18). The simulated event at (m,Δm) is assigned a value for each variable, x'_i, such that the fraction of the interpolated reference histogram at (m,Δm) which lies below x'_i is equal to F_i.

This method of rescaling the likelihood variable values for real signal Monte Carlo events allows the correlations between the different variables to be taken approximately into account. The method used here is similar to that used in [35], except now events from all adjacent Monte Carlo grid points are used, instead of just the nearest.

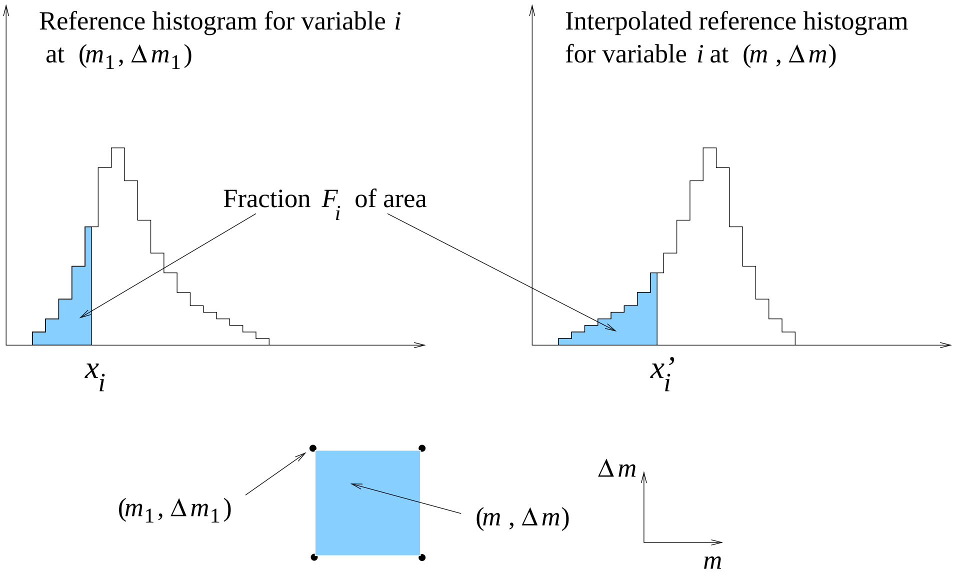

Figure 5.18: Simulation of signal Monte Carlo at arbitrary m and Δm.

5.7 Smoothing of L_R distributions

The L_R distributions for signal and background Monte Carlo are smoothed using the same smoothing algorithm used for 1D reference histograms. It is not required that there is only one peak in the smoothed histogram since the L_R distributions can have a more complicated structure. Instead the sensitivity to statistical fluctuations parameter is chosen by considering the number of peaks and the χ^2 of the fit[4].

If the sensitivity to statistical fluctuations is set too low then genuine features of the L_R distribution can be lost. To avoid this the total number of expected background events in the signal region (generally at high L_R) is compared before and after smoothing. If this has changed significantly then the smoothing is repeated with a higher sensitivity to statistical fluctuations.

---

[4] In practice this is done by minimising the empirically chosen parameter $\chi^2(1+N_{peak})/(10*ndf)$, where ndf is the number of degrees of freedom, and N_{peak} is the number of peaks in the smoothed histogram.

Smoothing the L_R distributions to reduce the effect of statistical fluctuations is very important because it allows quite narrow binning to be used for the L_R histograms. This retains sensitivity to sharp peaks close to $L_R = 0$ and $L_R = 1$ which would be lost if wider bins had to be used because of low statistics.

Examples of smoothing L_R distributions are shown in figure 5.19.

5.8 Setting Cross Section Limits

The number of events observed and their general kinematic properties are in reasonable agreement with the Standard Model expectation. The L_R distributions described in this chapter are hence used to set an upper limit at 95 % confidence level (σ_{95}) on the product of the cross-section for production of the new particle times the branching ratio squared for the decay mode being considered ($\sigma.BR^2$). An extended maximum likelihood technique is used to calculate σ_{95}. This method is the same as that described in [35], and is recapped in appendix A for the convenience of the reader.

The inputs to setting the cross-section limits at each point in the m, Δm plane are the L_R distributions for signal and background Monte Carlo, the number of expected background events with L_R greater than zero, and the general selection efficiency for signal events to have L_R greater than zero. The selection efficiency is found by linear interpolation between signal Monte Carlo gridpoints.

5.8.1 Expected Limits

Also calculated (on the Monte Carlo grid points) is the expected value of σ_{95} , $\langle\sigma_{95}\rangle$. This is the average value of σ_{95} which one would expect to observe if there is no signal present in the data. This can be used as a measure of the sensitivity of the

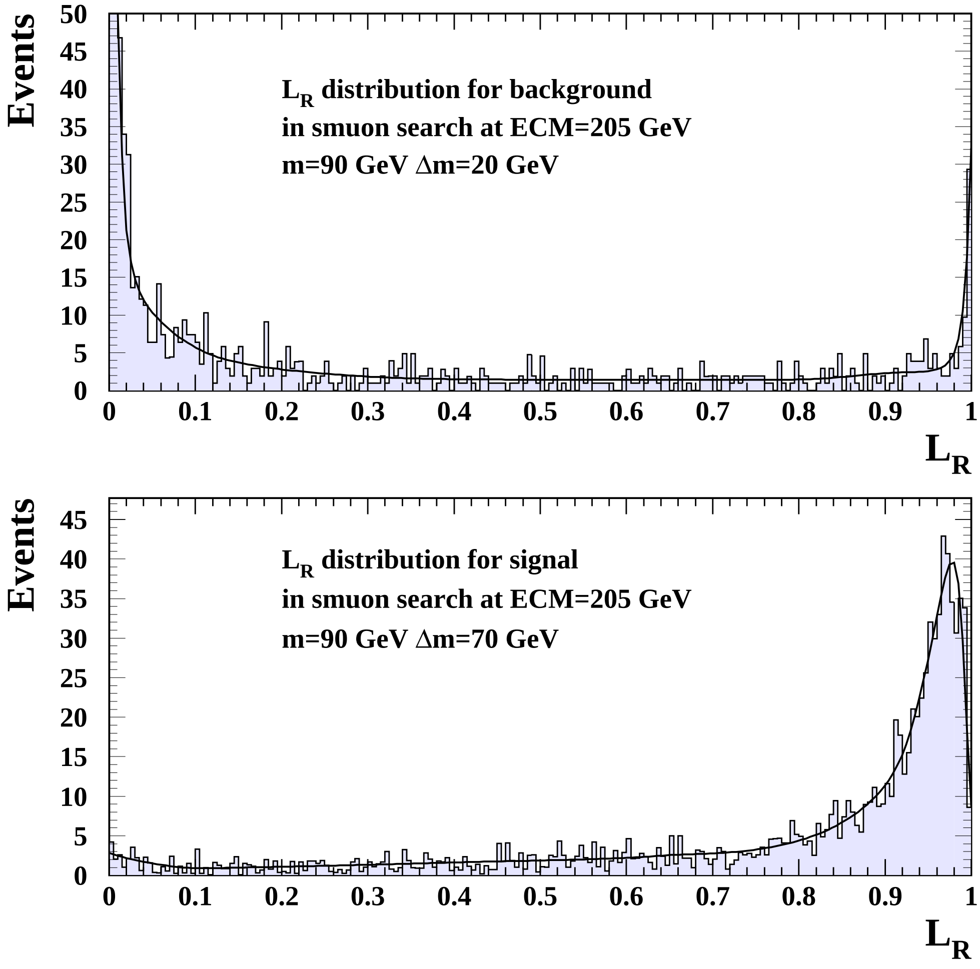

Figure 5.19: Examples of smoothing L_R distributions. The histogram shows the unsmoothed histogram and the line shows the smoothed function.

experiment.

The value of $\langle\sigma_{95}\rangle$ is calculated using 1000 "toy Standard Model Monte Carlo" experiments and taking an average of the σ_{95} values from each experiment. The number of data candidates in each experiment is taken from a Poisson distribution with mean equal to the number of background events expected. The L_R values for each event are taken at random from the Standard Model background Monte Carlo L_R distribution.

5.8.2 Confidence Levels

A Confidence Level (CL) for consistency with the Standard Model can also be assigned. This is done by comparing the value of σ_{95} observed in the data, to the set of 1000 σ_{95} values from the "toy Monte Carlo" experiments used to calculate the expected limit. The CL is defined as the probability to observe an upper limit greater than or equal to the limit observed in the data (this is the fraction of the background only Monte Carlo experiments where the limit set is larger than or equal to the data limit).

The values of the CL at neighbouring grid points can be highly correlated because the same events can contribute to the limit calculation at more than one grid point.

Some CL values of 100% are observed. This occurs when no data events with $L_R > 0$ are observed. Since σ_{95} cannot have a negative value, the toy Monte Carlo limits are always greater than or equal to the data limit, so a CL of 100% is found.

5.8.3 Overall Consistency with the Standard Model

If one looks at the Confidence Level for consistency with the Standard Model for just one hypothesized signal (ie. one search channel and one choice of m and Δm), then this value can indeed be interpreted as a probability.

Here however, many different signal hypotheses are tested (note that each value of m and Δm is considered as a different signal). This complicates the interpretation of the significance of observing low values of CL, due to dilution of the statistical significance of each point. If each grid point were uncorrelated with all others then the situation would still be relatively simple. However there is a degree of correlation between the grid points which is unknown.

Hence an additional set of 1000 toy Monte Carlo experiments is used to probe the overall significance of low CL values. In each experiment a set of background Monte Carlo events are selected, with the number of events from each background process taken from a Poisson distribution with mean equal to the expected number of events from that process.

The entire analysis chain is then applied to each of the Monte Carlo experiments as if it were the real data, and tables similar to those in the results section of this chapter (6.3) are produced for each of the six signal channels. For each experiment the lowest value of CL anywhere in the six tables is found. These values of lowest CL can then be compared the lowest value of CL observed in the real data tables.

The distribution of the lowest value of CL is shown in figure 5.20. The lowest value of CL found in the real data tables is 0.9% , at $m = 102$ GeV and $\Delta m = 67$ GeV in table 6.5. It is found that 56% of the 1000 background only toy Monte Carlo experiments have a lowest value of CL equal to or lower than 0.9%. Hence 56% can be considered as an overall measure of the consistency of the data with the Standard Model.

5.9 Systematic Errors

Monte Carlo statistical errors and other systematics are taken into account when setting the cross section limits. This signal efficiency, ϵ, is fluctuated up and down

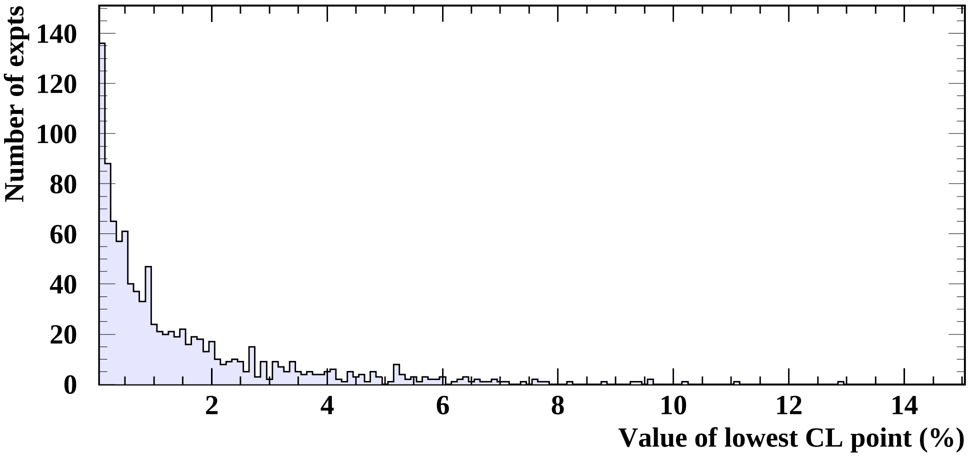

Figure 5.20: Value of lowest CL grid point for all 6 search channels in each of the 1000 toy Monte Carlo experiments.

by 0.52 and 1.28 times its total estimated error[5]. An average is found of the limits set using these 5 values of ϵ ($\epsilon - 1.28\sigma_\epsilon, \epsilon - 0.52\sigma_\epsilon, \epsilon, \epsilon + 0.52\sigma_\epsilon, \epsilon + 1.28\sigma_\epsilon$). This average is taken as the cross section limit taking into account the error on signal efficiency.

The error on the expected background is treated similarly.

In addition to the Monte Carlo statistical error on the signal efficiency, a conservative 10% systematic error is assigned to the signal selection efficiency to take into account uncertainties in trigger efficiency (less than 1%), detector occupancy ($\sim$ 1%), luminosity measurement (less than 0.3% [36–38]), the interpolation procedure (less than 5%, see section 5.9.2), fluctuations in shape of signal L_R distributions ($\sim$ 2%, see section 5.9.1), effect of tau polarisation (less than 5% [35]), and deficiencies in

---

[5] The exact size of these fluctuations is not important. They idea is to give an indication of how the limit varies as the efficiency is fluctuated up and down by a small amount comparable to the estimated error.

the signal Monte Carlo generators and the detector simulation (5%). The sensitivity of the final limit to the size of the efficiency systematic error is typically small ($\sim 1\%$).

The dominant background at high Δm to the searches presented here comes from W pair production. High statistics Monte Carlo samples for this process are used, which have been shown to describe the OPAL data well [16]. The Monte Carlo statistical error on the background at high Δm is therefore relatively small (less than 1%). At low Δm the background from $e^+e^-\ell^+\ell^-$ events becomes most important. The Monte Carlo statistics available for this process are more limited and here the statistical error dominates (typically 20-80%).

In addition to the Monte Carlo statistical errors, a systematic error of 5% is assigned to the expected background. This takes into account uncertainties in the shapes of the L_R distributions and deficiencies in the Monte Carlo detector simulation.

Some sources of systematic errors mentioned above are discussed here.

5.9.1 Signal Monte Carlo Statistics

The problem of limited signal Monte Carlo statistics presents two sources of error. Firstly there is the statistical error on the selection efficiency. This can be easily calculated and is accounted for in the limit setting procedure.

In addition to the statistical error there is an uncertainty in the shape of the signal L_R distribution. Fluctuations in this shape can affect the expected sensitivity of the search. The significance of this effect is investigated by splitting the signal Monte Carlo at each grid point into two subsets of equal size. Each of these subsets is then used independently to calculate an expected cross-section limit. In the absence of any effect due to L_R shape fluctuations the expected limit should be inversely proportional to the selection efficiency. Any deviation from this proportionality indicates that the L_R shape is important. The results of this test are shown in figure 5.21, with the grid points grouped by Δm value. The statistical fluctuations here are expected to be larger than those in the search analysis, because the signal Monte Carlo sets being compared have been halved in size.

At low values of Δm (2, 2.5, 5 GeV) the L_R shape fluctuations are seen to be unimportant. This is to be expected since the L_R distributions in this region of phase space are well approximated by a spike at $L_R = 1$. An event is either selected or not, and no additional discrimination is derived from the L_R shape. At higher Δm values L_R shape fluctuations do become important.

A large sample of 40000 smuon events was generated at $m = 80$ GeV, $\Delta m = 40$ GeV to quantify the size of this error. This is in the high Δm region where the effect is expected to be most significant, and corresponds to 40 subsets of the size used in the search analysis. Each of these subsets is used independently to calculate an expected cross-section limit. The size of the additional error due to L_R shape fluctuations is estimated to be 2%, by comparing the spread of values of the expected limit with the spread of selection efficiencies from the 40 subsets (see figure 5.22). This error is treated as a contribution to the systematic error on the signal selection efficiency.

5.9.2 Interpolation

Another source of signal systematic error is the interpolation procedure which allows the search for signals at intermediate points between those where signal Monte Carlo has been generated.

The interpolation in m and Δm has previously been shown to lead to only a small error of less than 5% [35]. The interpolation in $\sqrt{s}$ is tested by calculating expected cross-section limits ($\langle\sigma_{95}\rangle$) for smuons at 196 GeV both using signal Monte Carlo generated at 196 GeV and by interpolating signal Monte Carlo between 189 and 200 GeV. This is the largest distance in $\sqrt{s}$ over which the interpolation is required,

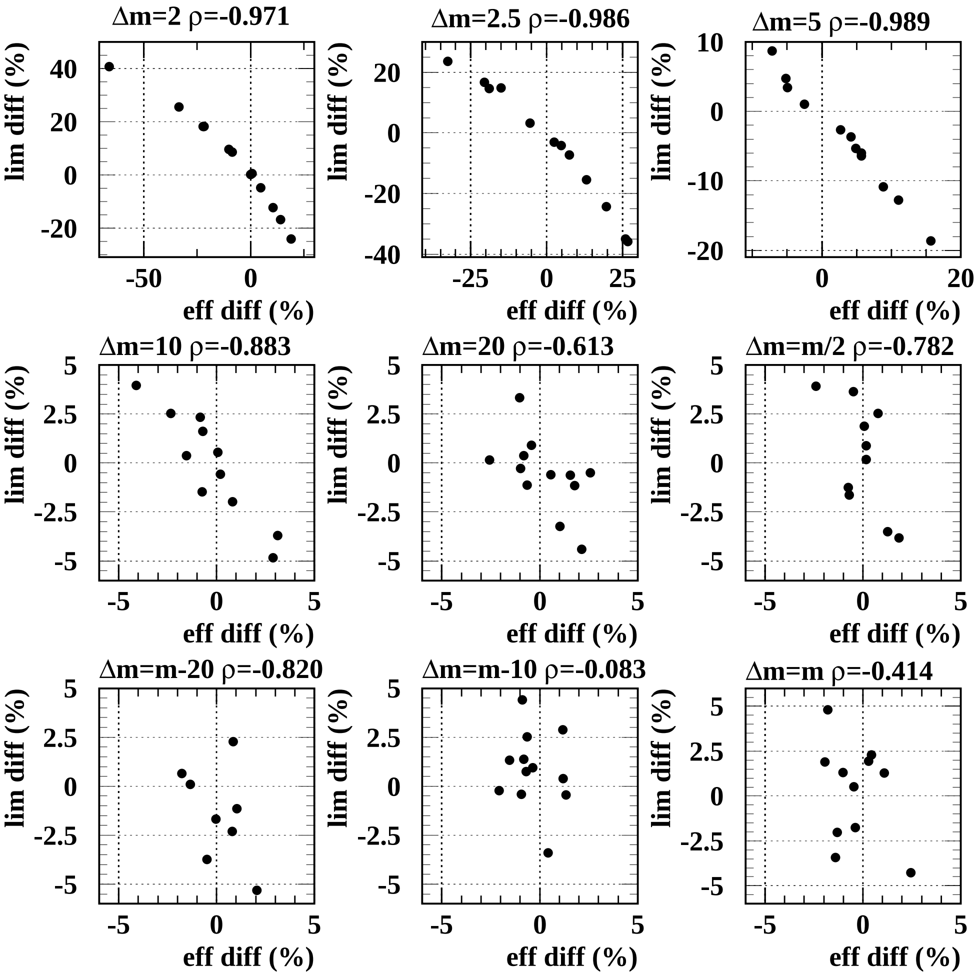

Figure 5.21: Change in expected limit versus change in efficiency at different values of Δm.

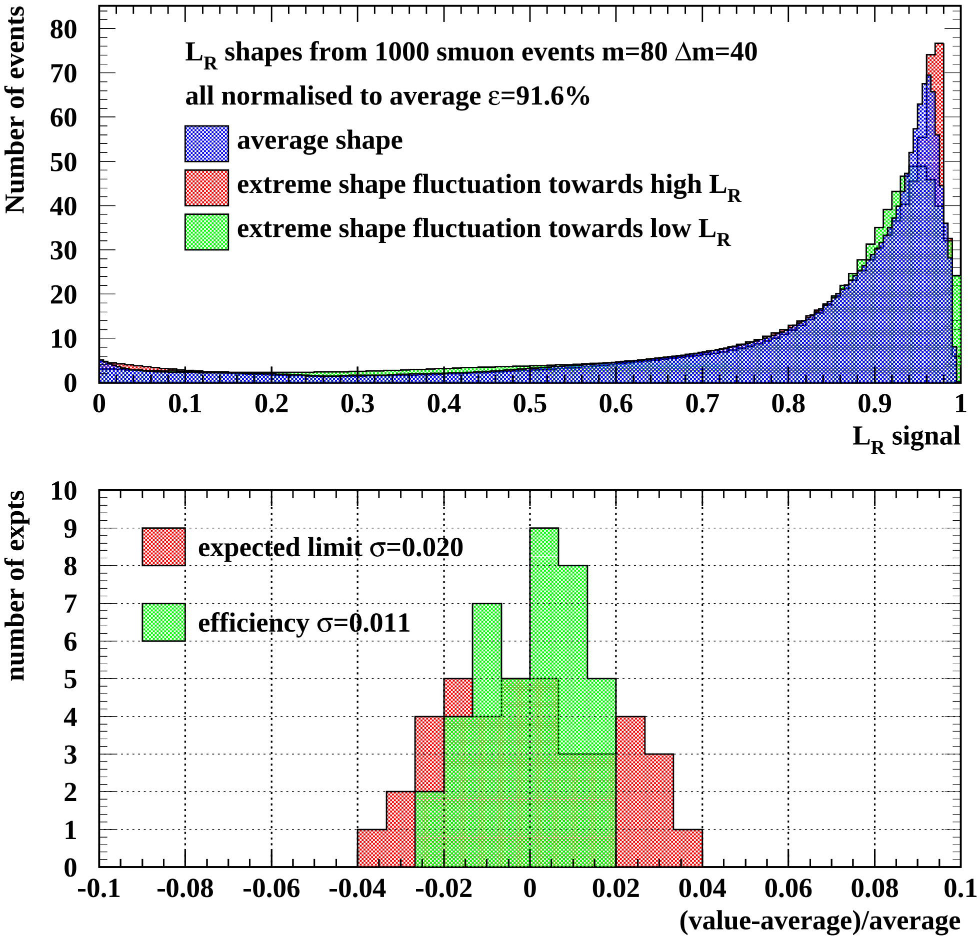

Figure 5.22: Top plot: Example signal L_R distributions illustrating extremes of variation (green and red histograms) and the average (blue histogram). Lower plot: Spread of expected limits (red histogram) and spread in signal selection efficiencies (green histogram) obtained from the 40 sets of 1000 smuon signal Monte Carlo events generated at $m = 80$ GeV and Δm=40 GeV.

and so should give a conservative estimate of the error due to interpolation. The variations in $\langle\sigma_{95}\rangle$ are generally small and are within the confines of those expected due to the different Monte Carlo statistics being used (see figure 5.23). The significance of the variations is further reduced in the final limits quoted at 208 GeV because only about half of the data luminosity was taken at $\sqrt{s}$ values where interpolation is necessary. Hence the error due to interpolation in m and Δm of 5% is also sufficient to account for errors in $\sqrt{s}$ interpolation.

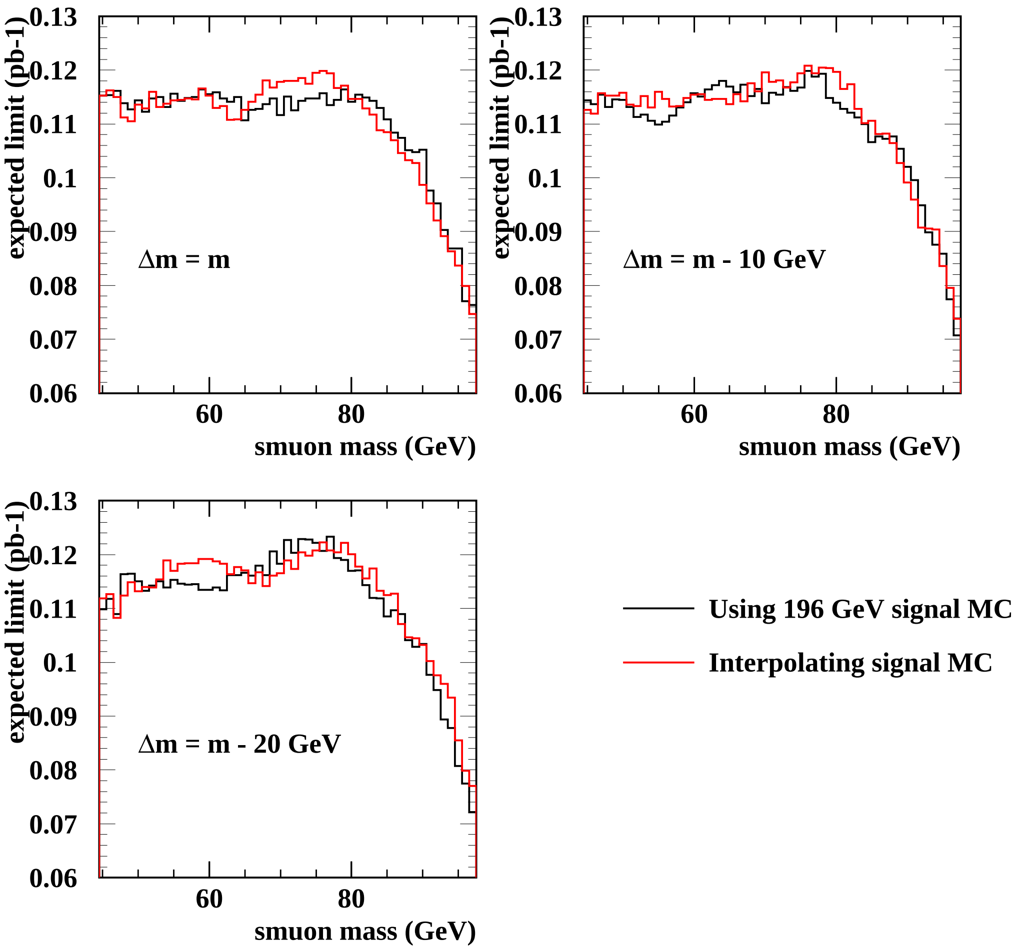

Figure 5.23: Plots showing $\langle\sigma_{95}\rangle$ calculated at 196 GeV by interpolating signal Monte Carlo between 189 and 200 GeV (red line) and using signal Monte Carlo generated at 196 GeV (black line), at (a) $\Delta m = m$, (b) $\Delta m = m - 10$ GeV, (c) $\Delta m = m - 20$ GeV.

Chapter 6

Search Results

6.1 Cross-section limit contour plots

Contour plots in the m, Δm plane showing the 95% confidence level upper limit on cross-section times branching ratio for each search channel are now presented (figures 6.1 to 6.3).

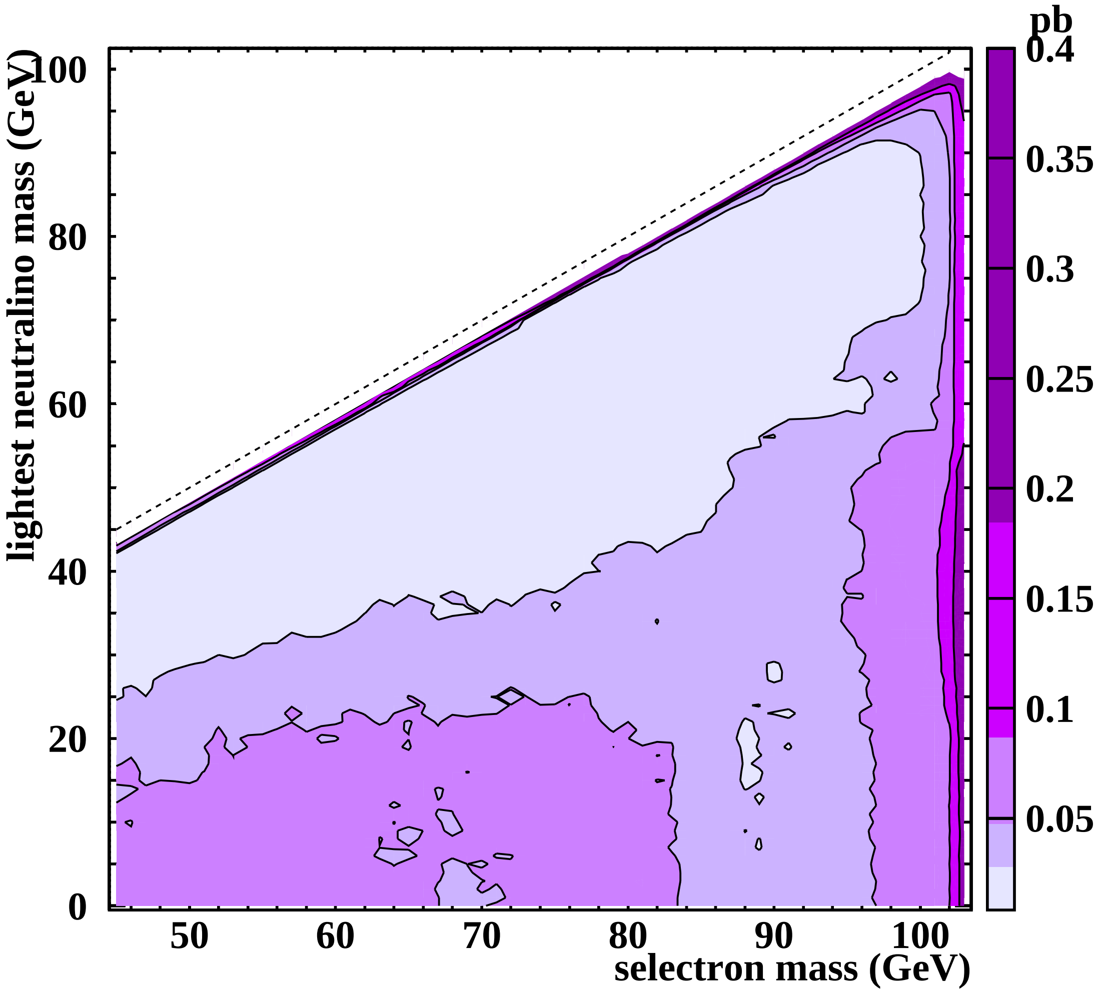

Figure 6.1: Contours of the 95% CL upper limits on the selectron pair cross-section times $BR^2(\tilde{e}^- \rightarrow e^\pm\tilde{\chi}_1^0)$ at $\sqrt{s}$=208 GeV based on combining the 183-208 GeV OPAL data-sets assuming a β^3/s dependence of the cross-section. The kinematically allowed region is indicated by the dashed line. The unshaded region at very low Δm is experimentally inaccessible in this search.

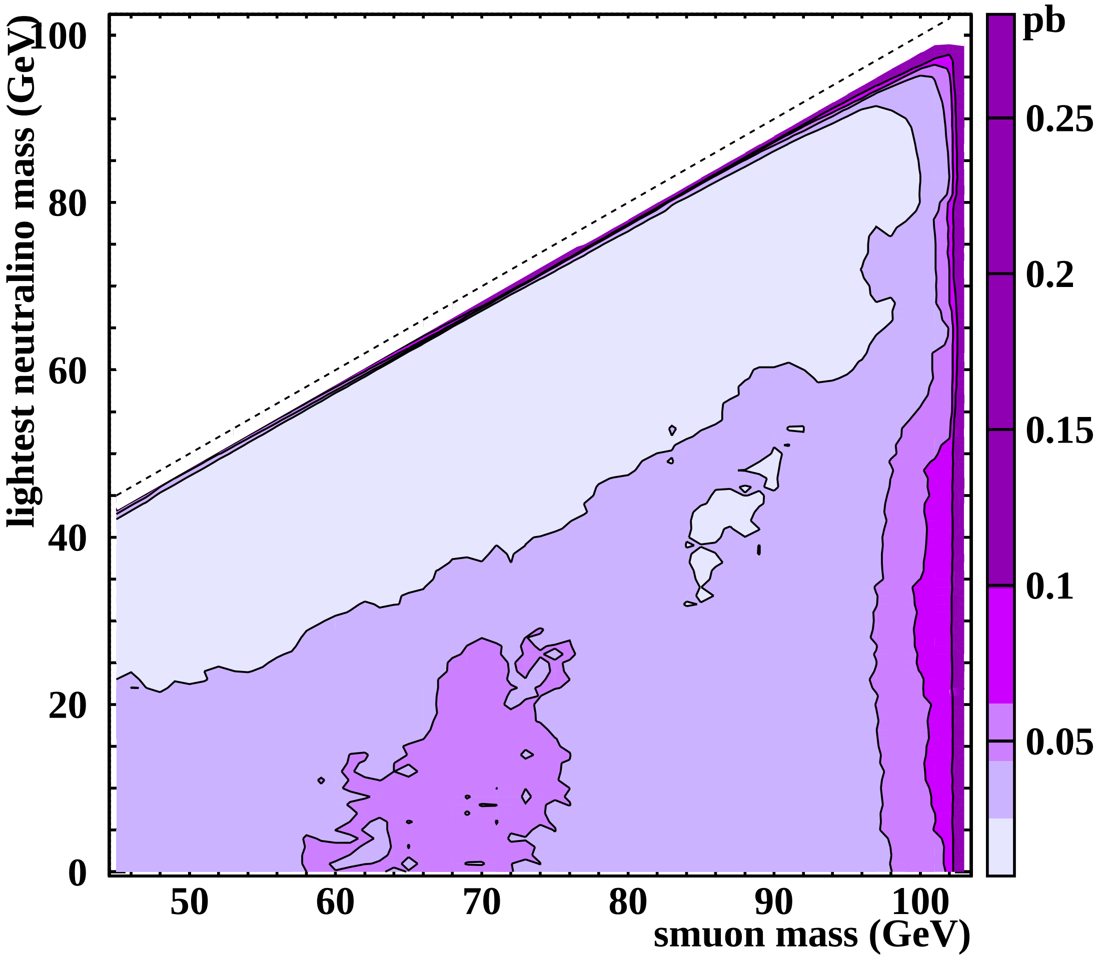

Figure 6.2: Contours of the 95% CL upper limits on the smuon pair cross-section times $BR^2(\tilde{\mu}^- \rightarrow \mu\tilde{\chi}_1^0)$ at $\sqrt{s}$=208 GeV based on combining the 183-208 GeV OPAL data-sets assuming a β^3/s dependence of the cross-section. The kinematically allowed region is indicated by the dashed line. The unshaded region at very low Δm is experimentally inaccessible in this search.

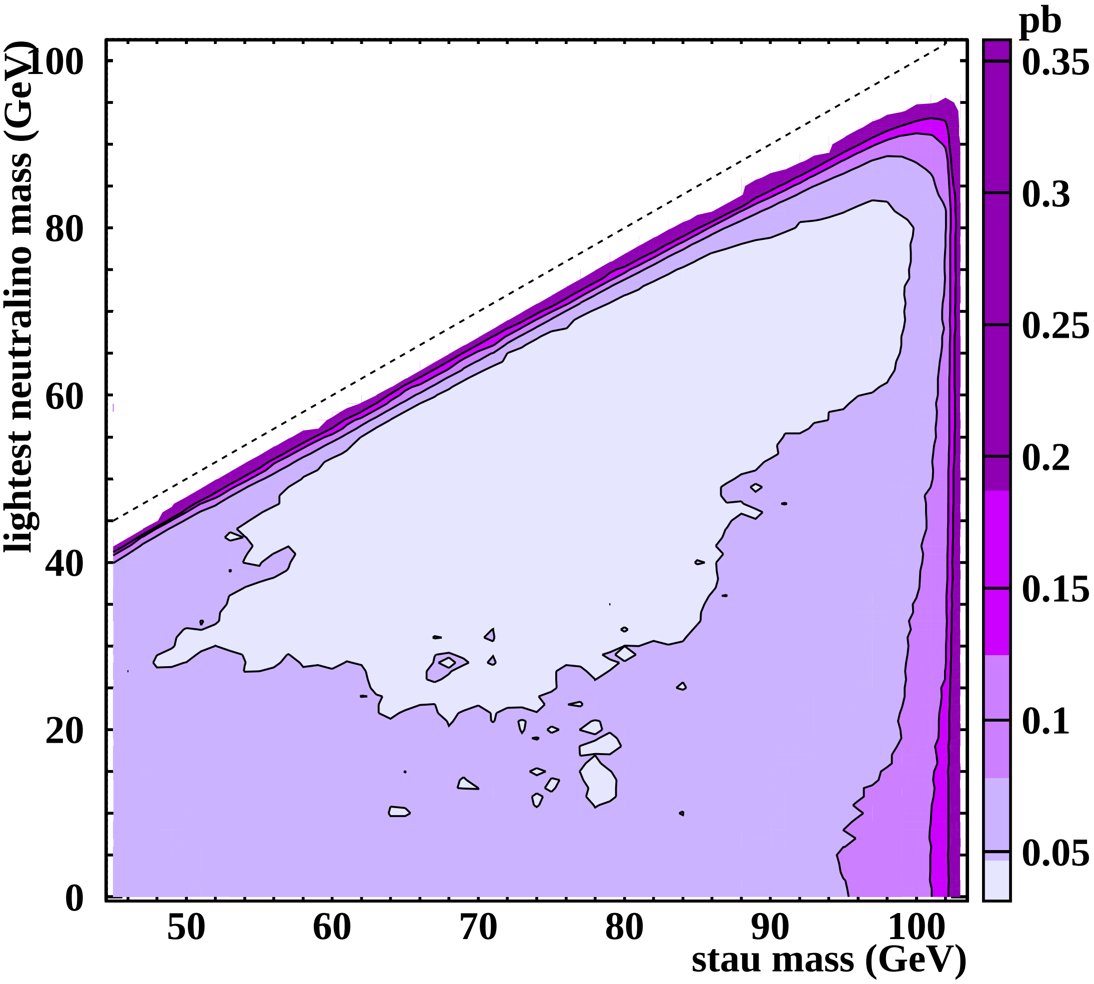

Figure 6.3: Contours of the 95% CL upper limits on the stau pair cross-section times $BR^2(\tilde{\tau}^- \rightarrow \tau\tilde{\chi}_1^0)$ at $\sqrt{s}$=208 GeV based on combining the 183-208 GeV OPAL datasets assuming a β^3/s dependence of the cross-section. The kinematically allowed region is indicated by the dashed line. The unshaded region at very low Δm is experimentally inaccessible in this search.

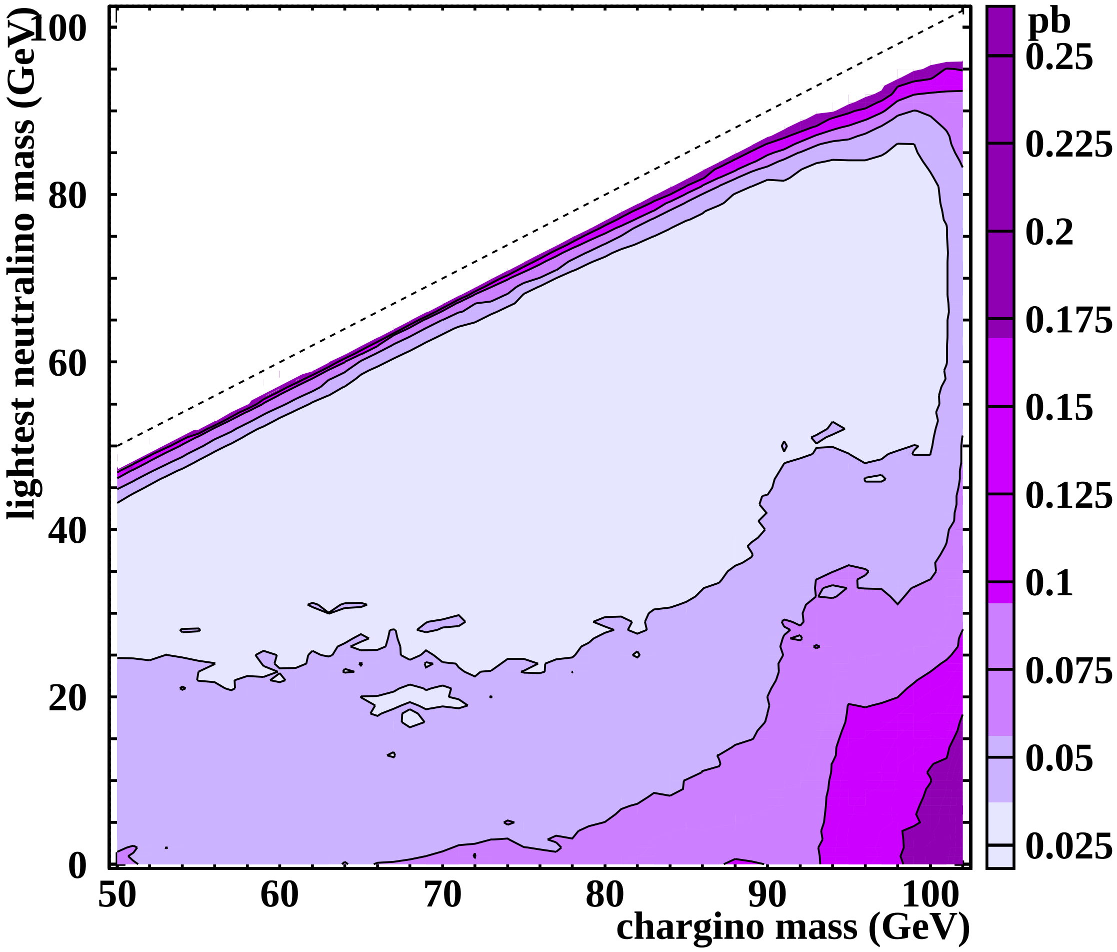

Figure 6.4: Contours of the 95% CL upper limits on the chargino pair cross-section times $BR^2(\tilde{\chi}_1^{\pm} \rightarrow \ell^{\pm}\nu\tilde{\chi}_1^0)$ (3-body decays) at $\sqrt{s}$=208 GeV based on combining the 183-208 GeV OPAL data-sets assuming a β/s dependence of the cross-section. The kinematically allowed region is indicated by the dashed line. The unshaded region at very low Δm is experimentally inaccessible in this search.

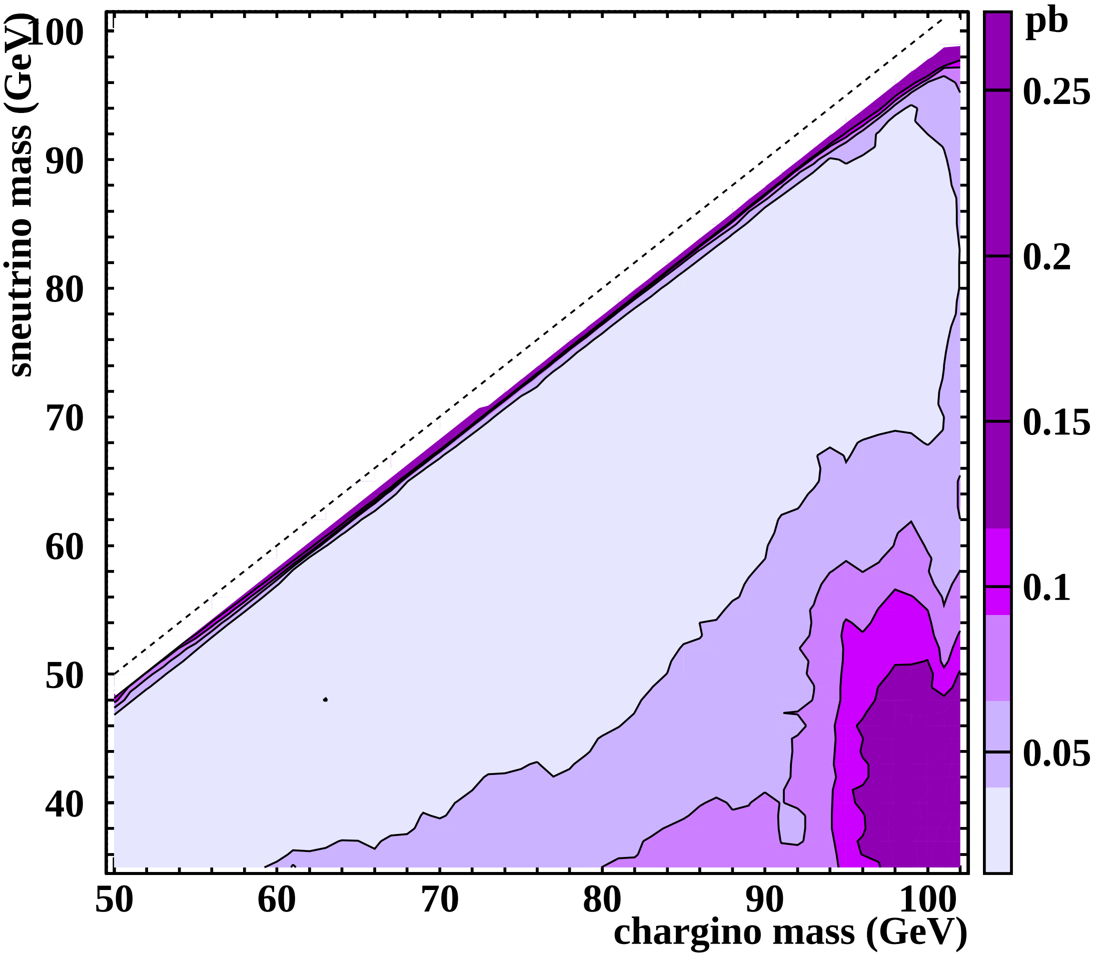

Figure 6.5: Contours of the 95% CL upper limits on the chargino pair cross-section times $BR^2(\tilde{\chi}_1^\pm \rightarrow \ell^\pm\tilde{\nu})$ (2-body decays) at $\sqrt{s}$=208 GeV based on combining the 183-208 GeV OPAL data-sets assuming a β/s dependence of the cross-section. The kinematically allowed region is indicated by the dashed line. The unshaded region at very low Δm is experimentally inaccessible in this search.

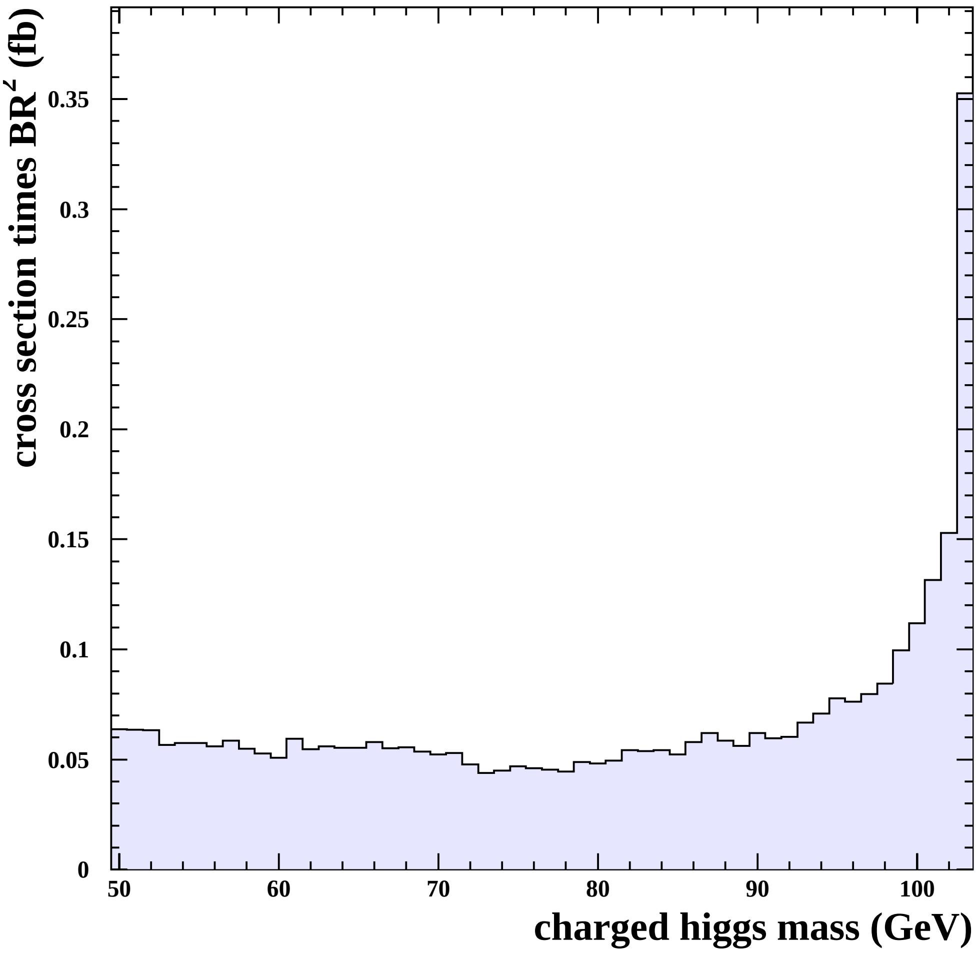

Figure 6.6: 95% CL upper limits on the charged higgs pair cross-section times $BR^2(\mathrm{H}^\pm \to \tau\tilde{\chi}_1^0)$ at $\sqrt{s}$=208 GeV based on combining the 183-208 GeV OPAL data-sets assuming a β^3/s dependence of the cross-section.

6.2 Mass limits for MSSM sleptons

The cross section limits from the previous section can be used to set limits on the masses of right handed sleptons[1] based on the expected right handed slepton pair production cross sections and branching ratios. The cross sections have been calculated at $\sqrt{s} = 208$ GeV using Susygen and take into account initial state radiation. Figure 6.7 shows the limits on right handed smuons and staus as a function of slepton mass and lightest neutralino mass, for several assumed values of the branching ratio squared for the decay $\tilde{\ell}^{\pm}_{R} \rightarrow \ell^{\pm}\tilde{\chi}^{0}_{1}$. For an assumed BR^2 of 1.0, smuons are excluded at 95% CL for masses below 94.0 GeV for $m_{\tilde{\mu}} - m_{\tilde{\chi}^0} > 4$ GeV. Staus are excluded at 95% CL for masses below 89.5 GeV for $m_{\tilde{\tau}} - m_{\tilde{\chi}^0} > 8$ GeV.

An alternative approach is to set limits taking into account the predicted cross-section and branching ratio for specific choices of the parameters within the MSSM. For $\mu < -100$ GeV and for two values of $\tan\beta$ (1.5 and 35), figure 6.8 shows the 95% CL exclusion regions in the $(m_{\tilde{\ell}^{\pm}_{R}}, m_{\tilde{\chi}^{0}_{1}})$ plane for right-handed selectrons, smuons and staus. For $\mu < -100$ GeV and $\tan\beta$ =1.5, right handed selectrons are excluded at 95% CL with masses below 97.5 GeV for $m_{\tilde{e}} - m_{\tilde{\chi}^0} > 10$ GeV.

---

[1] The right handed slepton is expected to be lighter than the left handed slepton. In addition the right handed slepton pair production cross section is expected to have a lower pair production cross section (not generally true for selectrons), so conventionally limits are given for this (usually) conservative case.

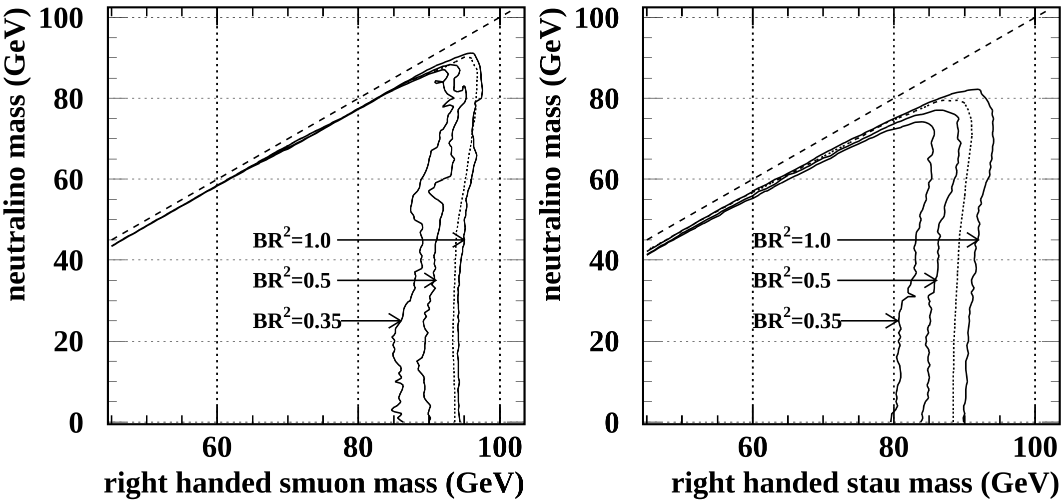

Figure 6.7: 95% CL exclusion regions for right handed smuon and stau pair production obtained by combining the $\sqrt{s} = 183 - 208$ GeV data sets. The limits are calculated for several values of the branching ratio squared for $\tilde{\ell}^{\pm}_R \to \ell^{\pm}\tilde{\chi}^0_1$ that are indicated in the figure. Otherwise they have no supersymmetry model assumptions. The kinematically allowed region is indicated by the dashed line. The expected limit for BR^2=1.0, calculated from Monte Carlo alone, is indicated by the dotted line.

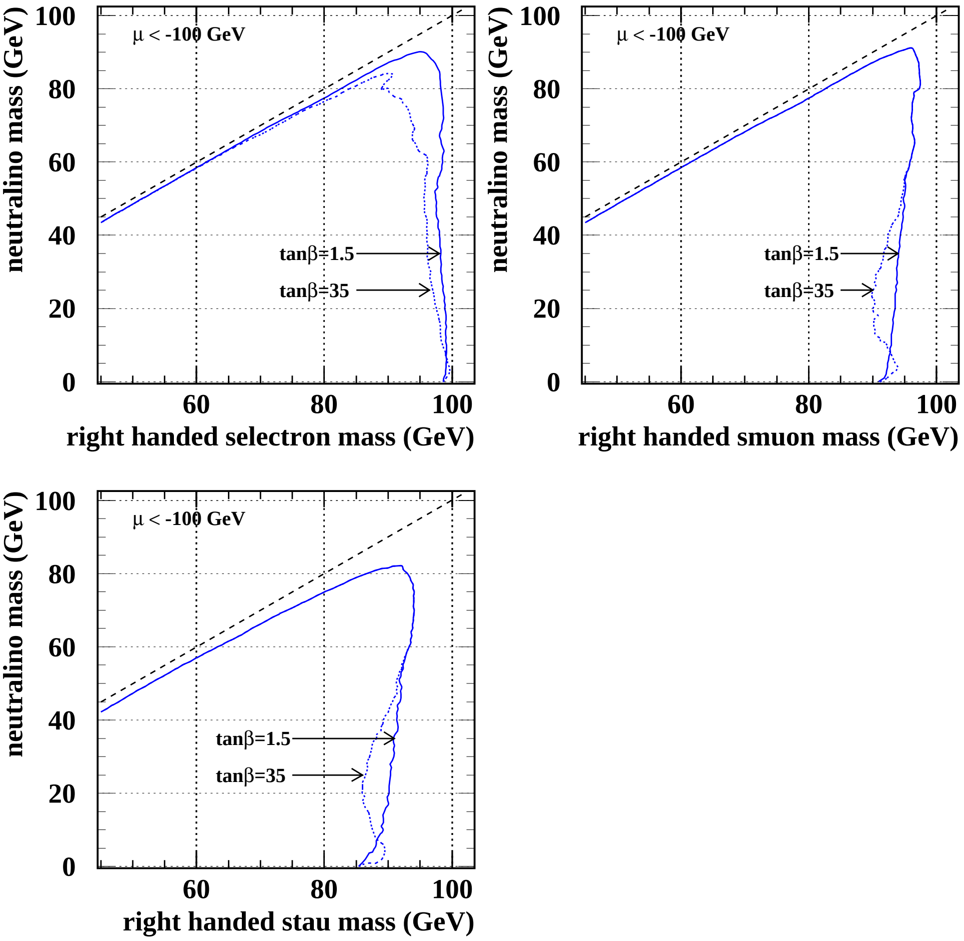

Figure 6.8: For two values of $\tan\beta$ and $\mu < -100$ GeV, 95% CL exclusion regions for right-handed slepton pairs within the MSSM, obtained by combining the $\sqrt{s} = 183 - 208$ GeV data. The excluded regions are calculated taking into account the predicted branching ratio for $\tilde{\ell}^{\pm}_{R} \rightarrow \ell^{\pm}\tilde{\chi}^{0}_{1}$. The gauge unification relation, $M_1 = \frac{5}{3}\tan^2\theta_W M_2$, is assumed in calculating the MSSM cross-sections and branching ratios. The kinematically allowed region is indicated by the dashed line.

6.3 Summary Tables

Over the next pages (tables 6.1 to 6.6) follow summary tables showing at $\sqrt{s} = 208$ GeV, for each search channel and selected values of m and Δm the general selection efficiency, the 95% CL upper limit on cross-section times branching ratio squared, the expected upper limit on cross-section times branching ratio squared, and the CL for consistency with the Standard Model.

Table 6.1 shows results for the search for $\tilde{\mathrm{e}}^+\tilde{\mathrm{e}}^-$ production, followed by the decay $\tilde{\mathrm{e}}^\pm \to \mathrm{e}^\pm\tilde{\chi}^0_1$.

Table 6.2 shows results for the search for $\tilde{\mu}^+\tilde{\mu}^-$ production, followed by the decay $\tilde{\mu}^\pm \to \mu^\pm\tilde{\chi}^0_1$.

Table 6.3 shows results for the search for $\tilde{\tau}^+\tilde{\tau}^-$ production, followed by the decay $\tilde{\tau}^\pm \to \tau^\pm\tilde{\chi}^0_1$.

Table 6.4 shows results for the search for $\tilde{\chi}^+_1\tilde{\chi}^-_1$ production, followed by the 3-body decay decay $\tilde{\chi}^\pm_1 \to \ell^\pm\nu\tilde{\chi}^0_1$.

Table 6.4 shows results for the search for $\tilde{\chi}^+_1\tilde{\chi}^-_1$ production, followed by the 2-body decay decay $\tilde{\chi}^\pm_1 \to \ell^\pm\tilde{\nu}$. The bins without entries at $m_{\tilde{\chi}^\pm} = 50$ GeV correspond to values of $m_{\tilde{\nu}} > 35$ GeV, which are excluded and therefore not considered in this analysis.

Table 6.6 shows results for the search for $\mathrm{H}^+\mathrm{H}^-$ production, followed by the decay decay $\mathrm{H}^\pm \to \tau^\pm\nu_\tau$.

Δm (GeV)	$m_{\tilde{e}^-}$ (GeV) 45	50	55	60	65	70	75	80	85	90	94	99	103
General Selection Efficiency (%)													
2	5.0±0.7	3.8±0.6	4.5±0.7	2.2±0.5	2.0±0.4	1.6±0.4	1.2±0.3	0.8±0.3	0.6±0.2	0.5±0.2	0.5±0.2	0.1±0.1	0.0±0.0
2.5	5.0±0.7	3.8±0.6	4.5±0.7	2.2±0.5	2.0±0.4	1.6±0.4	1.2±0.3	0.8±0.3	0.6±0.2	0.5±0.2	0.5±0.2	0.1±0.1	0.0±0.0
5	40.7±1.6	42.9±1.6	41.9±1.6	44.5±1.6	45.0±1.6	43.5±1.6	43.1±1.6	39.9±1.5	41.6±1.6	44.1±1.6	43.1±1.6	42.3±1.6	42.4±1.6
10	60.9±1.5	64.8±1.5	65.4±1.5	66.4±1.5	67.7±1.5	67.2±1.5	65.9±1.5	67.8±1.5	66.0±1.5	67.4±1.5	67.4±1.5	66.6±1.5	67.8±1.5
20	74.8±1.4	76.3±1.3	77.4±1.3	79.1±1.3	81.2±1.2	82.4±1.2	82.5±1.2	81.1±1.2	81.4±1.2	81.3±1.2	82.1±1.2	83.3±1.2	80.2±1.3
$m/2$	75.0±1.4	78.6±1.3	79.4±1.3	83.2±1.2	85.9±1.1	84.4±1.1	85.5±1.1	87.8±1.0	88.2±1.0	87.8±1.0	88.5±1.0	88.5±1.0	89.4±1.0
m-20	74.9±1.4	81.7±1.2	82.1±1.2	83.6±1.2	84.2±1.2	84.9±1.1	88.4±1.0	86.0±1.1	88.1±1.0	89.9±1.0	90.9±0.9	90.2±0.9	90.8±0.9
m-10	74.6±1.4	79.3±1.3	79.8±1.3	82.0±1.2	85.2±1.1	85.2±1.1	89.1±1.0	89.2±1.0	88.7±1.0	90.7±0.9	90.1±0.9	90.3±0.9	90.5±0.9
m	69.5±1.5	77.3±1.3	80.8±1.2	83.1±1.2	85.0±1.1	88.2±1.0	87.3±1.1	89.2±1.0	89.5±1.0	88.5±1.0	91.1±0.9	90.4±0.9	91.1±0.9
95% CL upper limit on cross-section times $BR^2(\tilde{e}^- \to e\tilde{\chi}_1^0)$ (fb)													
2	82.1	86.6	99.4	138.9	113.4	159.5	293.7	412.2	1226.4	2529.9	5017.4	–	–
2.5	34.0	33.7	36.3	39.6	43.5	35.4	43.7	58.6	85.9	135.8	256.1	975.0	–
5	13.8	11.6	12.1	12.3	9.6	15.0	10.3	11.9	12.7	21.4	23.2	36.9	270.3
10	14.0	17.2	12.9	9.7	10.2	10.3	10.0	10.2	10.6	11.1	14.9	23.9	174.4
20	26.9	23.4	21.8	19.1	16.6	21.0	21.5	16.5	13.2	13.0	14.1	22.6	161.8
$m/2$	34.4	35.0	37.2	34.6	34.2	27.9	25.7	31.0	31.2	37.5	40.3	75.6	282.4
m-20	39.6	43.1	49.7	45.7	47.6	53.7	60.8	47.7	35.2	30.2	34.3	60.1	243.4
m-10	48.3	56.3	56.1	56.5	49.4	48.1	61.7	54.8	42.2	33.9	40.3	52.9	227.6
m	56.0	59.3	61.3	52.0	51.2	46.7	53.9	62.9	39.7	36.5	37.9	54.8	228.6
expected upper limit on cross-section times $BR^2(\tilde{e}^- \to e\tilde{\chi}_1^0)$ (fb)													
2	78.1	83.2	98.5	122.0	142.8	192.3	341.6	474.0	1363.7	2728.3	5277.2	–	–
2.5	34.4	38.1	39.8	42.0	43.4	46.8	56.0	72.8	98.9	150.2	274.6	1005.4	–
5	15.6	15.4	15.5	15.4	14.4	15.0	15.6	15.9	16.4	20.0	27.0	41.1	273.7
10	18.0	15.6	14.4	13.4	12.7	12.6	12.1	12.4	13.2	16.0	19.9	29.4	188.4
20	29.9	26.7	24.1	22.1	21.3	18.6	17.6	17.2	17.7	19.3	21.8	27.3	170.7
$m/2$	34.0	32.9	32.2	32.8	31.9	32.9	33.4	35.3	38.9	42.1	43.7	45.9	190.7
m-20	36.0	37.1	37.8	39.1	40.2	42.6	44.8	48.4	48.3	49.1	50.8	54.9	218.7
m-10	38.0	38.3	37.2	38.5	40.3	44.6	46.4	49.5	48.8	47.7	51.1	55.0	217.9
m	38.9	37.5	37.9	38.9	40.8	43.0	47.5	49.7	47.7	48.8	49.7	53.9	215.7
CL for consistency with SM (%)													
2	33.4	34.1	39.3	24.0	100.0	100.0	100.0	100.0	100.0	100.0	100.0	–	–
2.5	42.6	57.2	53.4	46.4	42.8	63.1	100.0	100.0	100.0	100.0	100.0	100.0	–
5	57.7	73.5	72.8	68.0	85.2	44.5	87.2	73.9	71.2	35.4	100.0	100.0	100.0
10	72.9	32.2	56.0	81.0	67.8	66.8	63.3	69.0	68.6	88.9	100.0	66.3	100.0
20	54.3	59.4	54.8	58.4	69.9	30.6	22.8	47.6	76.0	87.4	95.3	64.2	40.1
$m/2$	42.2	36.2	26.4	37.2	36.1	63.4	74.5	58.4	67.4	55.1	52.5	5.3	7.2
m-20	32.3	27.5	17.5	28.1	24.9	19.6	14.9	45.6	79.5	91.4	85.1	32.3	27.1
m-10	18.8	8.4	7.3	9.4	20.9	34.5	14.2	32.4	62.0	79.6	70.4	45.9	33.6
m	9.9	5.3	4.4	16.3	21.5	33.7	30.5	18.8	65.6	75.5	73.6	42.0	34.2

Table 6.1: Selectron results summary table

Δm	$m_{\tilde{\mu}^-}$ (GeV)												
(GeV)	45	50	55	60	65	70	75	80	85	90	94	99	103
General Selection Efficiency (%)													
2	8.9±0.9	8.5±0.9	7.0±0.8	4.3±0.6	5.1±0.7	2.7±0.5	2.0±0.4	0.5±0.2	0.6±0.2	0.2±0.1	0.3±0.2	0.1±0.1	0.0±0.0
2.5	8.9±0.9	8.5±0.9	7.0±0.8	4.3±0.6	5.1±0.7	2.7±0.5	2.0±0.4	0.5±0.2	0.6±0.2	0.2±0.1	0.3±0.2	0.1±0.1	0.0±0.0
5	53.1±1.6	53.3±1.6	50.7±1.6	52.0±1.6	51.3±1.6	50.6±1.6	47.0±1.6	48.2±1.6	48.4±1.6	48.9±1.6	47.4±1.6	47.4±1.6	46.4±1.6
10	71.1±1.4	73.4±1.4	70.6±1.4	71.8±1.4	70.1±1.4	69.6±1.5	70.3±1.4	65.9±1.5	73.3±1.4	70.9±1.4	69.9±1.5	70.7±1.4	70.0±1.4
20	82.6±1.2	82.7±1.2	84.4±1.1	83.8±1.2	84.9±1.1	83.4±1.2	85.7±1.1	82.1±1.2	84.7±1.1	83.2±1.2	83.3±1.2	83.4±1.2	83.5±1.2
$m/2$	84.0±1.2	85.8±1.1	86.5±1.1	87.8±1.0	90.3±0.9	88.2±1.0	89.2±1.0	91.5±0.9	92.1±0.9	91.3±0.9	91.3±0.9	92.7±0.8	92.5±0.8
m-20	83.4±1.2	87.1±1.1	89.4±1.0	89.6±1.0	90.0±0.9	91.3±0.9	92.6±0.8	93.4±0.8	92.4±0.8	93.5±0.8	93.3±0.8	92.9±0.8	93.3±0.8
m-10	88.6±1.0	87.9±1.0	89.2±1.0	90.0±0.9	91.8±0.9	91.3±0.9	93.0±0.8	90.1±0.9	93.2±0.8	93.3±0.8	93.5±0.8	94.2±0.7	94.6±0.7
m	88.6±1.0	88.8±1.0	88.1±1.0	91.3±0.9	92.1±0.9	93.3±0.8	91.6±0.9	93.5±0.8	93.6±0.8	92.8±0.8	92.1±0.9	93.5±0.8	94.5±0.7
95% CL upper limit on cross-section times $BR^2(\tilde{\mu}^- \rightarrow \mu\tilde{\chi}^0_1)$ (fb)													
2	49.6	43.4	52.6	64.5	88.0	151.6	241.9	522.0	1383.0	3412.7	4815.0	–	–
2.5	28.2	23.0	23.6	26.7	30.1	34.3	39.6	52.7	61.1	107.6	206.1	584.4	8845.1
5	11.9	12.1	10.0	10.1	10.4	10.9	11.6	10.0	11.6	14.9	20.2	33.3	245.1
10	14.4	11.1	8.4	7.8	7.1	7.8	6.9	8.3	11.3	14.6	21.2	23.7	172.8
20	21.2	16.4	13.3	12.4	12.2	11.6	11.3	10.1	14.3	16.4	19.6	21.9	146.3
$m/2$	25.3	20.6	18.9	28.2	25.2	34.6	29.7	34.5	22.1	26.1	30.6	49.6	199.8
m-20	30.4	28.1	31.9	36.5	38.7	49.7	41.0	36.1	35.2	35.6	36.0	53.9	260.5
m-10	28.5	35.5	36.7	43.0	45.3	50.1	43.9	34.6	35.7	34.9	35.2	50.8	240.5
m	31.7	33.8	37.0	43.8	44.0	46.4	36.2	37.9	32.3	32.3	34.0	48.4	222.3
expected upper limit on cross-section times $BR^2(\tilde{\mu}^- \rightarrow \mu\tilde{\chi}^0_1)$ (fb)													
2	44.3	46.5	56.1	67.2	93.0	145.0	229.2	493.8	1602.8	3575.8	4968.0	–	–
2.5	25.5	25.1	27.0	28.8	32.1	36.0	43.1	52.3	72.8	123.6	230.6	601.3	8865.5
5	12.9	12.8	12.8	12.1	12.6	12.9	12.9	13.5	15.8	19.7	25.1	38.6	267.0
10	13.3	12.7	11.8	11.5	11.2	10.7	10.6	11.0	11.7	13.6	17.3	26.1	176.7
20	20.8	19.7	18.9	17.7	17.2	16.6	15.9	15.8	16.0	17.6	20.2	26.8	159.5
$m/2$	22.6	22.9	23.4	24.6	24.7	26.8	27.6	29.6	32.6	36.4	38.6	44.5	195.8
m-20	23.3	25.1	25.9	26.8	28.6	29.4	32.1	35.2	37.3	39.9	42.2	47.9	208.5
m-10	24.0	24.5	24.8	25.8	27.8	29.4	32.9	35.2	35.5	39.0	40.2	46.6	221.7
m	23.8	23.2	24.3	26.0	27.3	29.5	32.0	34.9	35.8	37.6	40.3	46.5	217.9
CL for consistency with SM (%)													
2	29.5	51.4	55.8	53.4	52.9	44.5	41.7	43.5	100.0	100.0	100.0	–	–
2.5	32.3	59.9	63.4	61.7	51.1	60.6	59.8	47.7	100.0	100.0	100.0	100.0	100.0
5	52.0	47.7	76.7	71.4	71.8	70.8	61.9	68.7	66.5	100.0	100.0	100.0	100.0
10	31.9	57.9	80.2	84.9	91.3	77.9	92.0	71.2	49.8	35.9	19.7	100.0	100.0
20	40.9	62.6	81.9	83.7	82.1	83.0	80.2	87.4	54.5	51.1	44.3	70.4	75.4
$m/2$	30.6	54.6	68.9	29.1	41.7	18.4	34.7	26.9	83.5	80.0	69.4	29.7	39.2
m-20	17.2	29.3	23.3	13.5	14.5	4.4	18.7	42.6	49.7	56.1	61.9	30.1	17.1
m-10	25.8	9.9	8.1	3.4	4.9	3.0	15.5	45.9	42.4	56.5	59.3	31.6	29.8
m	16.6	9.6	7.6	3.5	5.6	6.9	29.0	34.7	55.6	59.1	63.2	36.5	39.5

Table 6.2: Smuon results summary table.

Δm	$m_{\tilde{\tau}^-}$ (GeV)												
(GeV)	45	50	55	60	65	70	75	80	85	90	94	99	103
General Selection Efficiency (%)													
2	0.1±0.0	0.0±0.0	0.0±0.0	0.0±0.0	0.0±0.0	0.0±0.0	0.0±0.0	0.0±0.0	0.0±0.0	0.0±0.0	0.0±0.0	0.0±0.0	0.0±0.0
2.5	0.1±0.0	0.0±0.0	0.0±0.0	0.0±0.0	0.0±0.0	0.0±0.0	0.0±0.0	0.0±0.0	0.0±0.0	0.0±0.0	0.0±0.0	0.0±0.0	0.0±0.0
5	11.0±0.4	10.5±0.4	9.4±0.4	8.5±0.4	7.6±0.4	7.6±0.4	6.7±0.4	6.4±0.3	5.5±0.3	4.5±0.3	4.3±0.3	4.0±0.3	3.9±0.3
10	33.4±0.7	33.8±0.7	34.8±0.7	32.5±0.7	32.0±0.7	31.8±0.7	30.2±0.6	30.9±0.7	28.8±0.6	26.6±0.6	26.6±0.6	25.0±0.6	25.1±0.6
20	54.4±0.7	56.0±0.7	55.3±0.7	56.4±0.7	56.1±0.7	54.8±0.7	57.7±0.7	55.5±0.7	55.4±0.7	54.8±0.7	54.0±0.7	55.0±0.7	54.8±0.7
$m/2$	57.0±0.7	60.0±0.7	62.7±0.7	65.5±0.7	67.3±0.7	69.4±0.7	68.9±0.7	70.3±0.6	72.1±0.6	74.0±0.6	74.0±0.6	74.6±0.6	75.5±0.6
m-20	59.4±0.7	62.7±0.7	66.5±0.7	68.9±0.7	71.1±0.6	74.1±0.6	75.7±0.6	76.9±0.6	76.4±0.6	78.1±0.6	79.3±0.6	79.7±0.6	79.5±0.6
m-10	63.7±0.7	67.1±0.7	68.4±0.7	72.5±0.6	73.4±0.6	74.8±0.6	76.4±0.6	76.9±0.6	77.8±0.6	77.5±0.6	78.1±0.6	79.4±0.6	80.2±0.6
m	66.5±0.7	68.8±0.7	70.1±0.6	71.9±0.6	75.1±0.6	75.3±0.6	76.9±0.6	76.6±0.6	78.9±0.6	78.6±0.6	79.9±0.6	80.2±0.6	80.2±0.6
95% CL upper limit on cross-section times $BR^2(\tilde{\tau}^- \to \tau\tilde{\chi}_1^0)$ (fb)													
2	5120.5	6257.5	–	–	–	–	–	–	–	–	–	–	–
2.5	2127.4	2748.0	2701.6	3021.5	4413.7	5055.9	5707.0	8188.5	–	–	–	–	–
5	78.5	69.1	85.8	100.0	105.9	107.3	127.8	147.9	199.1	245.4	363.0	403.2	2964.7
10	52.6	49.5	44.2	39.2	33.7	35.2	35.2	34.9	39.6	48.0	56.0	81.4	474.3
20	50.3	42.5	42.8	40.3	40.8	36.9	36.7	39.0	37.2	34.8	37.5	42.3	234.9
$m/2$	51.4	51.6	46.6	45.7	42.0	44.3	41.9	42.8	44.7	48.6	53.3	61.4	255.8
m-20	56.0	53.8	56.3	48.8	48.0	47.6	45.7	47.9	54.2	57.7	61.2	78.7	328.4
m-10	63.6	62.8	55.7	49.7	46.1	48.3	49.1	48.5	52.1	58.7	70.0	91.8	355.7
m	67.4	64.4	53.7	49.8	53.7	52.1	51.3	53.7	57.1	65.8	77.3	92.4	345.2
expected upper limit on cross-section times $BR^2(\tilde{\tau}^- \to \tau\tilde{\chi}_1^0)$ (fb)													
2	5902.4	6188.3	–	–	–	–	–	–	–	–	–	–	–
2.5	1685.2	2437.1	2458.6	3328.8	4590.3	6352.0	6459.3	10109.3	–	–	–	–	–
5	86.6	87.9	94.9	105.0	112.6	119.6	141.2	159.2	192.6	264.5	350.6	585.9	3573.9
10	44.0	42.0	41.0	42.6	43.0	45.0	49.0	50.3	56.3	68.0	78.0	113.8	646.3
20	45.5	45.0	43.5	43.3	42.3	42.9	43.4	43.9	47.0	55.1	62.2	79.1	405.0
$m/2$	47.0	48.5	48.0	50.0	49.3	50.7	51.9	55.2	61.0	71.4	82.2	109.8	505.2
m-20	49.4	49.9	51.3	52.1	53.2	55.3	58.5	60.6	66.0	79.0	87.9	117.8	538.1
m-10	52.8	52.5	53.1	53.8	56.0	56.9	59.4	61.5	68.6	79.2	92.1	118.8	535.2
m	53.6	52.8	53.2	55.3	55.8	58.1	61.2	62.9	69.0	78.7	91.1	117.7	534.9
CL for consistency with SM (%)													
2	60.4	53.2	–	–	–	–	–	–	–	–	–	–	–
2.5	17.6	28.4	31.7	54.2	49.2	80.4	65.9	61.2	–	–	–	–	–
5	54.9	70.3	56.8	48.7	48.4	55.5	53.8	52.2	39.3	53.0	37.2	100.0	100.0
10	23.3	26.2	34.0	51.8	72.7	71.3	80.0	83.2	81.4	80.4	79.0	84.6	77.3
20	31.5	50.4	43.8	51.7	46.5	61.1	62.7	60.3	69.0	88.9	92.6	97.4	98.8
$m/2$	33.7	35.7	46.3	55.4	61.7	59.5	69.2	73.5	78.8	84.1	88.6	95.5	99.5
m-20	30.4	35.7	34.5	51.8	54.6	60.4	72.9	70.9	66.1	78.6	82.2	86.3	92.5
m-10	23.7	24.2	38.2	54.3	66.1	63.7	64.3	72.1	74.3	76.1	74.5	73.8	86.6
m	19.5	22.5	42.5	55.2	49.6	55.8	64.3	62.9	65.2	64.4	62.9	69.3	88.8

Table 6.3: Stau results summary table.

Δm	$m_{\tilde{\chi}_1^\pm}$ (GeV)									
(GeV)	50	60	70	80	85	90	94	99	102	103
General Selection Efficiency (%)										
3	1.7±0.2	1.5±0.2	1.4±0.2	0.8±0.1	0.4±0.1	0.4±0.1	0.3±0.1	0.1±0.0	0.0±0.0	0.0±0.0
5	11.2±0.5	10.4±0.5	10.2±0.5	9.1±0.5	7.3±0.4	6.8±0.4	6.0±0.4	5.6±0.4	4.8±0.3	4.4±0.3
10	32.6±0.7	34.2±0.8	33.5±0.7	32.4±0.7	31.0±0.7	32.5±0.7	31.2±0.7	29.3±0.7	29.5±0.7	29.7±0.7
20	52.7±0.8	53.7±0.8	54.8±0.8	54.8±0.8	55.4±0.8	55.0±0.8	55.2±0.8	53.4±0.8	54.6±0.8	55.4±0.8
$m/2$	57.5±0.8	63.9±0.8	69.5±0.7	75.7±0.7	74.9±0.7	76.6±0.7	77.2±0.7	78.0±0.7	78.4±0.7	77.9±0.7
m-20	62.2±0.8	71.9±0.7	75.8±0.7	79.2±0.6	82.4±0.6	82.9±0.6	84.6±0.6	87.2±0.5	88.5±0.5	88.8±0.5
m-10	68.9±0.7	73.4±0.7	79.2±0.6	82.2±0.6	84.3±0.6	87.8±0.5	89.0±0.5	90.2±0.5	90.4±0.5	90.3±0.5
m	72.2±0.7	77.2±0.7	80.4±0.6	85.2±0.6	87.3±0.5	89.2±0.5	89.7±0.5	89.6±0.5	90.5±0.5	91.1±0.5
95% CL upper limit on cross-section times $BR^2(\tilde{\chi}_1^\pm \to \ell^\pm \nu \tilde{\chi}_1^0)$ (fb)										
3	189.8	249.3	373.5	978.8	1168.0	1805.3	4181.5	10449.8	–	–
5	59.0	62.9	55.9	80.0	86.1	106.3	150.6	194.6	564.8	7644.4
10	29.8	23.5	21.8	24.1	23.7	27.7	36.1	46.3	87.4	1128.0
20	33.6	27.9	25.3	19.7	19.1	19.5	22.7	26.8	54.3	604.6
$m/2$	37.2	32.1	33.2	27.8	30.1	34.2	45.4	37.5	56.5	441.4
m-20	43.3	39.8	36.9	40.3	43.1	56.2	77.0	107.9	151.4	1046.3
m-10	50.5	45.4	45.4	47.6	56.7	68.2	98.4	155.3	248.1	1228.6
m	58.4	52.6	58.7	66.6	92.5	93.5	105.4	175.4	263.9	1184.4
expected upper limit on cross-section times $BR^2(\tilde{\chi}_1^\pm \to \ell^\pm \nu \tilde{\chi}_1^0)$ (fb)										
3	269.3	334.0	470.3	883.3	1364.1	2487.1	3961.3	12927.5	–	–
5	67.5	67.9	73.5	83.3	99.0	113.7	158.7	259.4	663.9	7666.5
10	36.4	33.5	32.5	32.5	33.0	35.8	43.0	60.2	116.7	1155.8
20	41.1	35.5	31.5	29.8	30.0	30.6	36.1	47.4	84.3	662.2
$m/2$	46.1	46.6	43.9	43.3	43.8	48.9	59.9	81.2	131.2	695.0
m-20	50.9	54.3	56.2	61.5	70.0	80.9	102.4	127.9	189.2	833.0
m-10	61.2	63.6	68.4	75.7	85.1	100.6	119.8	130.1	192.6	834.9
m	70.1	71.2	77.5	98.1	113.6	113.5	119.5	133.4	186.5	838.6
CL for consistency with SM (%)										
3	83.8	77.6	72.4	29.0	59.5	86.6	33.5	100.0	–	–
5	59.6	50.9	74.3	47.3	60.5	49.8	47.3	100.0	100.0	100.0
10	66.3	82.8	86.0	76.4	80.2	71.8	61.6	73.0	100.0	100.0
20	66.3	72.6	67.2	86.3	88.3	88.4	90.6	95.7	90.7	100.0
$m/2$	70.3	81.2	73.8	88.1	82.8	81.2	72.5	99.5	99.8	96.3
m-20	62.7	77.1	86.8	87.0	92.4	81.8	76.7	64.1	68.6	20.8
m-10	64.4	80.3	86.9	90.6	88.0	86.5	68.5	23.5	17.3	8.8
m	64.5	75.9	76.7	86.2	69.9	67.8	59.3	15.6	11.3	10.9

Table 6.4: Chargino (3-body decay) results summary table.

Δm	$m_{\tilde{\chi}_1^\pm}$ (GeV)								
(GeV)	50	60	70	80	85	90	94	99	102
General Selection Efficiency (%)									
2	5.3±0.4	3.9±0.3	2.6±0.3	1.5±0.2	1.0±0.2	0.7±0.1	0.4±0.1	0.2±0.1	0.1±0.0
3	16.2±0.6	15.9±0.6	14.3±0.6	12.6±0.5	11.7±0.5	10.5±0.5	9.3±0.5	8.1±0.4	7.6±0.4
4	26.5±0.8	27.4±0.7	24.6±0.7	24.3±0.7	23.9±0.7	22.5±0.7	20.9±0.6	20.0±0.6	20.0±0.6
5	35.6±0.8	35.2±0.8	33.8±0.8	33.8±0.7	33.8±0.7	33.1±0.7	31.8±0.7	30.9±0.7	31.0±0.7
10	58.1±0.9	59.6±0.8	59.1±0.8	58.5±0.8	57.6±0.8	56.3±0.8	55.5±0.8	55.1±0.8	55.1±0.8
20	0.0±0.0	76.1±0.7	76.8±0.7	76.2±0.7	75.7±0.7	75.4±0.7	75.3±0.7	75.5±0.7	75.2±0.7
$(m-15)/2$	0.0±0.0	77.6±0.7	81.4±0.6	84.1±0.6	84.9±0.6	85.2±0.6	85.8±0.6	87.2±0.5	88.1±0.5
m-35	68.5±0.8	78.6±0.7	83.3±0.6	85.9±0.6	87.2±0.5	88.3±0.5	89.1±0.5	90.3±0.5	90.6±0.5
95% CL upper limit on cross-section times $BR^2(\tilde{\chi}_1^\pm \to \ell^\pm \tilde{\nu})$ (fb)									
2	103.6	132.6	217.2	472.7	835.1	1958.5	3390.9	8231.3	–
3	41.7	41.1	42.0	52.7	63.9	73.4	88.1	134.9	350.4
4	26.0	24.5	29.1	25.6	28.8	29.4	36.1	52.3	129.4
5	20.2	19.5	19.7	21.3	22.7	24.6	34.1	34.5	84.1
10	29.3	24.2	20.2	17.1	16.2	17.0	21.2	25.6	48.5
20	–	30.2	27.4	23.5	25.3	19.9	19.5	21.2	40.1
$(m-15)/2$	–	33.1	34.9	35.9	45.2	47.9	70.9	78.8	64.7
m-35	65.1	42.0	45.3	65.6	73.0	69.3	77.3	155.8	272.6
expected upper limit on cross-section times $BR^2(\tilde{\chi}_1^\pm \to \ell^\pm \tilde{\nu})$ (fb)									
2	110.6	156.2	250.4	502.7	790.7	1718.2	3001.0	9903.8	–
3	49.0	47.6	50.3	56.5	61.9	74.8	105.7	173.7	400.6
4	34.6	33.2	34.4	32.4	34.3	38.5	51.0	72.9	149.8
5	30.5	28.6	28.2	27.5	28.0	29.6	37.0	53.1	105.1
10	35.7	29.7	26.3	23.5	23.3	24.1	28.4	36.8	71.4
20	–	53.8	44.7	38.5	34.9	33.1	37.4	45.5	72.3
$(m-15)/2$	–	59.1	61.6	64.0	68.6	77.2	85.6	89.0	116.7
m-35	98.9	66.1	77.8	90.2	98.9	97.5	100.4	100.5	135.9
CL for consistency with SM (%)									
2	46.7	66.5	60.5	49.1	35.6	25.8	32.0	100.0	–
3	61.3	60.6	66.3	54.1	37.8	43.6	75.4	100.0	100.0
4	76.7	76.5	64.7	68.7	63.6	77.0	81.4	100.0	100.0
5	85.7	83.9	83.4	72.3	68.3	65.3	54.8	86.2	100.0
10	66.0	66.6	72.9	78.0	81.6	81.2	76.4	83.5	92.2
20	–	95.4	91.9	90.9	79.0	91.7	97.6	99.6	99.6
$(m-15)/2$	–	96.4	94.8	94.8	88.1	90.7	67.2	57.7	96.1
m-35	86.3	91.1	94.6	79.5	78.9	82.9	72.8	7.5	0.9

Table 6.5: Chargino (2-body decay) results summary table.

m_{H^+} (GeV)											
50	55	60	65	70	75	80	85	90	94	99	103
General Selection Efficiency (%)											
68.8±0.7	70.1±0.6	71.9±0.6	75.1±0.6	75.3±0.6	76.9±0.6	76.6±0.6	78.9±0.6	78.6±0.6	79.9±0.6	80.2±0.6	80.2±0.6
95% CL upper limit on cross-section times $BR^2(\mathrm{H}^\pm \to \tau^\pm \nu_\tau)$ (fb)											
63.8	57.4	50.9	55.4	52.2	47.0	48.1	52.4	61.9	70.8	99.5	352.4
expected upper limit on cross-section times $BR^2(\mathrm{H}^\pm \to \tau^\pm \nu_\tau)$ (fb)											
53.0	53.5	54.4	57.3	57.4	59.7	62.9	68.1	78.1	88.9	116.9	538.8
CL for consistency with SM (%)											
23.8	34.9	50.5	48.1	54.4	71.3	74.8	75.1	72.2	68.2	62.2	87.3

Table 6.6: Charged Higgs results summary table.

6.4 Discussion of results

The points of lowest confidence level for consistency with the Standard Model in tables 6.1 to 6.6 occur in the Chargino (2-body decay) search at $m = 102$ GeV, $\Delta m = m - 35$ GeV (CL=0.9%), and in the smuon search at $m = 70$ GeV, $\Delta m = m - 10$ GeV (CL=3.0%). The study in section 5.8.3 shows that it is not unlikely for points with this level of consistency to occur. However, it is still important to examine the data at these points more closely.

Figure 6.9 shows the L_R distributions for data, background and signal in the chargino (2-body decay) search at $m = 102$ GeV, $\Delta m = m - 35$ GeV. Appendix B describes an alternative analysis which makes an optimised cut on the L_R distributions at each point in the m, Δm plane. At this point only the data with $\sqrt{s} > 206$ GeV contribute with the cuts being placed at $L_R = 0.86$ and $L_R = 0.61$ for the 207 and 208 GeV energy bins respectively. The number of events passing this cut is 19 in the data with 11.33 ± 0.35 expected.

Figure 6.10 shows the L_R distributions for the smuon search at $m = 60$ GeV and $\Delta m = 60$ GeV. Here the cut based analysis finds 48 events in the data with 40.1 ± 0.53 expected (the L_R cut ranges between 0.5 and 0.75 at the different $\sqrt{s}$ values). This is not a very large excess of events, but the figure shows that there is a particular excess in the region where the signal L_R distributions peaks. This demonstrates the extra discriminating power of this analysis over a simple event counting experiment.

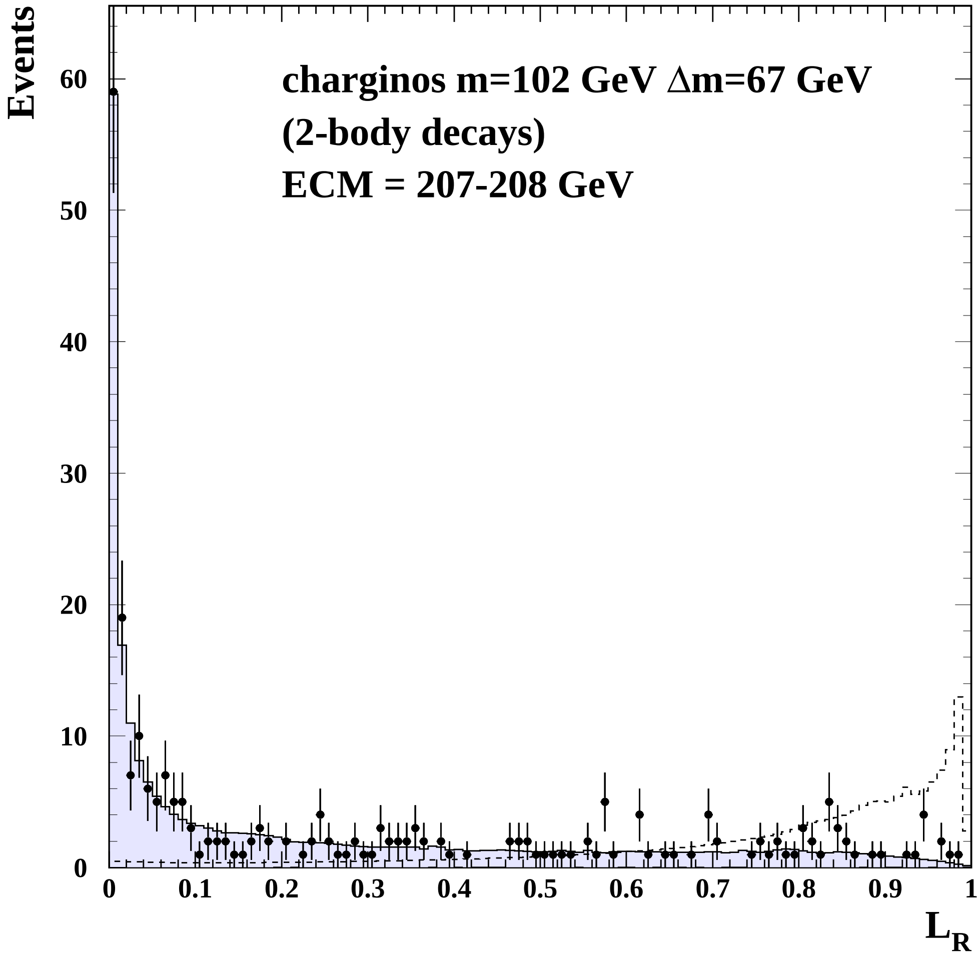

Figure 6.9: L_R distributions for charginos (2-body decays) at $m = 102$ GeV, $\Delta m = m - 35$ GeV, for data (points with error bars), background (filled histogram) and signal (dashed histogram, arbitrary normalisation).

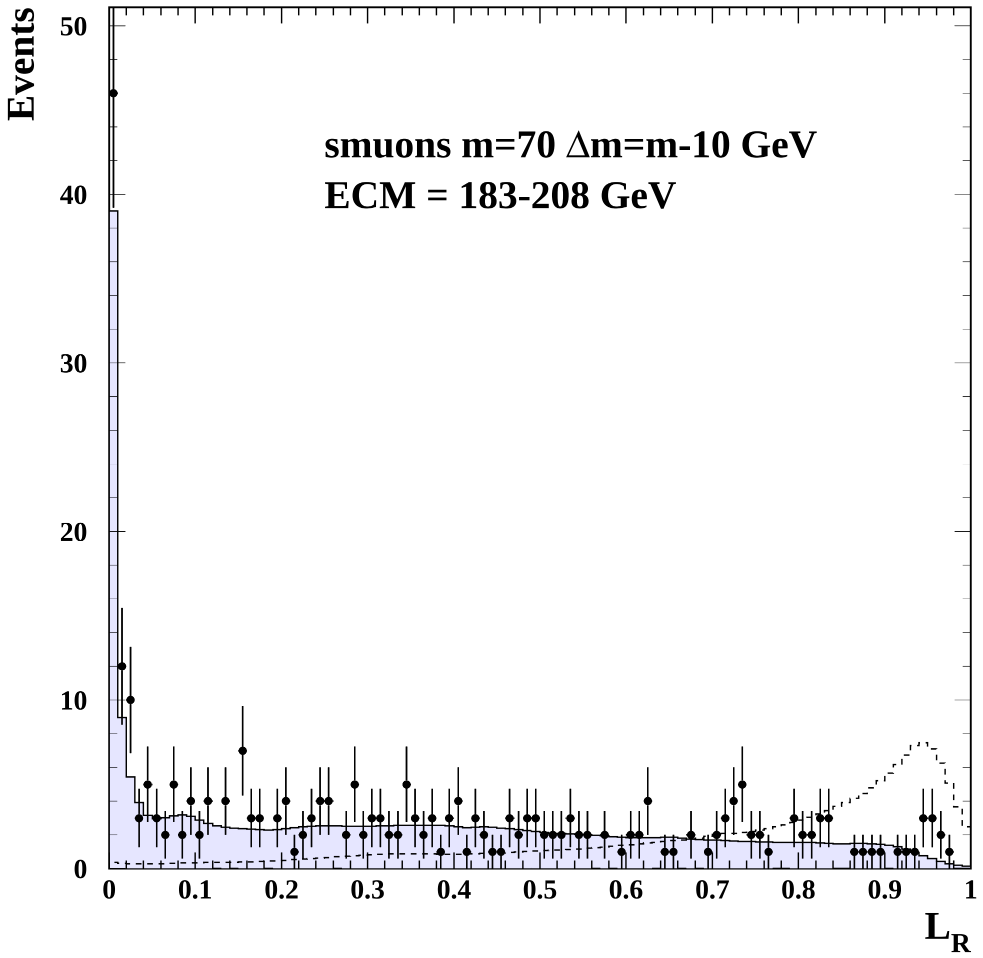

Figure 6.10: L_R distributions for smuons at $m = 70$ GeV, $\Delta m = m - 10$ GeV, for data (points with error bars), background (filled histogram) and signal (dashed histogram, arbitrary normalisation).

Chapter 7

Further Data-Standard Model Comparisons

This chapter contains some further tests of consistency between the data and the Standard Model expectation. These comparisons are inspired by possible new physics signals, but no attempt has been made here to generate signal Monte Carlo or set cross section limits. This is because there would be too many signal parameters to scan. However, the aim here is to look for signals which the main slepton search may not be sensitive to. If any such signals are present then some inconsistency should become apparent between the data and Standard Model expectation.

7.1 Unequal Mass Particle Production

The main search of chapter 5 is concerned with the pair production of new particles which have equal mass. This results in both new particles having equal energy, and thus the same Lorentz boost being given to the observed leptons. Hence the momentum distribution is the same for each lepton.

In the case that two particles with unequal mass are produced which then decay to leptons plus missing energy, the momentum spectrum of each lepton would be different. In general the lepton from the decay of the higher mass particle would have higher momentum. This situation could occur if, for example, $\tilde{e}_R^+\tilde{e}_L^-$ production took place. The left and right handed sleptons do not in general have the same mass. Production of left and right handed selectrons is potentially interesting because it takes place via a t-channel process with cross-section proportional to β/s. Close to the kinematic limit this cross-section can be larger than the right handed selectron pair production cross section which is suppressed proportional to β^3/s.

Since the search described in chapter 5 is carried out using signal Monte Carlo with equal mass selectrons, it will certainly have reduced sensitivity to the case where particles of unequal mass are produced. Indeed there are some mass combinations to which it would be completely blind [1].

In this section a search is carried out for lepton pairs with momenta falling in the kinematically allowed ranges for various different $\tilde{\mathrm{e}}_L$,$\tilde{\mathrm{e}}_R$ and $\tilde{\chi}^0$ mass combinations. Though primarily motivated by the possibility of unequal mass selectron production, the search is not limited to selectron candidate events. This is done to make the search as general as possible, but also motivated by new physics models which could produce acoplanar lepton pairs of unequal momentum, and arbitrary lepton flavour. An example[2] is $\mathrm{W}^+\mathrm{W}^-$ production where one W decays normally, and the other via $\mathrm{W}^\pm \rightarrow \tilde{\chi}_1^0\tilde{\chi}_1^\pm$ followed by $\tilde{\chi}_1^\pm \rightarrow \ell^\pm\tilde{\nu}$.

This search is not exhaustive, and in particular more attention could be focussed on the regions where the 3 masses are relatively close together. However it is intended

---

[1] It is possible at relatively small mass differences between the $\tilde{\mathrm{e}}_L/\tilde{\mathrm{e}}_R$ and $\tilde{\chi}^0$, for the allowed momentum ranges for the two observed leptons to be completely separated [39]

[2] This scenario would not result in the same lepton momentum ranges as from $\tilde{\mathrm{e}}_L\tilde{\mathrm{e}}_R$ production, however these ranges are still used for simplicity and because they provide a way of scanning the entire lepton momentum plane.

to make a broad survey of the data, to check for any obvious disagreements with the Monte Carlo to which the standard search may not have sensitivity.

7.1.1 Kinematics of Unequal Mass Particle Production

$\tilde{e}_L\tilde{e}_R$ pairs are produced by the t-channel process shown in figure 2.5b. The energy of the lower mass particle, E_{light}, is given by

$$E_{light} = \frac{m_{light}^2 - m_{heavy}^2 + s}{2\sqrt{s}} \tag{7.1}$$

where m_{light} and m_{heavy} are the masses of the masses of the unequal mass particles being produced, and $\sqrt{s}$ is the centre of mass energy. E_{heavy} is given by $E_{heavy} = \sqrt{s} - E_{light}$.

In the subsequent decay $\tilde{e} \to e\tilde{\chi}^0$, the maximum and minimum kinematically allowed energies of the electron are given by

$$E_e^{max} = \frac{m_{\tilde{e}}^2 - m_{\tilde{\chi}^0}^2}{2(E_{\tilde{e}} - p_{\tilde{e}})} \tag{7.2}$$

and

$$E_e^{min} = \frac{m_{\tilde{e}}^2 - m_{\tilde{\chi}^0}^2}{2(E_{\tilde{e}} + p_{\tilde{e}})} \tag{7.3}$$

where $E_{\tilde{e}}$ and $p_{\tilde{e}}$ are the energy and momentum of the parent selectron, and $m_{\tilde{\chi}^0}$ is the mass of the neutralino.

7.1.2 Mass scan

Equations 7.1-7.3 are used to find the allowed lepton momentum ranges for each mass combination, and these are then applied to the data. The masses are scanned in the relatively coarse step of 10 GeV. This is not ideal but necessary due to the large volume of parameter space involved. Results are shown in figures 7.1, 7.2, and 7.3, which show the Poisson probability at each mass point to observe greater than or equal to the number of events in the data, given the expectation from the Standard Model Monte Carlo. The lowest probability point occurs for leptons of arbitrary flavour at $m_{heavy} = 130$ GeV, $m_{light} = 60$ GeV, $m_{\tilde{\chi}^0} = 20$ GeV, where 242 events are observed with 197.3 expected from Standard Model sources (statistical only Poisson probability = 0.0007).

Due to the large number of mass combinations tested, it is expected that some large statistical fluctuations should occur. An ensemble of 1000 toy Standard Model-Monte Carlo experiments is used to test the probability of observing a fluctuation of a certain size. Of the 1000 toy experiments, 125 contained points with Poisson probability lower than the lowest probability observed in the data.

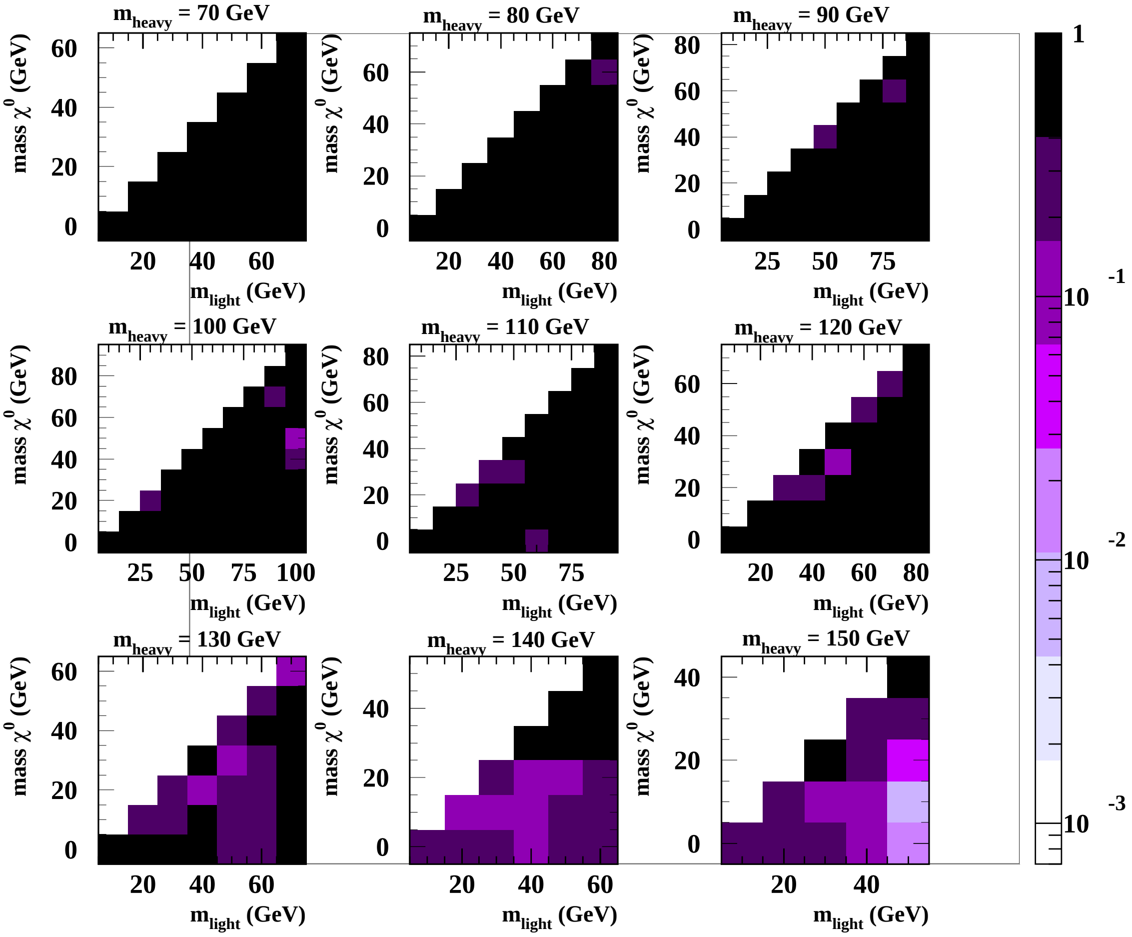

Figure 7.1: Probability to observe greater than or equal to the number of selectron candidate events in the data, for lepton momentum ranges kinematically allowed for various m_{heavy}, m_{light}, $m_{\tilde{\chi}^0}$ mass combinations.

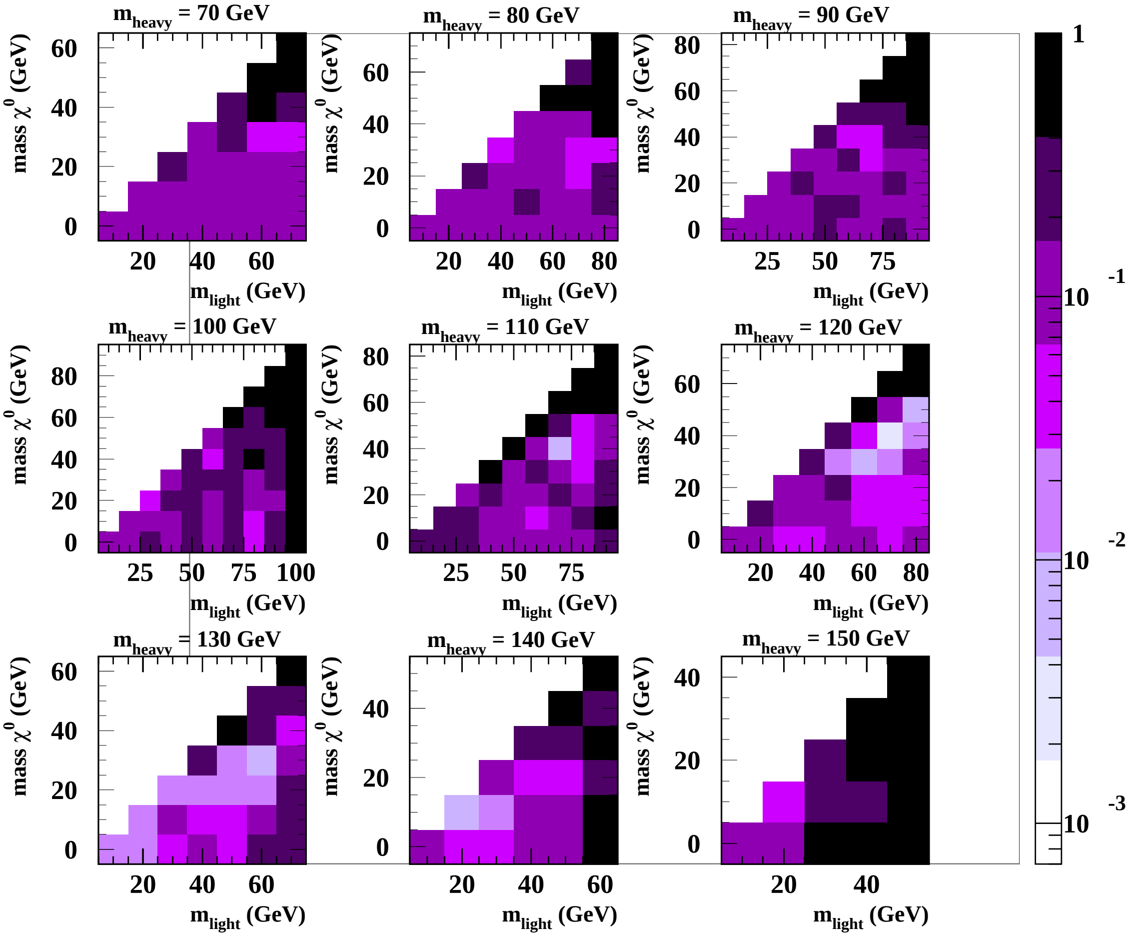

Figure 7.2: Probability to observe greater than or equal to the number of smuon candidate events in the data, for lepton momentum ranges kinematically allowed for various m_{heavy}, m_{light}, $m_{\tilde{\chi}^0}$ mass combinations.

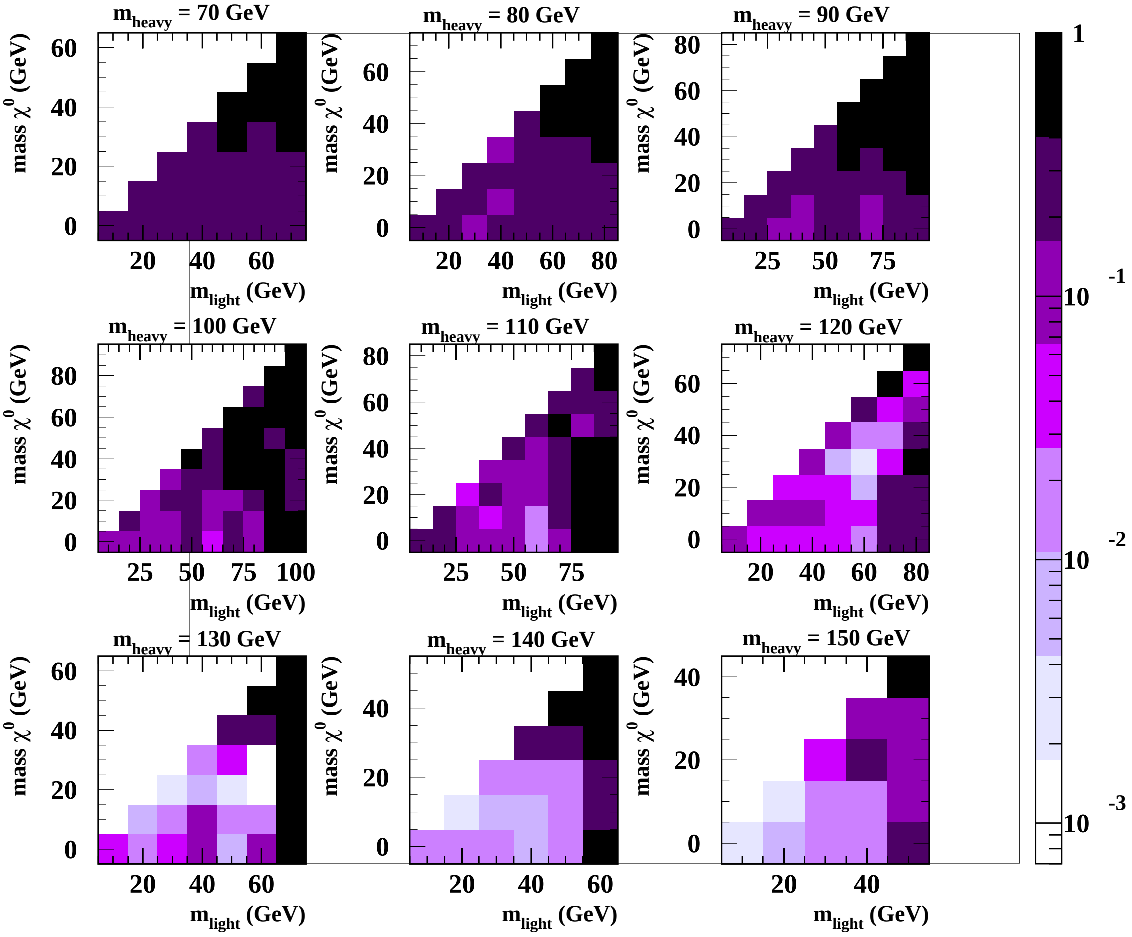

Figure 7.3: Probability to observe greater than or equal to the number of slepton candidate events of arbitrary lepton flavour in the data, for lepton momentum ranges kinematically allowed for various m_{heavy}, m_{light}, $m_{\tilde{\chi}^0}$ mass combinations.

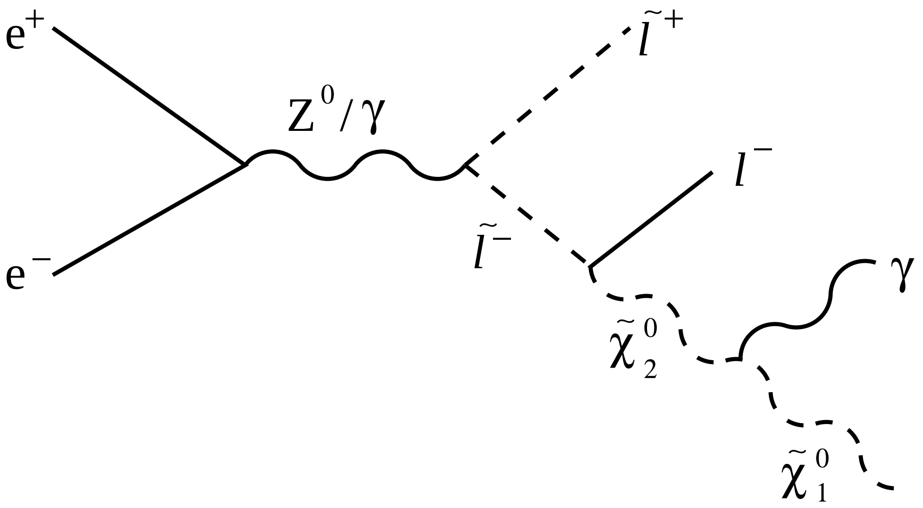

Figure 7.4: Smuon pair production followed by neutralino decay leading to an isolated photon.

7.2 Photons in Acoplanar Lepton Pairs

Acoplanar lepton pair events containing one or more photons are studied here. The main source of these photons is expected to be bremsstrahlung. A photon can be radiated from any of the charged particles by this process. Events containing photons could also provide sensitivity to a range of new physics processes beyond the Standard Model. An example is slepton pair production. If a pair of smuons was produced which then decayed by the process $\tilde{\mu} \rightarrow \mu\tilde{\chi}_2^0$, followed by the neutralino decay $\tilde{\chi}_2^0 \rightarrow \tilde{\chi}_1^0\gamma$, then photons would occur in the final state (see figure 7.4). Another possibility, favoured in GMSB SUSY models where the gravitino is the LSP, is slepton decay to lepton plus neutralino followed by neutralino decay to gravitino plus photon, $\tilde{\chi}_1^0 \rightarrow \tilde{G}\gamma$.

7.2.1 Selection of isolated photons

Isolated photons are characterised by clusters of energy in the electromagnetic calorimeter (ECAL) which are isolated from any charged tracks or other clusters. This selection of isolated photons is based on information provided from selection A (see section 4.1.1). ECAL clusters are required to be outside the isolation cones defined around the lepton candidates. It is further required that there is no charged track within a 20° cone around the ECAL cluster. In this study, only the two highest energy objects outside the lepton cone are considered, and hence the number of isolated photons identified never exceeds two.

Studies using Monte Carlo truth information show that clusters caused by small amounts of random noise in the ECAL could be falsely identified as photons. These noise clusters are eliminated by requiring that the raw energy of ECAL clusters must be greater than 250 MeV. Clusters with raw energy less than this are not considered. The raw energy deposited in the ECAL is not the same as the measured ECAL energy. The measured energy is obtained from the raw energy by applying a correction factor which depends on the amount of material in front of the ECAL. The noise clusters tend to have small raw energy.

Some photons are identified as converting photons which have undergone pair production in passing through the material of the detector. These account for 5% of the photons identified by this selection. The identification of low energy converting photons is also found to be unreliable, and so these are rejected for measured energy less than 500 MeV.

A further complication is that not all of the events in the sample have two identified lepton candidates (see section 4.1). In events containing a “rest of event” lepton candidate, there is a danger that the other activity in the event may be misidentified as a photon. To avoid this, the following extra requirements are made for events containing a “rest of event” lepton candidate:

- there must be at least one charged track outside the identified lepton cone

  OR

- if there are no charged tracks, the photon must not be too close to the beam ($|\cos\theta| > 0.95$) to avoid cases where the lepton track is not well identified, and the calorimeter cluster produced by the lepton is wrongly considered as an isolated photon.

Additional cuts for high energy photons ($E_{phot} > 25$ GeV) in events with "rest of event" lepton candidates:

- the photon must not be identified as a converting photon (to avoid mistaking a lepton track for a converting photon).
- the photon must be well separated from the beam ($|\cos\theta| > 0.88$).

7.2.2 Random occupancy background

The random occupancy background described in section 4.4 gives rise to a significant number of isolated ECAL clusters (0.9% of randomly triggered beam crossings have at least 1 isolated ECAL cluster which passes the raw energy cut described in section 7.2.1). The majority of these clusters are very low energy and at small angles from the beam. This allows a cut to be made on energy and angle which eliminates 40% of the photons found in the random trigger events. Figure 7.5 shows the distribution in energy and angle of the random trigger photons, and also a graphical representation of the cut. Details of the cut are as follows:

- clusters with $|\cos\theta| > 0.95$ **AND** $E_{clus} < 1$ GeV are rejected.

Table 7.1 shows the number of photons found in the random trigger events and in the acoplanar lepton pair candidate events, both before and after the cut is made.

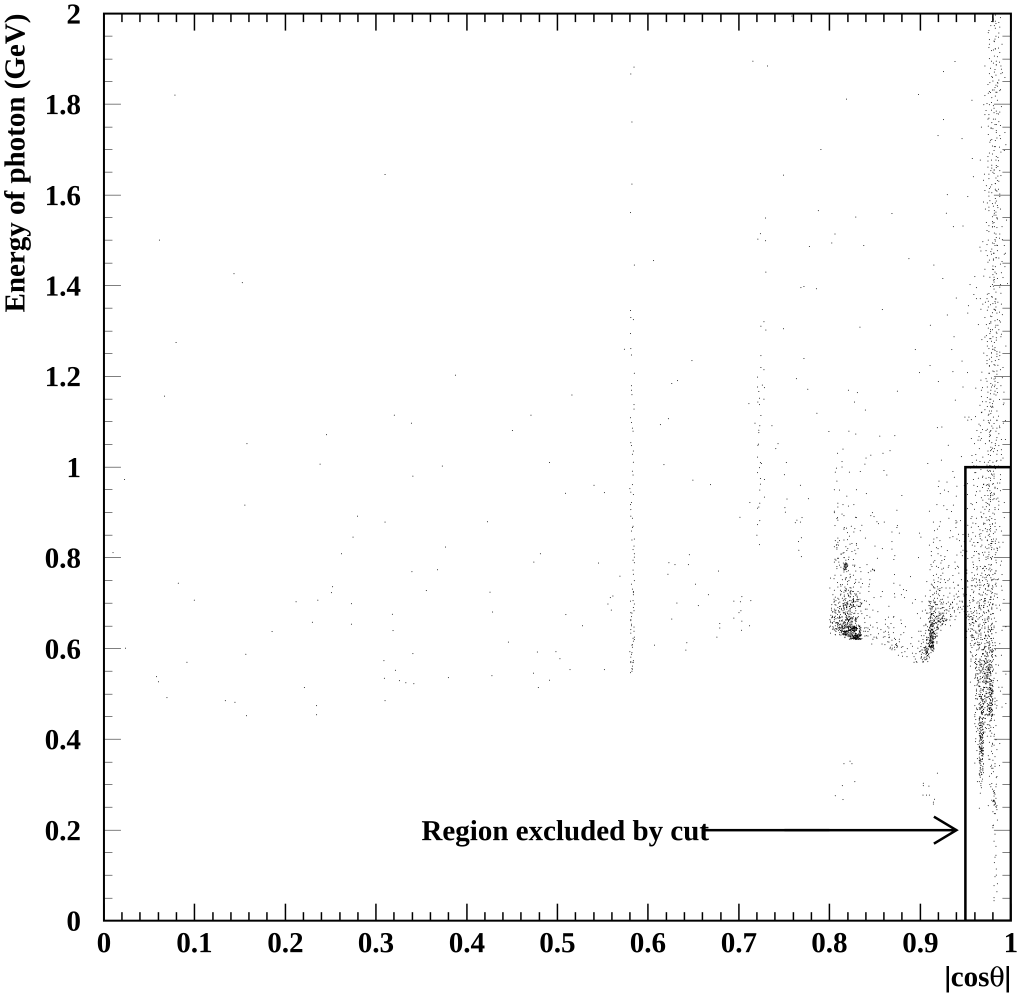

Figure 7.5: The distribution in energy and angle of isolated photons found in the random trigger events. The cut to reduce the effect of this background is shown graphically. (The variation of the lowest energies observed with angle is caused by the correction made to photon energy due to material in front of the detector.)

number of photons	0	1	2
Random triggers (no cut)	1701535	14948	308
Random triggers (with cut)	1707774	8895	122
Data acoplanar lepton candidates (no cut)	1026	128	7
Data acoplanar lepton candidates (with cut)	1029	126	6
MC acoplanar leptons (no cut)	1039.3±2.8	113.5±1.0	6.1±0.2
MC acoplanar lepton candidates (with cut)	1043.8±2.8	109.5±0.9	5.5±0.2

Table 7.1: Numbers of isolated photons found in random trigger events, and in acoplanar lepton pair candidate events, before and after cut is made to reduce background due to random occupancy of the detector.

After this cut, approximately 0.5% of events are expected to gain an isolated ECAL cluster due to random occupancy of the detector.

7.2.3 Performance of isolated photon selection

The efficiency and purity of this selection of isolated photons has been studied using the Standard Model Monte Carlo. Figures 7.6a-b show the purity of the photons selected as a function of photon energy. Here a selected photon is defined as a 'success' if it corresponds to a photon generated by the Monte Carlo which originated close to the interaction point ($x_0, y_0 < 1$ cm, $z_0 < 2.5$ cm). Figure 7.6a shows that photons are selected with good purity down to energies of about 500 MeV. The overall purity of the photons selected from this Monte Carlo is 84.2 ± 0.3%.

Figure 7.6b shows the efficiency to select photons as a function of photon energy. Here the efficiency is defined for photons originating close the the interaction point (as above), with $E_{phot} > 0.5$ GeV, and with $|\cos\theta| < 0.95$. The overall efficiency to select these photons is 87.6 ± 0.3%.

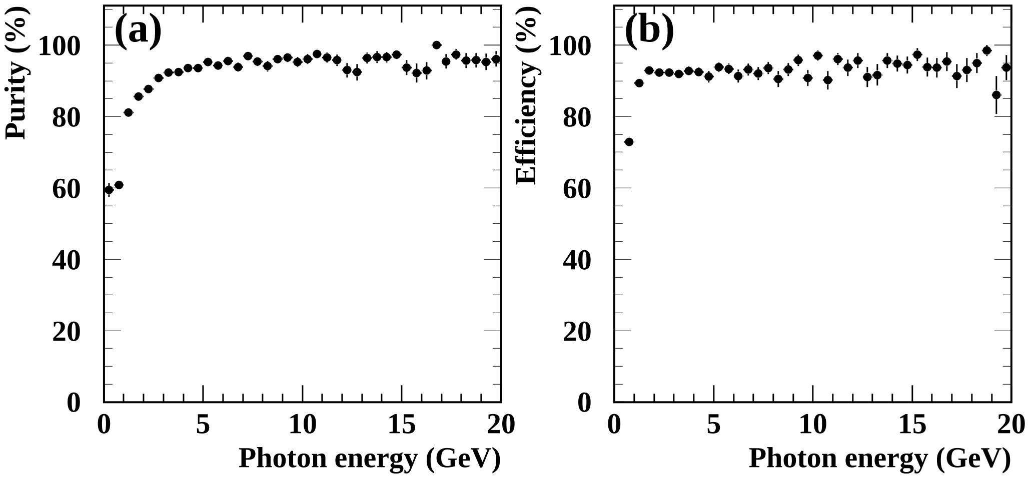

Figure 7.6: (a) purity of photon sample. (b) efficiency to select photons.

7.2.4 Isolated photon distributions

Distributions of number of photons per event, photon energy, polar angle, and dilepton type of event are shown in figure 7.7. No significant deviations from the Standard Model expectation are observed.

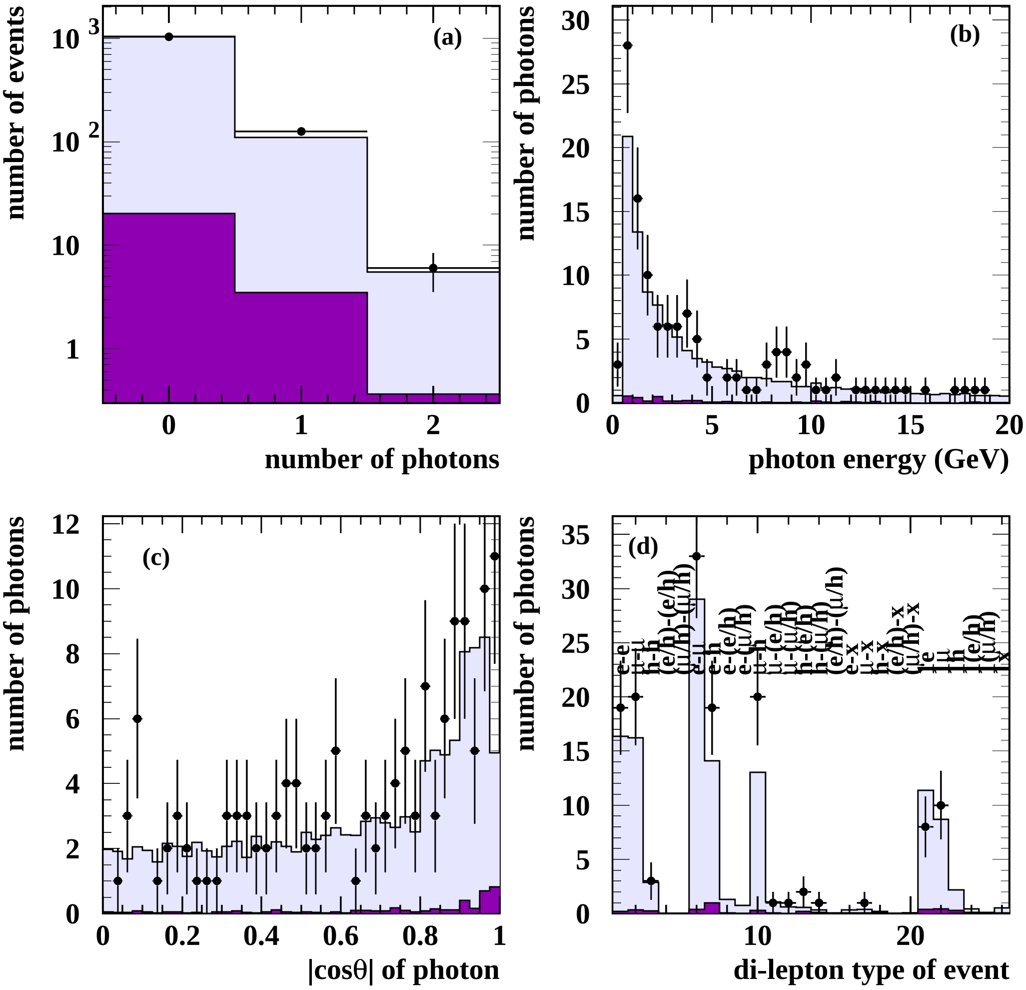

Figure 7.7: Properties of isolated photons in acoplanar lepton pair events. (a) Number of photons (b) Energy of photons (c) $|\cos\theta|$ of photons (d) Dilepton type of event containing photon.

Chapter 8

Summary and Conclusions

A selection of events containing two charged leptons and significant missing transverse momentum has been carried out using a total data sample of 680.4 pb^{-1} collected at e^+e^- centre of mass energies between 183 and 208 GeV. The observed numbers of events are consistent with the expectation from Standard Model processes, which come mostly from W^+W^- production where both W particles decay leptonically.

These events have been used to carry out a search for the pair production of sleptons, leptonically decaying charginos and charged Higgs particles. Cross section limits have been calculated at 95% confidence level, for a range of new particle masses up to 103 GeV. Confidence levels for consistency with the Standard Model have also been computed. No evidence for new phenomena is apparent.

An attempt has also been made to check the consistency of the data with the Standard Model with respect to processes which may produce acoplanar lepton pair events with unequal momentum distributions for the two leptons, and also processes leading to acoplanar lepton pair events plus isolated photons. Again no evidence for new phenomena is apparent.

The results presented in this thesis will be submitted for publication by OPAL. Preliminary results from this analysis prepared by the author have already been documented by OPAL in physics notes containing searches updates for 1999 and 2000 data taking [40, 41]. This data has also been combined with results from other decay channels in searches for charged Higgs particles [42], and searches for sleptons with arbitrary lifetime [43]. The preliminary OPAL slepton search results have also been combined with the other three LEP experiments [44].

Appendix A

Setting Limits Using Extended Maximum Likelihood Technique

This appendix recaps the method used to set an upper limit at 95% confidence level on the signal cross section times branching ratio squared. This description is included for the convenience of the reader and follows closely the description in [35].

The upper limit, σ_{95} , is found by forming a likelihood, $L(\sigma_s)$, for the distribution of L_R values seen in the data to be consitent with the expectation from the Standard Model plus a signal with cross-section $\sigma.BR^2 = \sigma_{95}$. σ_{95} is the value of σ_s below which 95% of the area under the likelihood function (probability) lies (see figure A.1).

A.1 The Likelihood Function

The Likelihood Function is the likelihood of the observed L_R values being consistent with expectation as a function of σ_s.

Extended maximum likelihood combines standard maximum likelihood with the Poisson probability of observing N candidate events when ν are expected:

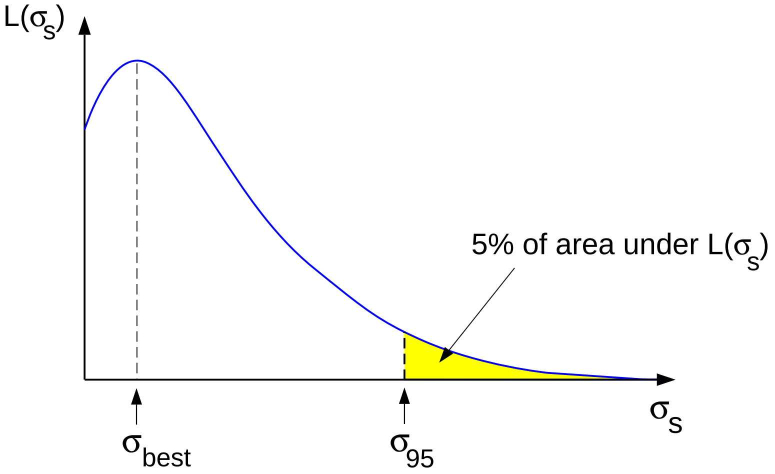

Figure A.1: Definition of σ_{95} in terms of likelihood function (from [35]).

$$L = \frac{e^{-\nu}\nu^N}{N!}\prod_{i=1}^{N} P(L_{R_i}; B, S), \tag{A.1}$$

where $P(L_{R_i}; B, S)$ is the probability of event i having $L_R = L_{R_i}$, given L_R distributions B and S for background and signal.

Dropping the constant $N!$, this can be re-written:

$$\ln L = -\nu + N\ln\nu + \sum_{i=1}^{N} \ln P(L_{R_i}; B, S) \tag{A.2}$$

$$\ln L = -\nu + \sum_{i=1}^{N} \ln[Q(L_{R_i}; B, S)] \tag{A.3}$$

where Q is identical to P but normalized to ν instead of 1 ($Q = \nu P$).

The dependence on σ_s comes in through the expected number of events, ν, and the relative normalisations of B and S. The expected number of candidates ν is given by:

$$\nu = \mu_B + \epsilon\mathcal{L}\omega\sigma_s, \tag{A.4}$$

where μ_B is the expected number of Standard Model events with non-zero L_R passing the general selection (similarly, N is the number of data candidates with $L_R \neq 0$ [1]), ϵ is the signal selection efficiency of the general selection, $\mathcal{L}$ is the experimental luminosity and ω is a weight factor which takes into account that the expected production cross-section varies with $\sqrt{s}$, but the limit on the observed cross-section is quoted at $\sqrt{s} = 208$ GeV.

$$\omega_i = \frac{\sigma_i}{\sigma_{208}}, \tag{A.5}$$

where σ_{208} is the expected cross-section for $\sqrt{s} = 208$ GeV and σ_i is the expected cross-section for the i^{th} value of $\sqrt{s}$.

For scalar particles, for example sleptons, we assume that the expected cross-section varies as β^3/s. For spin $\frac{1}{2}$ particles, for example charginos, we assume that the expected cross-section varies as β/s.

The function Q is the probability of event i having $L_R = L_{R_i}$, given L_R distributions B and S for background and signal, normalized to ν. This is given by:

$$Q = \mu_B B(L_{R_i}) + \epsilon\mathcal{L}\omega\sigma_s S(L_{R_i}), \tag{A.6}$$

where the functions B and S, formed using background and signal Monte Carlo respectively, are normalized to 1.

Hence the likelihood function is given by:

$$\ln L(\sigma_s) = -(\mu_B + \epsilon\mathcal{L}\omega\sigma_s) + \sum_{i=1}^{N} \ln[\mu_B B(L_{R_i}) + \epsilon\mathcal{L}\omega\sigma_s S(L_{R_i})]. \tag{A.7}$$

---

[1] For simplicity, only candidate events with $L_R \neq 0$ are considered in the calculation, because $S(L_R = 0) = 0$, and therefore, from equation A.7, the inclusion of events with $L_R = 0$ affects only the normalisation of L(σ_s) and does not therefore affect the value of σ_{95}.

A.2 Limit Calculation

For data at a single centre-of-mass energy, the upper limit on $\sigma.BR^2$ at 95% confidence level is the value of σ_{95} which satisfies:

$$0.95 = \frac{\int_0^{\sigma_{95}} L(\sigma_s)\mathrm{d}\sigma_s}{\int_0^{\infty} L(\sigma_s)\mathrm{d}\sigma_s}. \tag{A.8}$$

The generalization to N_{ECM} values of $\sqrt{s}$ is:

$$0.95 = \frac{\int_0^{\sigma_{95}^{208}} \prod_{i=1}^{N_{ECM}} L_i(\sigma_s^{208})\mathrm{d}\sigma_s^{208}}{\int_0^{\infty} \prod_{i=1}^{N_{ECM}} L_i(\sigma_s^{208})\mathrm{d}\sigma_s^{208}}. \tag{A.9}$$

where σ_s^{208} is the cross-section at $\sqrt{s} = 208$ GeV .

Appendix B

Cut-Based Results

A cut-based analysis can be used to compare data with expected Standard Model background, as an alternative to the extended maximum likelihood technique used in chapter 5. Here a cut is applied to the L_R distributions for signal, background and data. The number of data candidates, expected background and signal selection efficiency can then be found simply by counting events which pass the cut. These can then be used to check the consistency between data and background, or as inputs to calculate cross-section limits.

The value of the cut is optimised at each value of m and Δm where signal Monte Carlo has been generated to give the maximum sensitivity to a signal. This is done by scanning the cut value, L_{cut}, between 0 and 1 and calculating the expected cross-section limit at 95% confidence level for each L_{cut}. The value of L_{cut} which gives the minimum expected limit is used. The cut values on the grid points are then parameterised using a 2-dimensional function, to allow the optimum value of L_{cut} at intermediate m and Δm values to be found.

This cut-based method of setting limits was found in [35] to be as much as 20% less sensitive, depending on m and Δm , than the extended maximum likelihood method. However, these results are presented here because they provide a useful cross-check of the extended maximum likelihood technique, and because they allow a direct comparison between data and background. Also they are used as inputs to combine this analysis with other experiments or other analyses.

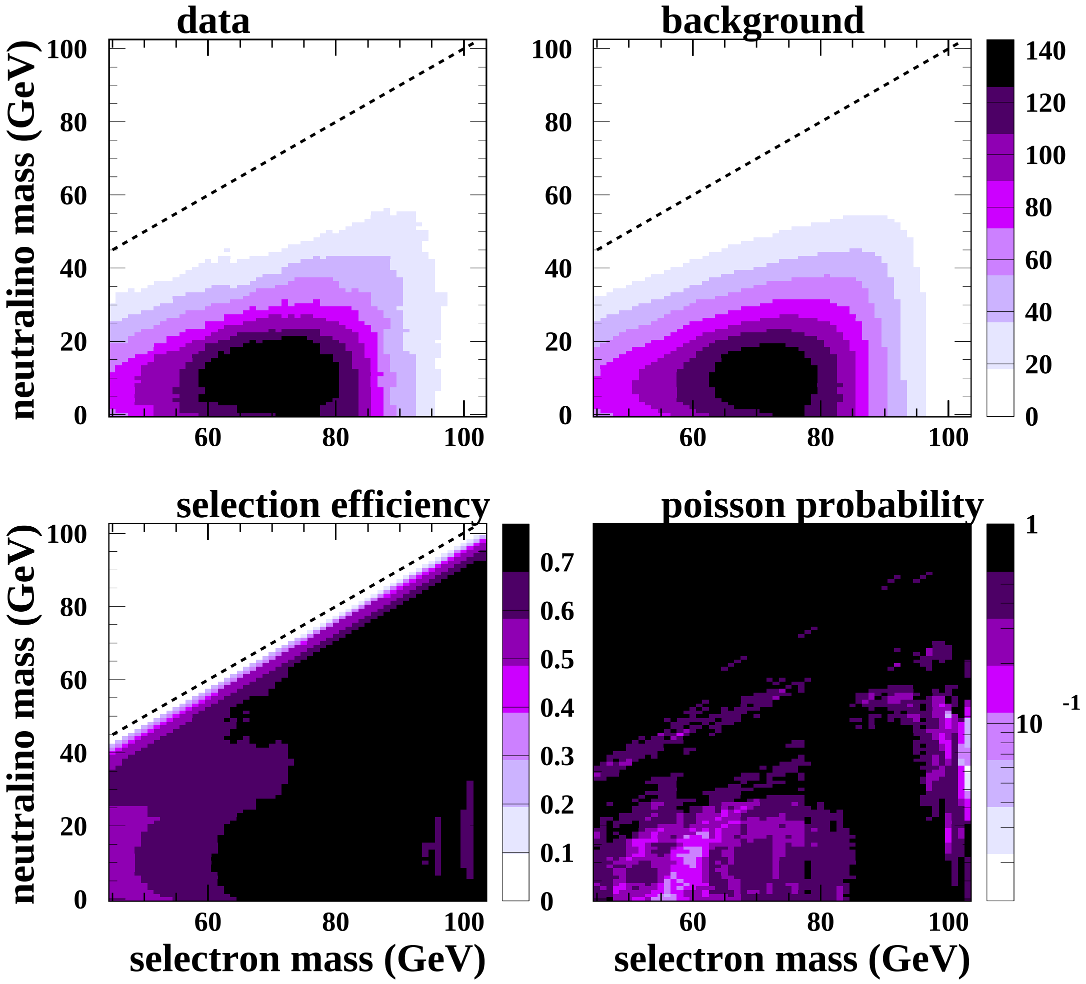

Figure B.1: Cut-based results from the search for $\tilde{e}^+\tilde{e}^-$ production, showing number of data candidates, expected Standard Model background, signal selection efficiency and Poisson probability to observe greater than or equal to the number of data candidates. These plots combine data taken from 183-208 GeV.

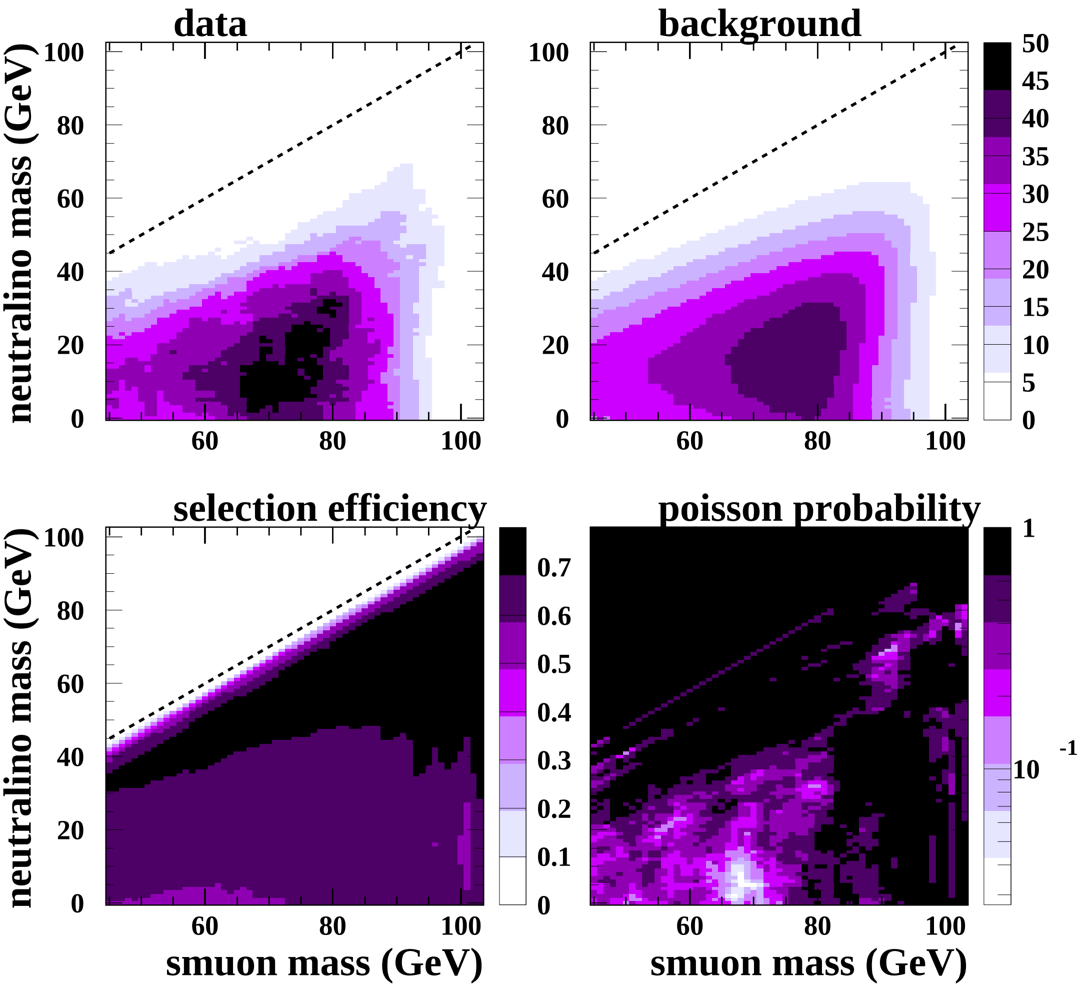

Figure B.2: Cut-based results from the search for $\tilde{\mu}^+\tilde{\mu}^-$ production, showing number of data candidates, expected Standard Model background, signal selection efficiency and Poisson probability to observe greater than or equal to the number of data candidates. These plots combine data taken from 183-208 GeV.

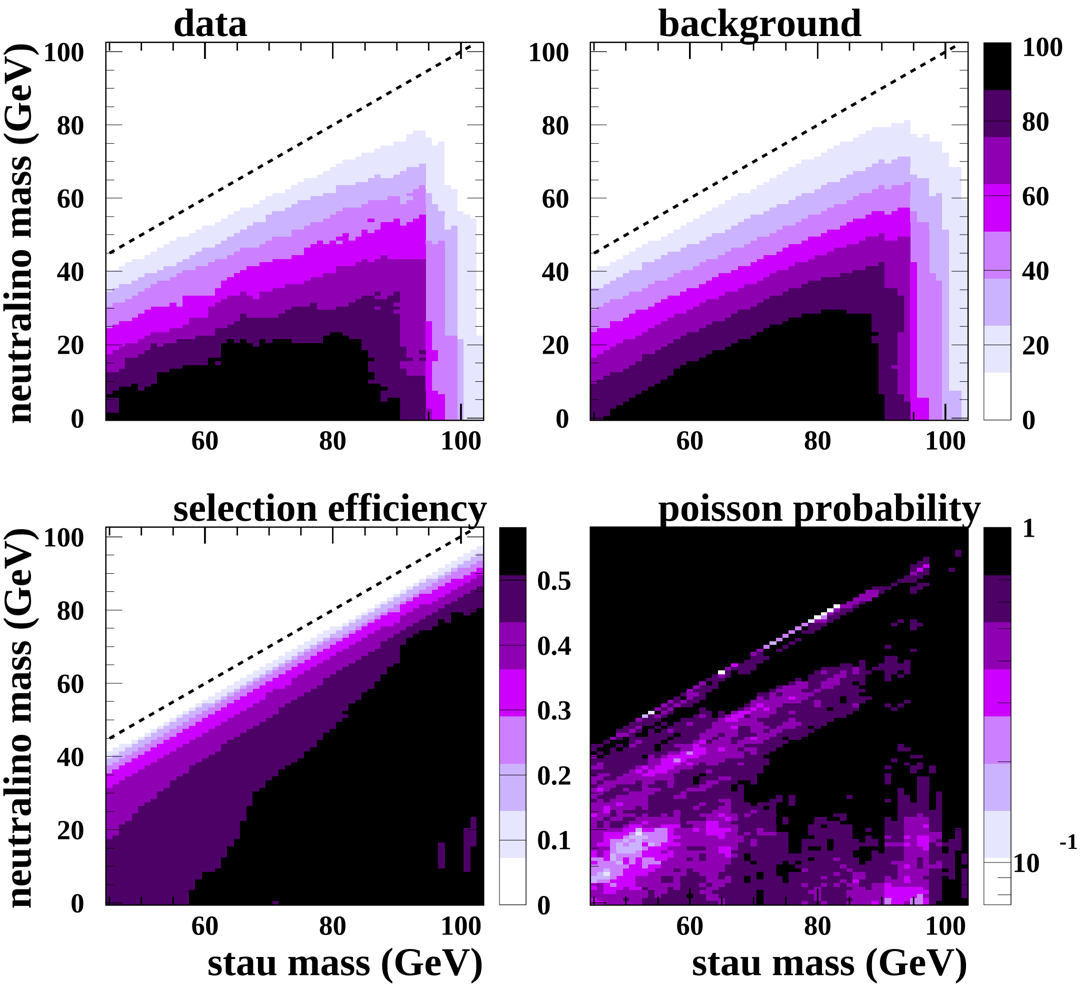

Figure B.3: Cut-based results from the search for $\tilde{\tau}^+\tilde{\tau}^-$ production, showing number of data candidates, expected Standard Model background, signal selection efficiency and Poisson probability to observe greater than or equal to the number of data candidates. These plots combine data taken from 183-208 GeV.

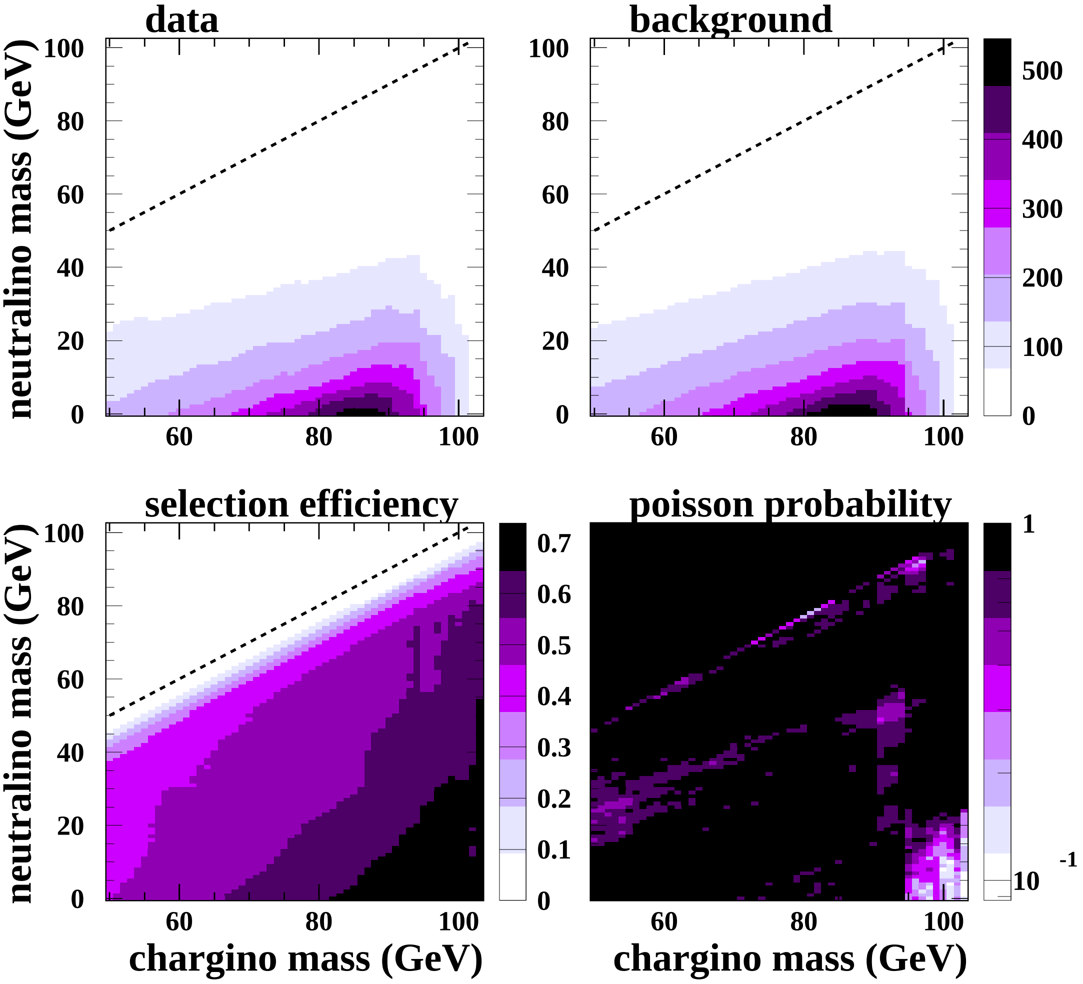

Figure B.4: Cut-based results from the search for $\tilde{\chi}_1^+\tilde{\chi}_1^-$ (3-body decays) production, showing number of data candidates, expected Standard Model background, signal selection efficiency and Poisson probability to observe greater than or equal to the number of data candidates. These plots combine data taken from 183-208 GeV.

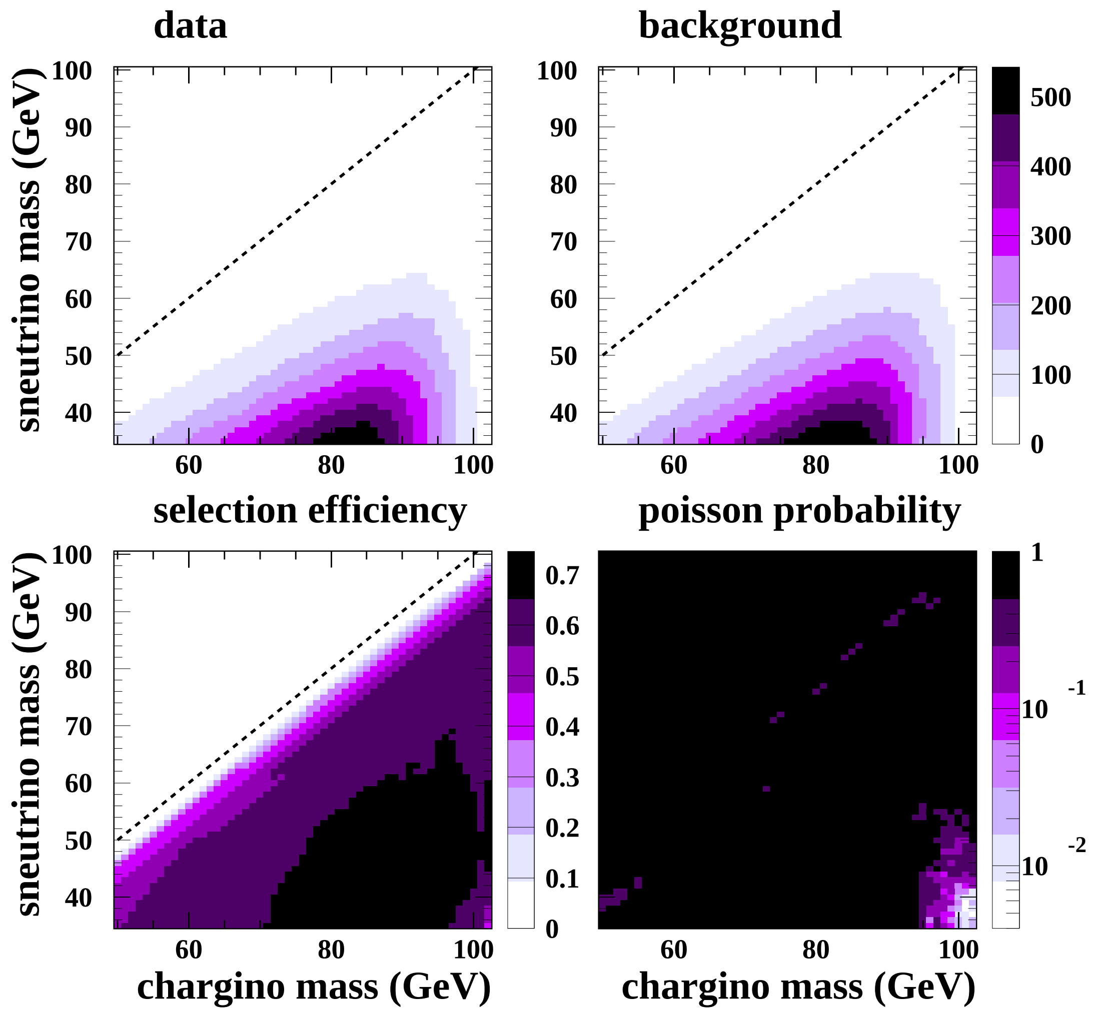

Figure B.5: Cut-based results from the search for $\tilde{\chi}_1^+\tilde{\chi}_1^-$ (2-body decays) production, showing number of data candidates, expected Standard Model background, signal selection efficiency and Poisson probability to observe greater than or equal to the number of data candidates. These plots combine data taken from 183-208 GeV.

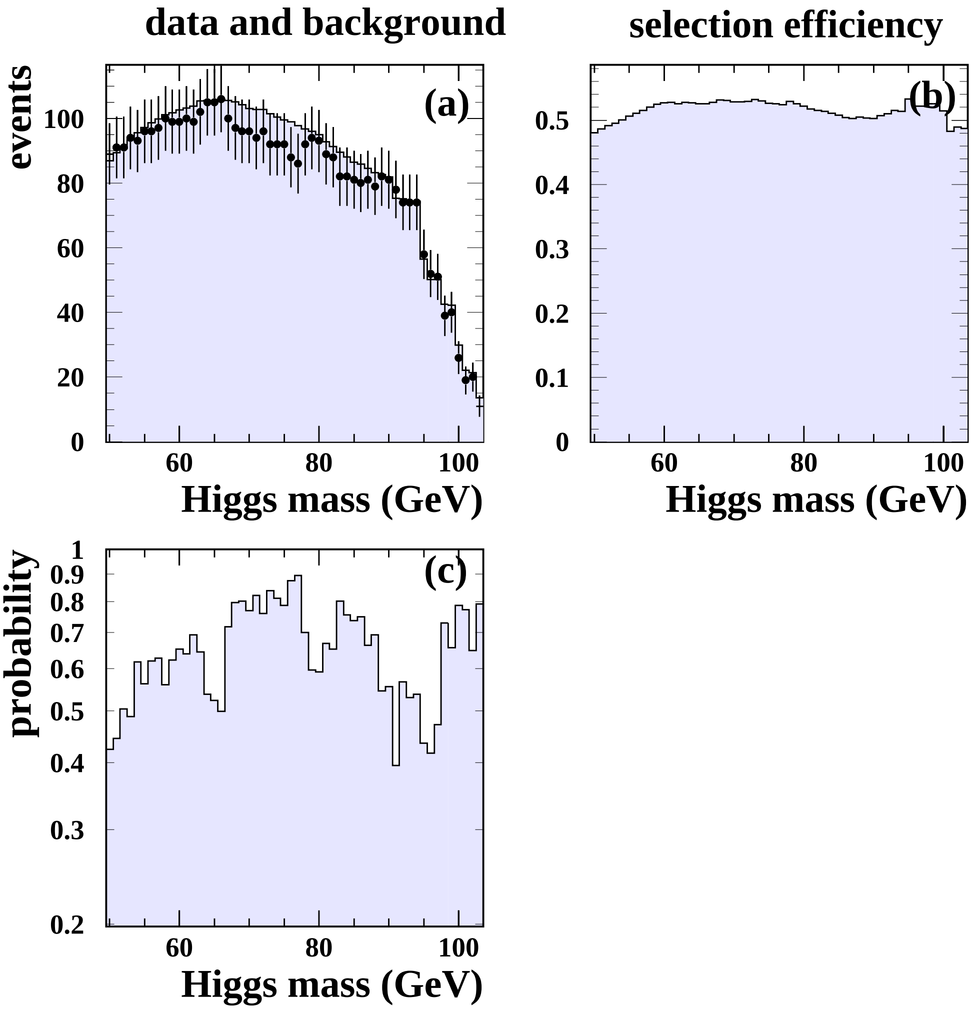

Figure B.6: Cut-based results from the search for $H^\pm$ production production, showing (a) number of data candidates (points with error bars) and expected Standard Model background (shaded histogram), (b) signal selection efficiency and (c) Poisson probability to observe greater than or equal to the number of data candidates. These plots combine data taken from 183-208 GeV.

Appendix C

Sleptons with Lifetime

The search for sleptons presented in this thesis is designed to be sensitive to sleptons with zero lifetime, which decay at the interaction point. However, in GMSB SUSY models the slepton can have non-zero lifetime (see section 2.5.4). The acoplanar lepton analysis can be applied to the zero and very-short lifetime range and other analyses are developed to cover intermediate and long lifetimes (see [43] for a full description). In GMSB SUSY the essentially massless gravitino is the LSP. This simplifies the search since the only parameters to be scanned are now the slepton mass and the slepton lifetime.

Four separate analyses are used which are described below. Their efficiencies for different slepton mass/lifetime combinations are evaluated using slepton Monte Carlo based on the 4-vectors used by the acoplanar lepton analysis, but with the appropriate slepton lifetime information inserted into GOPAL. The exclusive and overlap efficiencies for each analysis in the stau search are shown in figure C.1.

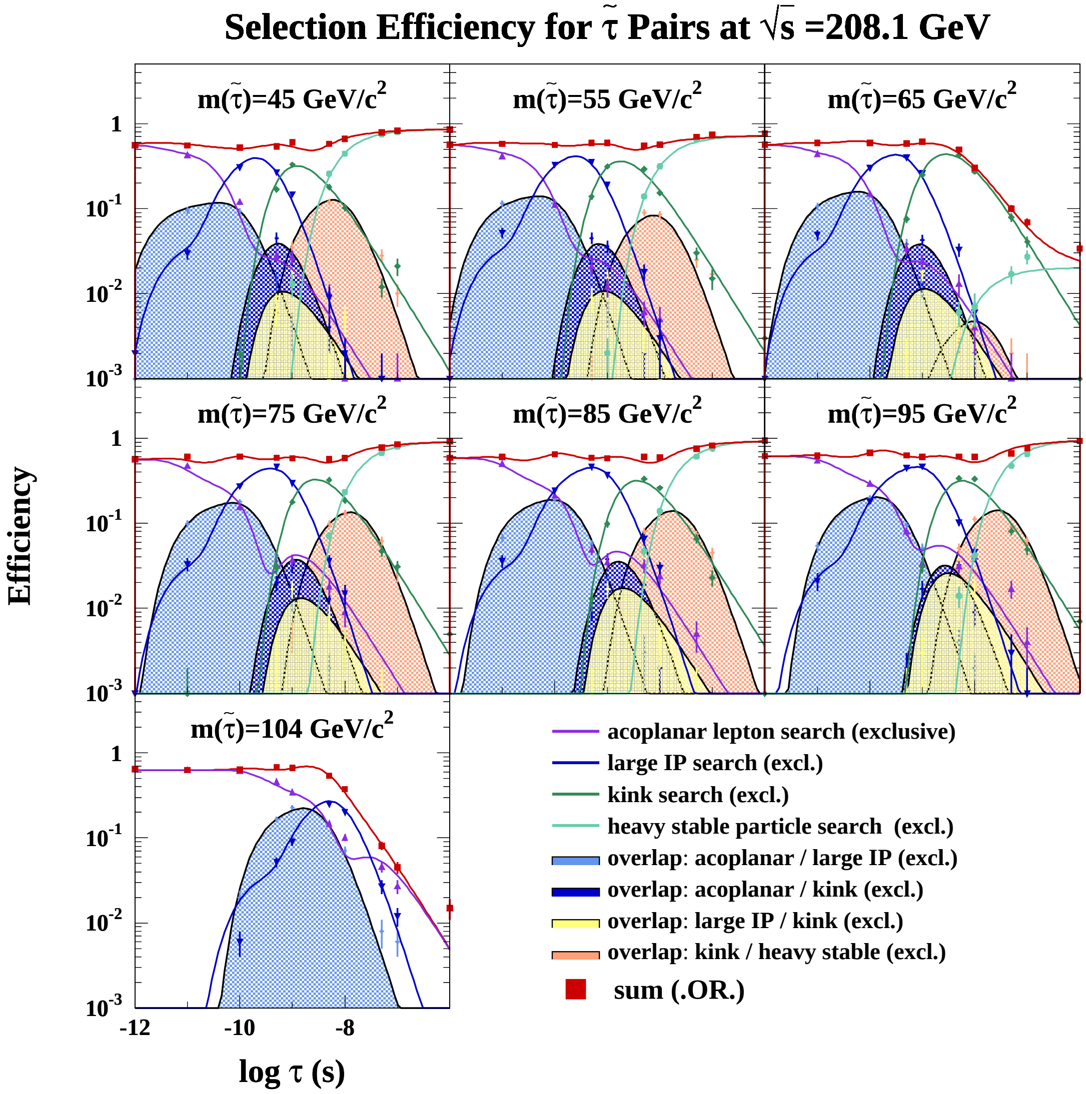

Figure C.1: Efficiency to select GMSB stau pairs as a function of stau lifetime for the different lifetime selections (from [43]).

C.1 Acoplanar lepton analysis

The acoplanar lepton analysis used is identical to that described in this thesis. Results from the cut-based analysis described in appendix B are used for ease of combination with the other analyses. The selection efficiency is found to remain high up to lifetimes of about 10^{-11} s, and to begin dropping off around 10^{-10} s. This can be understood from the requirement that particle tracks used in this analysis must point to within 2 cm of the interaction point. The mean radius of a particle produced at $\sqrt{s} = 208$ GeV with $m = 55$ GeV and lifetime $\tau = 10^{-10}$ s is $\beta c \gamma \tau = 5$ cm.

At the highest slepton mass values, close to the kinematic limit, the efficiency of the acoplanar lepton analysis extends to much higher values of τ. This is because the high mass slepton is produced with lower momentum and travels with speed considerably less that c (and $\gamma \approx 1$). Hence the distance travelled from the interaction point before decay is much less.

C.2 Other analyses

The three other analyses used to search for sleptons with intermediate lifetime are the large impact parameter search, the kinked tracks search and the heavy stable charged particle search.

The large impact parameter search looks for events where both leptons have decay vertices significantly displaced from the interaction point, but otherwise good quality tracks.

The kinked tracks search looks for events where one or both lepton tracks display a “kink” produced by the decay of the primary particle. Such tracks would be rejected by normal track selection criteria. This selection is sensitive to events where one or both of the sleptons decay within the central jet chamber.

The heavy stable charged particle search looks for events with two particle tracks originating from the interaction point, and no missing transverse energy. The tracks are required to have anomalous dE/dx values, consistent with a heavy charged particle. This analysis is sensitive to particles which decay outside the detector volume.

C.3 Results

The results from these analyses have been combined to cover all slepton lifetimes. No evidence for any excess of candidates over the Standard Model expectation was found, and limits on the production cross-section have been set at 95% confidence level (shown in figure C.2). The results for the acoplanar lepton analysis were prepared by the author, but not the other analyses or the combination.

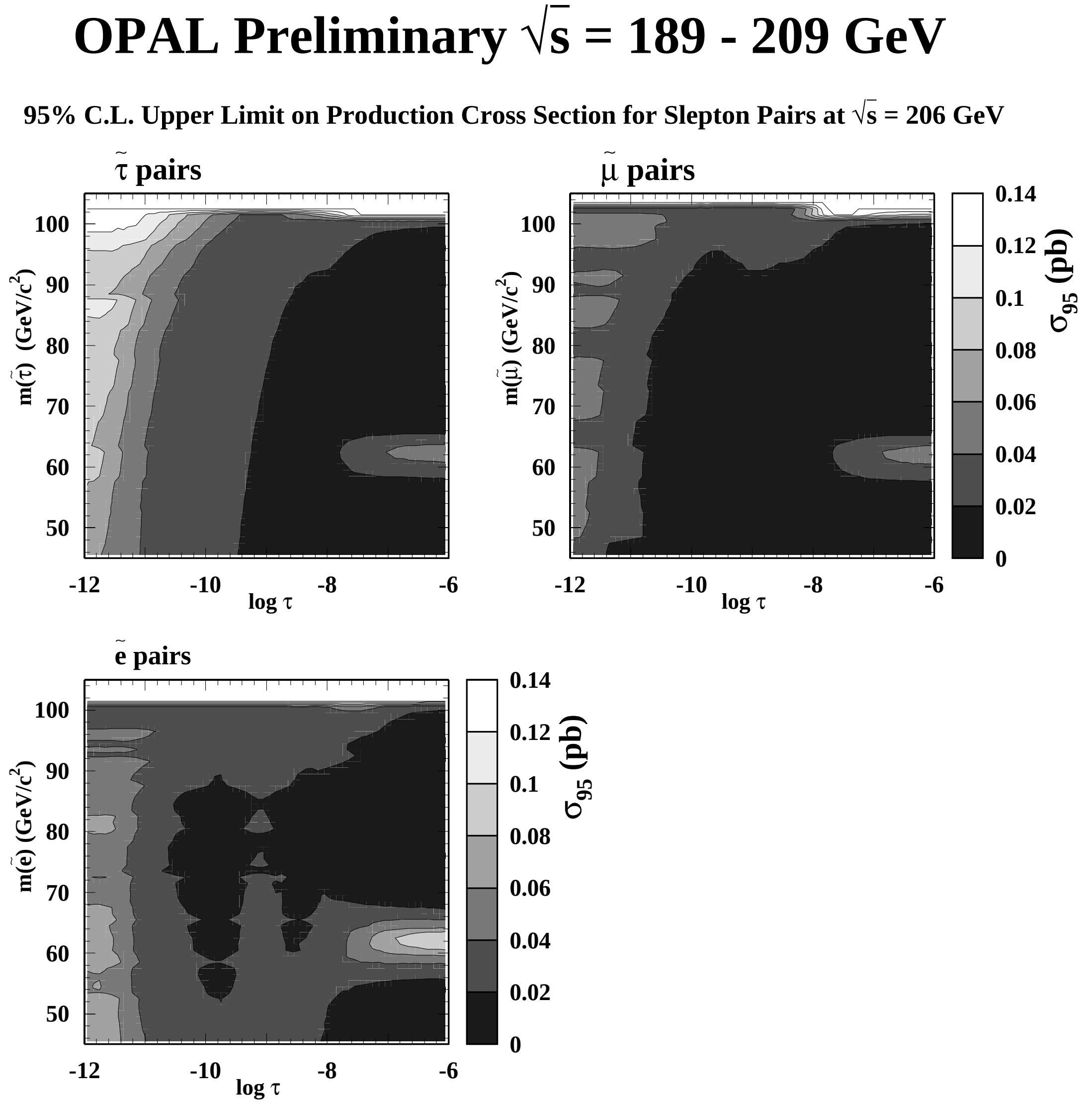

Figure C.2: Cross sections limits at 206 GeV for GMSB slepton production as a function of slepton mass and slepton lifetime, from combining the different lifetime analyses (from [43]).

Bibliography

[1] I. Aitchison and A. Hey, "Gauge theories in particle physics," (1989), Institute of Physics Publishing, Bristol.

[2] W. Beenakker *et al.*, "WW Cross-sections and Distributions," hep-ph/9602351.

[3] M. S. Turner, "Dark matter and dark energy in the universe," Phys. Scripta **T85** (2000) 210 [astro-ph/9901109].

[4] J. R. Ellis, "Beyond the standard model for hillwalkers," hep-ph/9812235.

S. P. Martin, "A supersymmetry primer," hep-ph/9709356.

M. Drees, "An introduction to supersymmetry," hep-ph/9611409.

[5] R. Haag, J. T. Lopuszanski and M. Sohnius, "All Possible Generators Of Supersymmetries Of The S Matrix," Nucl. Phys. B **88** (1975) 257.

[6] D. E. Groom *et al.* [Particle Data Group Collaboration], "Review of particle physics," Eur. Phys. J. C **15** (2000) 1.

[7] H. E. Haber and G. L. Kane, "The Search For Supersymmetry: Probing Physics Beyond The Standard Model," Phys. Rept. **117** (1985) 75.

[8] M. Carena *et al.*, "Higgs physics," arXiv:hep-ph/9602250. (Also published in "Physics at LEP2," edited by G. Altarelli, T. Sjöstrand and F. Zwirner,

CERN 96-01, Vol. 1 (1996) p. 351)

[9] S. Myers, "The LEP collider, from design to approval and commissioning, Nov 26, 1990," CERN-91-08 *Presented at CERN Accelerator School: The LEP Collider from Design to Approval and Commissioning, Geneva, Switzerland, Nov 26, 1990, CAS: CERN accelerator school, 6th John Adams Memorial lecture.*

[10] K. Ahmet *et al.* [OPAL Collaboration], "The OPAL detector at LEP," Nucl. Instrum. Meth. **A305** (1991) 275.

[11] S. Anderson *et al.*, "The extended OPAL silicon strip microvertex detector," Nucl. Instrum. Meth. **A403** (1998) 326.

[12] B. E. Anderson *et al.*, "The OPAL silicon - tungsten calorimeter front end electronics," IEEE Trans. Nucl. Sci. **41** (1994) 845.

[13] G. Aguillion *et al.*, "Thin scintillating tiles with high light yield for the OPAL endcaps," Nucl. Instrum. Meth. **A417** (1998) 266.

[14] M. Arignon *et al.*, "The trigger system of the OPAL experiment at LEP," Nucl. Instrum. Meth. **A313** (1992) 103.

[15] J. Allison *et al.*, "The detector simulation program for the OPAL experiment at LEP," Nucl. Instrum. Meth. **A317** (1992) 47.

[16] G. Abbiendi *et al.* [OPAL Collaboration], "W^+W^- production cross section and W branching fractions in e^+e^- collisions at 189 GeV," Phys. Lett. B **493** (2000) 249 [hep-ex/0009019].

[17] K. Ackerstaff *et al.* [OPAL Collaboration], "Search for anomalous production of di-lepton events with missing transverse momentum in e^+e^- collisions at $\sqrt{s} = 161$ GeV and 172 GeV," Eur. Phys. J. C **4** (1998) 47 [hep-ex/9710010].

[18] G. Abbiendi *et al.* [OPAL Collaboration], "Search for acoplanar lepton pair events in e^+e^- collisions at $\sqrt{s} = 161$ GeV, 172 GeV and 183 GeV," Eur. Phys. J. C **12** (2000) 551 [hep-ex/9808036].

[19] G. Abbiendi *et al.* [OPAL Collaboration], "Search for anomalous production of acoplanar di-lepton events in e^+e^- collisions at $\sqrt{s} = 183$ GeV and 189 GeV," Eur. Phys. J. **C14** (2000) 51 [hep-ex/9909052].

[20] S. Jadach, W. Placzek, M. Skrzypek, B. F. Ward and Z. Was, "Monte Carlo program KoralW 1.42 for all four-fermion final states in e^+e^- collisions," Comput. Phys. Commun. **119** (1999) 272 [hep-ph/9906277].

[21] A. Denner, *et. al.*, "Electroweak radiative corrections to $e^+e^- \rightarrow WW \rightarrow 4$ fermions in double-pole approximation – the RACOONWW approach", Nucl. Phys. B587 (2000) 67.

[22] J. A. Vermaseren, "Two Photon Processes At Very High-Energies," Nucl. Phys. B **229** (1983) 347.

[23] F. A. Berends, P. H. Daverveldt and R. Kleiss, "Monte Carlo Simulation Of Two Photon Processes," Comput. Phys. Commun. **40** (1986) 271-326.

[24] J. Fujimoto *et al.*, "grc4f v1.1: a Four-fermion Event Generator for e^+e^- Collisions," Comput. Phys. Commun. **100** (1997) 128 [hep-ph/9605312].

[25] S. Jadach, W. Placzek and B. F. Ward, "BHWIDE 1.00: $\mathcal{O}(\alpha)$ YFS exponentiated Monte Carlo for Bhabha scattering at wide angles for LEP1/SLC and LEP2," Phys. Lett. B **390** (1997) 298 [hep-ph/9608412].

[26] D. Karlen, "Radiative Bhabha Scattering For Singly Tagged And Untagged Configurations," Nucl. Phys. B **289** (1987) 23.

[27] S. Jadach, B. F. Ward and Z. Was, "Coherent exclusive exponentiation CEEX: The case of the resonant e^+e^- collision," Phys. Lett. B **449** (1999) 97 [hep-ph/9905453].

[28] S. Jadach, B. F. Ward and Z. Was, "The Monte Carlo program KORALZ, version 4.0, for the lepton or quark pair production at LEP / SLC energies," Comput. Phys. Commun. **79** (1994) 503.

[29] G. Montagna, O. Nicrosini and F. Piccinini, "NUNUGPV: A Monte Carlo event generator for $e^+e^- \to \nu\bar{\nu}\gamma(\gamma)$ events at LEP," Comput. Phys. Commun. **98** (1996) 206.

[30] F. A. Berends and R. Kleiss, "Distributions For Electron - Positron Annihilation Into Two And Three Photons," Nucl. Phys. B **186** (1981) 22.

[31] S. Katsanevas and S. Melachroinos, in "Physics at LEP2," edited by G. Altarelli, T. Sjöstrand and F. Zwirner, CERN 96-01, Vol. 2 (1996) p. 328; S. Katsanevas and P. Morawitz, "SUSYGEN-2.2: A Monte Carlo event generator for MSSM sparticle production at e^+e^- colliders," Comput. Phys. Commun. **112** (1998) 227 [hep-ph/9711417].

[32] C. Dionisi *et al.*, in "Physics at LEP2," edited by G. Altarelli, T. Sjöstrand and F. Zwirner, CERN 96-01, Vol. 2 (1996) p. 337.

[33] P. Janot, in "Physics at LEP2," edited by G. Altarelli, T. Sjöstrand and F. Zwirner, CERN 96-01, Vol. 2 (1996) p. 309.

[34] J. Allison, "Multiquadric radial basis functions for representing multidimensional high-energy physics data," Comput. Phys. Commun. **77** (1993) 377.

[35] D. I. Futyan, "Search for supersymmetry using acoplanar lepton pair events at OPAL," Ph.D. Thesis submitted to Univesity of Manchester, December 1999. (available from http://www.hep.man.ac.uk/hep/theses/DavidFutyan.ps)

[36] G. Abbiendi *et al.* [OPAL Collaboration], "Measurements of Standard Model Processes in e^+e^- Collisions at $\sqrt{s} = 203 - 209$ GeV," OPAL Physics Note PN469, Feb. 2001.

[37] G. Abbiendi *et al.* [OPAL Collaboration], "Tests of the Standard Model and Contraints on New Physics from Measurements of Fermion-pair Production at 192-202 GeV at LEP," OPAL Physics Note PN424, March 2000.

[38] G. Abbiendi *et al.* [OPAL Collaboration], "Tests of the standard model and constraints on new physics from measurements of fermion pair production at 189-GeV at LEP," Eur. Phys. J. C **13** (2000) 553 [hep-ex/9908008].

[39] B. C. Allanach *et al.*, "Report of the beyond the standard model working group of the 1999 UK phenomenology workshop on collider physics (Durham)," J. Phys. G **G26** (2000) 551 [hep-ph/9912302].

[40] G. Abbiendi *et al.* [OPAL Collaboration], "New Particle Searches in e^+e^- Collisions at $\sqrt{s} = 200 - 209$ GeV," OPAL Physics Note PN466, November 2000.

[41] G. Abbiendi *et al.* [OPAL Collaboration], "New Particle Searches in e^+e^- Collisions at $\sqrt{s} = 192 - 202$ GeV," OPAL Physics Note PN418, November 1999.

[42] G. Abbiendi *et al.* [OPAL Collaboration], "Search for Charged Higgs Bosons in e^+e^- Collisions at $\sqrt{s} = 189 - 202$ GeV," OPAL Physics Note PN432, July 2000.

[43] G. Abbiendi *et al.* [OPAL Collaboration], "Searches for Intermediate Lifetime Signatures in e^+e^- Collisions at $\sqrt{s} = 189 - 209$ GeV," OPAL Physics Note PN478, July 2001.

[44] Combined LEP SUSY results available from LEP SUSY working group web page at http://lepsusy.web.cern.ch/lepsusy/